The Autonomous Landing of an Unmanned Helicopter on a Moving Platform

by

Christopher Kurt Fourie

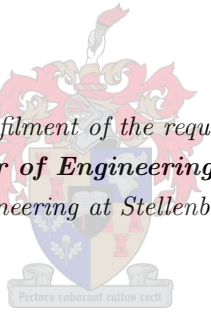

Thesis presented in partial fulfilment of the requirements for the degree
Master of Engineering
in the Faculty of Engineering at Stellenbosch University

Supervisor:
Prof. Thomas Jones
Department of Electrical and Electronic Engineering

December 2015

Declaration

By submitting this thesis/dissertation electronically, I declare that the entirety of the work contained therein is my own, original work, that I am the sole author thereof (save to the extent explicitly otherwise stated), that reproduction and publication thereof by Stellenbosch University will not infringe any third party rights and that I have not previously in its entirety or in part submitted it for obtaining any qualification.

December 2015

Abstract

This work details the design and implementation of an autonomous landing system for an unmanned helicopter. The system was broken down in to two separate systems - an autonomous navigation and control system design for an X-Cell .90 Aerobatic Helicopter, and a safe-landing system utilising ship motion prediction to discern ideal landing periods for autonomous helicopter landings.

The helicopter control system is based on a successively closed control system architecture optimized for the X-Cell .90 Aerobatic Helicopter. A state-machine is used to implement fully autonomous landing behaviour, with tracking and landing modes tested for full autonomous landings on a moving platform. Results are given for both hardware-in-the-loop simulated landings, as well as practical landings. Successful practical landings were demonstrated on a target moving at 11 kph.

A quiescent period detection system was developed based on data obtained from the South African Navy. This system makes use of a prediction technique to provide advance warning of quiescent periods as well as the ship's deviation from such periods. A classifier based on multiple predictors was implemented to provide an aggregate prediction on whether it is safe for a helicopter to land. Performance, while conservative, illustrated that such a system is feasible and suitable for further development.

Uittreksel

Hierdie werkstuk behandel die ontwerp en implementering van ’n outonome landingstelsel vir ’n onbemande helikopter. Die stelsel is verdeel in twee afsonderlike substelsels - ’n outonome navigasie- en beheerstelsel ontwerp vir ’n X-Cell .90 akrobatiese helikopter, en ’n veilige landingsisteem wat skipbeweging voorspel om ideale landingsperiodes te herken vir outonome helikopterlandings.

Die helikopter beheerstelsel is gebasseer op ’n opeenvolgende lus-sluiting argitektuur wat vir die X-Cell .90 akrobatiese helikopter geoptimeer is. ’n Toestandmasjien word gebruik vir die implementering van volle outonome landingsgedrag, met getoetsde volging en landingsmodusse vir volle outonome landings op ’n bewegende platform. Resultate word voorsien vir beide gesimuleerde hardeware-in-die-lus landings sowel as praktiese landings. Suksesvolle landings was gedemonstreer op ’n platform wat teen 11 kph beweeg het.

’n Statiese tydperk voorspellingsstelsel is ontwikkel om relatief statiese periodes in beweging op te spoor, gebasseer op data van die Suid-Afrikaanse Vloot. Die stelsel maak gebruik van ’n voorspellingstegniek om ’n vroegtydige waarskuwing van statiese periodes sowel as afwyking van die skip te gee. ’n Klassifiseerder wat gebasseer is op verskeie voorspellers is geïmplementeer om ’n gekombineerde voorspelling vir veilige landingstoestande te voorsien. Konserwatiewe prestasies illustreer dat só ’n stelsel haalbaar en vir verdere ontwikkeling geskik is.

Acknowledgements

Challenging as this work was, I don't feel that I've ever in my life had an opportunity to learn so much. It has certainly been a growing experience and, despite the numerous upsets and challenges, I've found the experience to be incredibly rewarding. With this in mind, I would like to thank the following people for their advice, experience and frequently invaluable support that allowed me to achieve my goals.

1. First and foremost, I owe significant thanks to my supervisor Professor Thomas Jones. He was kind enough to mentor and guide me throughout this process, and his support has been invaluable.
2. Many of the technical staff at Stellenbosch have been an invaluable aid in the completion of this work. Wessel Crouwcamp, for always going beyond the call of duty to help me fix the helicopter whenever it broke (his frequent support was greatly appreciated). Petro Petzer and his staff for helping me set up and bolt down the moving platform.
3. Japie Engelbrecht for taking great interest in this work as well as his attendance and support at almost every single flight test.
4. Cornelus le Roux for sharing an office with me and putting up with me, even when times were tough.
5. And lastly, to my family, as always, for their never ending support. To my father in particular, for his careful proof reading of this document and unfailing interest in this work.

Contents

List of Figures

List of Tables

Chapter 1

Introduction

The subject of autonomous helicopter navigation and control systems has been extensively studied worldwide, and is currently a popular area of research at many institutions. While generally involved in military applications, the scope for UAVs has been found to increasingly include civilian use [1]. Non-military research began in the early 1990's, and has subsequently grown into a major field of research.

The general agility and controllability of helicopters, as well as their hovering and VTOL capability, has made them ideal for a large range of applications [2], including potential in applications such as Remote Sensing, Disaster Response, Surveillance, Search and Rescue, Transportation, Communications and military applications [3]. In particular, their usage as experimental surrogates for larger, more expensive systems makes them invaluable for research purposes.

Autonomous flight for unmanned helicopter systems is often generalized into the broader "Vertical Take-Off and Landing - Unmanned Aerial Vehicle" research category (VTOL-UAV). This particular field of study has been of interest for several decades, largely due to the complexity of the helicopter model and the applicability of control systems to improve their ease of use.

At the Electronics Systems Lab, the subject of Autonomous Takeoff and Landing (ATOL) has been studied for several years. This project was commissioned as one of the final implementations of rotary VTOL systems on moving platforms.

1.1 Problem Statement

The landing of a helicopter on board a ship deck is a hazardous and dangerous procedure, requiring immense skill on the behalf of the pilot and landing supervisor. Margins for human error are large when landing, consequently resulting in stringent operational restrictions for helicopter operations at sea. Despite this, accidents persist - spawning numerous engineering approaches in an attempt to alleviate the shortcomings.

The landing of a UAV helicopter on a moving ship deck can be seen to be an equally difficult task in which predictable autonomous behaviour would greatly aid and improve the operational capabilities of UAV's at sea.

The ship-sea environment presents a complex and dynamic scenario that contains a series of generally mitigatable hazards, including dynamic roll over, ground effect, superstructure wake and general impact considerations that must be accounted for and considered in the design of an autonomous landing system.

This study aims to provide an operable, practical system both for flight control and autonomous landing, capable of mitigating the associated hazards where possible. The project is an extension of previous work done at the Electronic Systems Lab (ESL) relating to the autonomous flight of helicopters.

1.2 Project History

Much of the early research into rotary UAV systems at the Electronic Systems Lab (ESL) at Stellenbosch University was conducted by Nicol Carstens [4], who worked on the instrumentation and basic automation of an electrically powered remote control (RC) helicopter. Using a JR Voyager E Model Helicopter, Carstens was able to demonstrate successful yaw, height and longitudinal position control.

The helicopter used was found to be limited in its payload capabilities (and hence ability to carry avionic control and instrumentation systems), as well as suffering from mechanical problems. It was then subsequently replaced with an X-Cell Fury .60 Expert[1] in 2004. The X-Cell helicopter has been used in several studies world-wide and thus, due also to the availability of models and the positive results obtained by Gavrilets et al. [5], the acrobatic model helicopter made a suitable candidate for the project as well as for future work to be completed [6]. As part of his master's dissertation, Stephanus Groenewald was responsible for the design of an expandable avionics architecture, based on the CAN standard, that allowed for additional sensors and actuators to be added to the system with relative ease [6]. The avionics system was completed in 2005.

In 2008, Carlo van Schalkwyk [7] and Louis-Emile Rossouw [8] investigated different control algorithms to autonomously control the helicopter in flight. Carlo van Schalkwyk investigated full-state feedback approaches, whilst Rossouw designed a successive loop closure control system to control the helicopter. Both control structures were practically tested.

At the time of writing, much of the current research at the lab is in achieving VTOL capabilities on moving platforms or decks, the emphasis being for use in guidance systems to aid landing on seafaring vessels.

1.3 Similar Work

Recent interest in the applications of UAV's to both the military and civil aviation sectors has provided a wealth of information with regard to VTOL-UAV's and autonomous landing. A brief overview on the state of the art is provided here.

Static landings have been performed by a variety of international researchers, with results from [9, 10] illustrating precision performance using a camera setup. Performance on a full scale helicopter was demonstrated in [11]. Landing a helicopter on a moving platform is a substantially more complex problem and the applicable literature

[1] The X-Cell Fury .60 Expert comes fitted with a .70 methanol based glow engine, producing a theoretical maximum power of 1716W

deals with various techniques or approaches that could be used to alleviate the associated issues. One such proposed technique is optimal trajectory control [12], later implemented using a visual feedback technique [13] where the position of the target in the future is presumed to be precisely known. A similar approach using a path planning approach has been suggested [14], a simulated vision based system [15], as well as the use of a tether to aid landing [16]. Additionally, a visual servoing technique was found to work well for a quad rotor device in conjunction with a sliding mode controller [17].

Various models exist for UAV helicopters, with the work of Mettler [18] and Gavrilets [5] providing an early and commonly used simplified model for control systems development. Many additional models exist based on several first principle approaches [19, 20, 21].

Differing control techniques have generated a plethora of results. Specific control approaches have included both linear and non-linear techniques, with a variety of design requirements ranging from aggressive control to robust control in the presence of model uncertainty. Linear techniques have included a standard PID loop-shaping approach [9], an optimal control approach (LQR) [22], model predictive control (MPC) [23] as well as a study comparing the applicability of several pertinent linear techniques to ship board landings [24]. Non-linear techniques have included State-Dependent Riccati Equation implementations [25], a composite non-linear feedback technique [26], an optimal trajectory control scheme [12], dynamic inversion [27], backstepping [28] as well as a robust non-linear control scheme illustrated by Marconi [29]. A review of standard control techniques can be found in [30].

With regard to state estimation, camera systems have been considered a powerful source of rapid, accurate relative information and much of the literature deals with the extraction of useful information [31, 9, 32].

1.4 Approaches to Shipboard Landing

A standard shipboard landing approach is detailed by Padfield [33] as a manoeuvre in which the pilot lines up on alongside of the landing deck and awaits a quiescent period during which a landing can be attempted. Once such a quiescent period has been detected, the pilot moves over the deck and lands the helicopter. The procedure is illustrated in Figure 1.1.

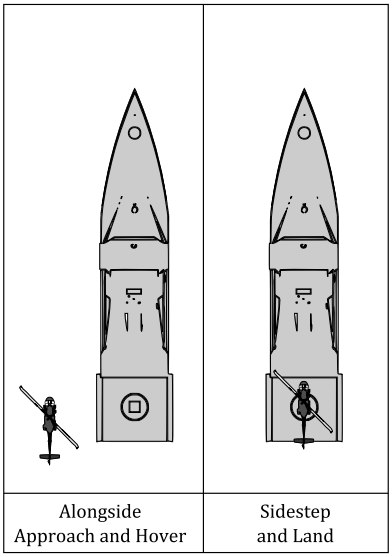

Figure 1.1: Standard Deck Landing Mission Task Element, adapted from [33]

Such an approach has many practical advantages for a human pilot and allows the pilot to directly observe the deck and assess its motion before hovering over it (where many visual cues are blocked from the pilot's view). Visual limitations do not apply to UAV's, resulting in many autonomous approaches deviating from de facto methods used by pilots, and instead commencing with a direct overhead hover before attempting a landing, or by trailing the ship and performing a track and land manoeuvre [13, 14, 16].

1.5 Critical Objectives

This work aims to provide a realisable system, conservative in approach but broad in applicability. The principal outcomes of this work include,

1. The development of a full-scale autonomous landing procedure or algorithm for an autonomous UAV helicopter to land on a moving, heaving, pitching, rolling platform,
2. The design of a system to adequately establish if a landing attempt will fall within operational limits, and
3. The practical testing of the system on a UAV in an experimental setup.

The focus will be in ensuring the safety and preservation of the UAV helicopter, defining optimality to be in terms of realistic operational characteristics and robustness as opposed to speed of response or best case results.

1.6 Project Breakdown

The project can be broken down into a series of sections that directly relate to the implementation of a landing system. At the beginning of the project the helicopter model was already implemented as well as a rudimentary control system. The control and estimation systems were found to perform sub-optimally and the re-implementation of these key components was brought into the scope of this work.

The philosophy used in this work mimics current operational characteristics and behaviours seen in full-scale, manned helicopter missions. As a result, the system will be required to land the helicopter during a quiescent period and a system will need to be derived to establish such periods autonomously.

The primary elements involved in this project are discussed in the table below, providing a loose specification for the establishment of a working system.

The system will be designed for optimal performance where possible but will favour conservatism in light of possible failure modes. The end results will ideally conform to a system that can repeatedly perform autonomous landings on a moving ship deck.

Project Element	Description
Helicopter Modelling	In order to accurately control the helicopter, a model will need to be derived from which a new control system can be designed.
Ship Modelling	The dynamic interface between the helicopter and ship, as well as a description of possible failures in landing need to be established.
Control System Design	A control system capable of providing precise tracking of a moving deck will need to be designed, while still maintaining good disturbance rejection qualities, particularly for wind.
Autonomous Behaviour Design	The autopilot tracking capabilities will need to be designed to include the desired landing capabilities as well as standard operational behaviour.
Quiescent Period Detection	A system will need to be derived that will select optimum points for the helicopter to perform a landing in a safe and predictable manner.
Hardware Implementation	Practical testing will require the hardware implementation of the designed systems, as well as thorough hardware-in-the-loop testing.
Practical Flight Testing	The practical realisation of the system will provide a valuable indication of the helicopter's ability to perform autonomous landing in the presence of possibly unmodelled factors.

Table 1.1: Project Breakdown

1.7 Scope and Limitations

The scope of this work will focus primarily in the control and autonomous systems design, with an additional focus on the question of quiescent period detection. Optimal sensor choice and ideal state estimation techniques are considered out of the scope of this work, and working systems from other projects will be used where appropriate.

Hardware designs and choices will be based on the avionics systems developed in-house at the Electronic Systems Laboratory at Stellenbosch University. Modifications will be made where appropriate or necessary, but general hardware approaches are considered out of the scope of this work.

Due to the nature of the testing of this project (where flight tests will be performed in simulated conditions), it is unnecessary and possibly dangerous to test the landing systems with states outside of the safe landing limits discussed in Section 2.2.2. To facilitate testing, landing will occur within the set limits at the command of the ground station operator. Quiescent period detection techniques will not be practically tested outside of a simulated environment (using real data provided by the South African Navy of a 70m+ ship with a helicopter landing area in South African waters).

1.8 Plan of Development

This dissertation will begin with a description of the modelling techniques used to describe both the helicopter and the ship deck, as well as the implied limitations for simulation. This will be followed by a detailed description of the helicopter control system design procedure with results generated from the linear model as well as the results obtained from the system when implemented with the previously specified gains. The feed forward response capabilities are discussed as well as the system's ability to reject disturbances from wind.

The focus of the work will then shift to the design of the autonomous systems where landing controllers and waypoint navigation are discussed. After discussing software simulations detailing the predicted performance of these systems, the implementation of the systems in hardware will be discussed and preliminary results from Hardware-in-the-Loop simulations will be presented. Flight test results demonstrating the applicability of the systems in practice will be shown directly after this.

Lastly, an implementation of a Quiescent Period Prediction system will be discussed based on results using datasets obtained from the South African Navy.

Chapter 2

System Modelling

The modelling requirements for this project involve modelling the helicopter, modelling the motion of the ship deck, as well as developing a model for the interaction between the helicopter and the ship deck. The purpose in modelling is to realistically encapsulate forces and effects that occur in the real world within a simulation, so as to ensure the correct functioning of the designed systems in practice. The more accurate the model, the more accurate controllers can be designed and implemented.

This chapter begins with details regarding the helicopter model, followed by the deck and relevant interactions, concluding with a discussion on the merits and limitations of the models.

2.1 Helicopter System Modelling

The non-linear helicopter model used in this work is a simplified model based predominantly on the work completed by Vladislav Gavrilets [34] that has been shown to be adequate for control system design purposes. Several pertinent assumptions are made that are discussed at the end of the section. Gavrilets based the model predominantly on his own linearisations and the work by Padfield [33] and Bramwell [35].

The helicopter used in this project is the X-Cell .90 Aerobatic Helicopter. The helicopter was originally used based on its reputable design, and is the same helicopter that was used by Gavrilets [22]. Other helicopters used with similar modelling approaches include the Vario Helicopter [36] and the Yamaha R-max [2].

This section will begin by defining the axes and coordinate systems used, the standard six degree-of-freedom model, followed by the model's components, aerodynamic effects and actuators.

The aerodynamic model discussed here was primarily implemented in Simulink by Medellin-Colombia [8], for which model parameters were estimated by Groenewald [6]. A detailed comparison of the model parameters can be found in Groenewald's dissertation. Several components were added to the model including a detailed deck model and a ground effect model. Empirical data was also used to improve the fidelity of the simulation model and several parameters were significantly modified to improve the matching between recorded and simulated data.

2.1.1 Coordinate Systems

To fully model the helicopter in simulation, the model makes use of two coordinate systems. The first is the body-fixed coordinate system, illustrated in Figure 2.1, while the second is the Earth Coordinate System.

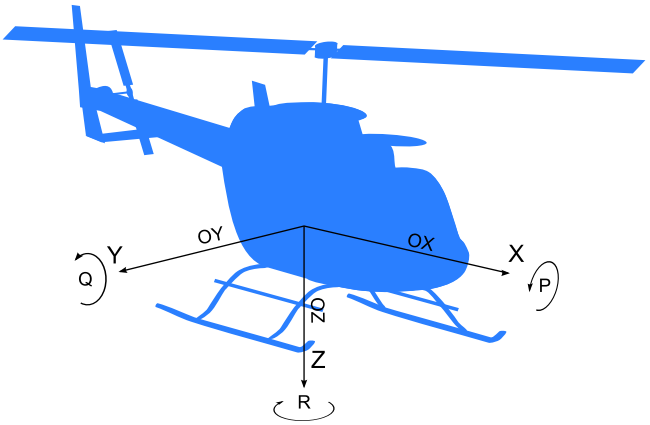

Figure 2.1: Helicopter Axes Definition

The body-fixed axis essentially defines the directions associated with body-fixed velocities and angular rates, and is defined following the notation described by Blakelock [37]. In essence, Blakelock defines the position O as the centre of mass, the direction OX as the direction stretching to the nose of the craft, and the direction OY as the direction pointing to the right of the aircraft. OZ is the direction down from the CG, perpendicular with the OXY plane.

The velocities u, v and w are the equivalent velocities associated with the axes along the OX, OY and OZ directions respectively[1]. The angular rates are defined around these axes in a similar fashion. Roll rate (p) is defined as a rotation around the OX axis, pitch rate (q) around the OY axis, and yaw rate (r) around the OZ axis.

It is necessary that the definitions obey the right-hand rule, and so the following vectors are defined. In this context, $\mathbf{V_b}$ is used to describe the body-fixed velocity, while $\omega_\mathbf{b}$ describes the body-fixed angular velocity.

$$\mathbf{V_b} = \begin{bmatrix} u \\ v \\ w \end{bmatrix} \qquad \omega_\mathbf{b} = \begin{bmatrix} p \\ q \\ r \end{bmatrix}$$

The earth axes are defined using the North-East-Down coordinate system, a coordinate system similar in principle to the intuitive North-East-Altitude convention, except using the downward direction in order to satisfy the right hand rule.

The Euler angles are defined based on the orientation of the body-fixed axis to the earth axis. Positive roll implies a rotation of the body-fixed axis around its OX direction, with the OY direction rotating towards the earth (for roll angles less that 90°).

Similarly, positive pitch implies a rotation of the axis around the OY direction, with the OX direction rotating

[1] This velocity is defined with respect to the body axis, but is relative to the earth axis. The conversion between the two resulting velocity measurements is defined in Section 2.1.2

towards the sky. Positive yaw angle is the clockwise angular deviation from the North direction. These definitions are illustrated in Figure 2.2.

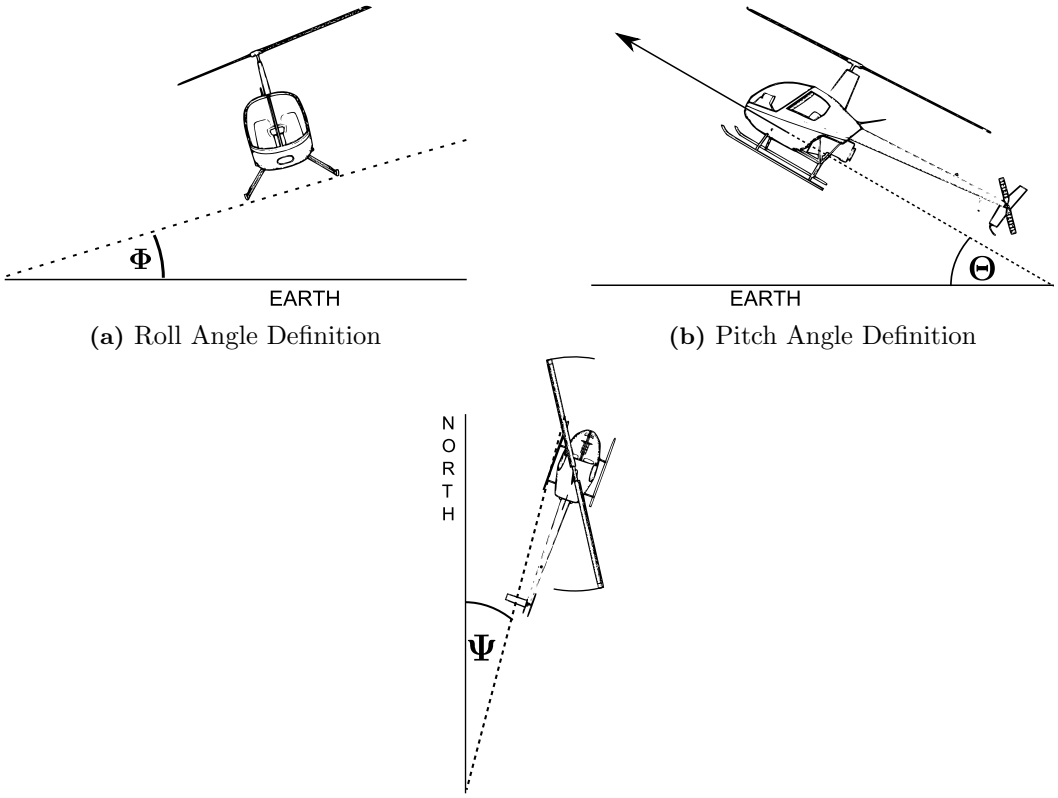

(a) Roll Angle Definition

(b) Pitch Angle Definition

(c) Yaw Angle Definition

Figure 2.2: Euler Angle Definitions

2.1.2 Equations of Motion

These equations of motion completely describe the motion of a six degree of freedom object, and the full derivation can be viewed in [37]. The resulting equations, commonly referred to as the Newton-Euler Equations of Motion, have the form shown in Equations 2.1 to 2.6.

$$\dot{u} = (vr - wq) + \sum_i X_i/m \tag{2.1}$$

$$\dot{v} = (wp - ur) + \sum_i Y_i/m \tag{2.2}$$

$$\dot{w} = (uq - vp) + \sum_i Z_i/m \tag{2.3}$$

$$\dot{p}I_{xx} = qr(I_{yy} - I_{zz}) + (\dot{r} - pq)\,J_{xz} + \sum_i L_i \tag{2.4}$$

$$\dot{q}I_{yy} = pr(I_{zz} - I_{xx}) + (r^2 - p^2)J_{xz} + \sum_i M_i \tag{2.5}$$

$$\dot{r}I_{zz} = pq(I_{xx} - I_{yy}) + (\dot{p} - qr)\,J_{xz} + \sum_i N_i \tag{2.6}$$

where, X_i, Y_i and Z_i are the individual force contributions, and L_i, M_i and N_i are the moment contributions. The force contributions are summarized at the end of this chapter. Note that these equations are for the full

inertia matrix, defined as follows,

$$J = \begin{bmatrix} I_{xx} & J_{xy} & J_{xz} \\ J_{yx} & I_{yy} & J_{yz} \\ J_{zx} & J_{zy} & I_{zz} \end{bmatrix}$$

In the equations above, symmetry around the centre of gravity is assumed, implying that $J_{xy} \equiv J_{yz} \equiv 0$. The additional term, J_{xz} is often neglected if its contribution is small.

The change in Euler angle is dependent on the current orientation of the body-fixed axis and the current fixed-body angular rates. The following equation can be derived [37] to provide the conversion between body-fixed angular rates and rate of change of the Euler angles.

$$\begin{bmatrix} \dot{\Phi} \\ \dot{\Theta} \\ \dot{\Psi} \end{bmatrix} = \begin{bmatrix} 1 & \sin\Phi\tan\Theta & \cos\Phi\tan\Theta \\ 0 & \cos\Phi & -\sin\Phi \\ 0 & \sin\Phi\sec\Theta & \cos\Phi\sec\Theta \end{bmatrix} \begin{bmatrix} p \\ q \\ r \end{bmatrix}$$

Note that the conversion becomes undefined for heading rate when the pitch angle orientates the aircraft as being perpendicular to the Earth's NE plane ($\Theta = \pm 90°$). This is commonly referred to as the Gimbal Lock problem and can be considered to be when the heading angle is arbitrary or undefined. In this work this is considered to be a highly unlikely attitude for the helicopter and so the problem is acknowledged but disregarded.

Lastly, conversion between body-fixed and earth velocities and displacements is required. This can be achieved by a succession of rotation matrices such that a earth coordinate velocity can be rotated into the body-fixed frame of reference. This can be shown to be,

$$\mathbf{V_b} = \mathbf{R_\Phi R_\Theta R_\Psi V_E}$$

where these matrices are defined as the orthogonal rotation matrices,

$$\mathbf{R_\Psi} = \begin{bmatrix} \cos\Psi & \sin\Psi & 0 \\ -\sin\Psi & \cos\Psi & 0 \\ 0 & 0 & 1 \end{bmatrix} \qquad \mathbf{R_\Theta} = \begin{bmatrix} \cos\Theta & 0 & -\sin\Theta \\ 0 & 1 & 0 \\ \sin\Theta & 0 & \cos\Theta \end{bmatrix} \qquad \mathbf{R_\Phi} = \begin{bmatrix} 1 & 0 & 0 \\ 0 & \cos\Phi & \sin\Phi \\ 0 & -\sin\Phi & \cos\Phi \end{bmatrix}$$

The matrix $\mathbf{R_\Phi R_\Theta R_\Psi}$ is commonly referred to as the Direction-Cosine-Matrix (DCM), and is a uniform, orthogonal matrix. The DCM matrix can be expressed as follows,

$$\begin{bmatrix} U \\ V \\ W \end{bmatrix} = \begin{bmatrix} \cos\Psi\cos\Theta & \sin\Psi\cos\Theta & -\sin\Theta \\ \cos\Psi\sin\Theta\sin\Phi - \sin\Psi\cos\Phi & \sin\Psi\sin\Theta\sin\Phi + \cos\Psi\cos\Phi & \cos\Theta\sin\Phi \\ \cos\Psi\sin\Theta\cos\Phi + \sin\Psi\sin\Phi & \sin\Psi\sin\Theta\cos\Phi - \cos\Psi\sin\Phi & \cos\Theta\cos\Phi \end{bmatrix} \begin{bmatrix} \dot{N} \\ \dot{E} \\ \dot{D} \end{bmatrix}$$

It should be noted that these equations are relevant to any symmetrical rigid body with six degrees of freedom.

2.1.3 Control Inputs

The helicopter has four primary control inputs, three of which directly actuate the swashplate, the last of which directly actuates the tail rotor. These control inputs are described in terms of their orthogonal actuation capabilities of the rotor blades (after swashplate mixing has taken place). The swashplate, illustrated in Figure

2.3, is essentially made up of two disks separated by ball bearings or some of form of frictionless spacer. The lower disk, directly connected to the command inputs, remains stationary while the upper disk, connected directly to the blades by rods, rotates at the same rates as the blades. These rods, extending from the upper swashplate, modify the pitch of the blades based on their elevation (an action referred to as "feathering"). This provides a variable pitch of the blades as they move around their azimuth. The control inputs are defined as follows:

1. **Collective:** The collective control is the change in the collective pitch of the helicopter's blades (effected by physically raising or lowering the helicopter's swashplate), resulting in a change in the collective thrust produced by the rotor.
2. **Lateral and Longitudinal Cyclic:** The cyclic input defines the cyclic pitch of the helicopter blades - i.e. this describes the change in the differential thrust generated by the blades, in accordance with the angular shift in the swashplate. This in turn results in a change in the attitude of the helicopter's Tip-Path-Plane (TPP), which allows for lateral and longitudinal accelerations.
3. **Tail Rotor Pitch:** This input defines the pitch of the tail-rotor blades which produces a thrust that allows the system to yaw around its centre of mass. This input is used to control the helicopter's heading and to counteract the yawing moment generated by the main rotor blades.

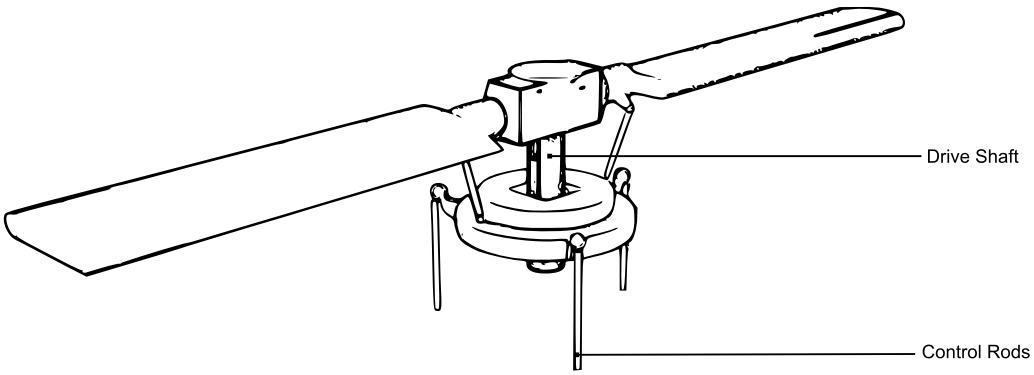

Figure 2.3: Helicopter Swashplate

2.1.4 Main Rotor Aerodynamics

The helicopter generates thrust based on the angular pitch of its spinning blades, deflecting the surrounding air mass and creating lift. There are two primary forms of thrust generation models, based either on Momentum Theory or on Blade Element Analysis.

For most helicopters, the blades are connected via a complicated hinge mechanism that allows in-plane flapping, out-of-plane flapping, and on-axis pitching (referred to as feathering, and providing the basis of the helicopter's actuation). The flapping is primarily implemented to reduce the bending stresses on the blades and the rotor head, slowing the dynamics of the helicopter. Steady state flapping angles are relative to the helicopter fixed body axes and can be seen as the reorientation of the Tip-Path-Plane relative to the helicopter's body.[2].

The blade azimuth angle ($\mathbf{\Psi_r}$) is measured from the rear of the helicopter, and indicates the instantaneous orientation of the blades relative to the fixed body axis (illustrated in Figure 2.4a). The helicopter disk, or

[2]The X-Cell Helicopter does not make use of out-of-plane flapping hinges, and relies instead on the flexibility of the blades to create the same effect.

Tip-Path-Plance, is subject to a series of forces that influence the thrust generated and orientation (i.e. flapping angle) relative to the helicopter. This is illustrated in Figure 2.4b

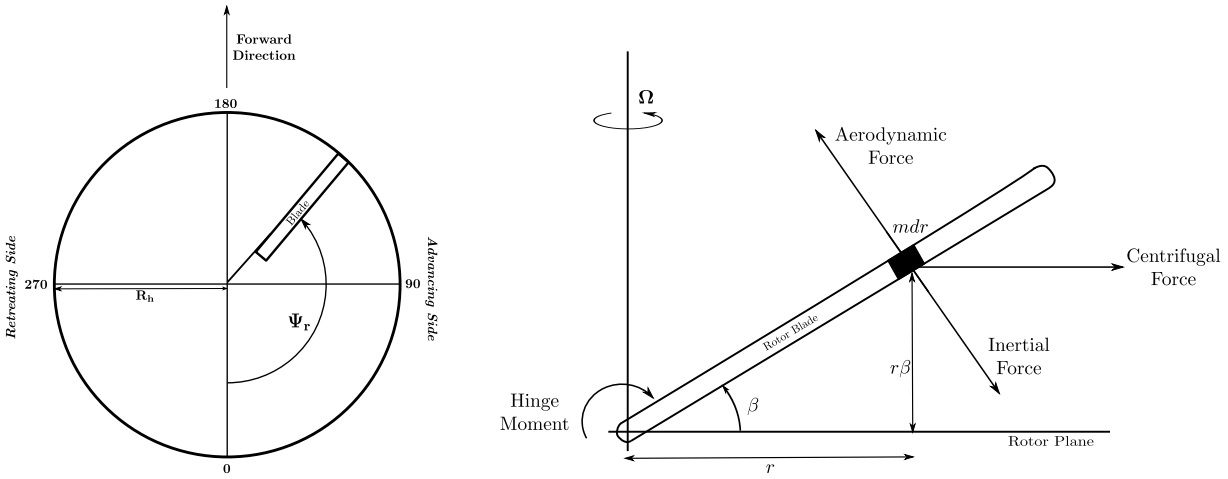

(a) Rotor Azimuth Illustration, adapted from [38]

(b) Illustration of Rotor Flapping Forces, adapted from [33]

Figure 2.4: Rotor Aerodynamic Forces and Azimuth Illustrations

These forces and moments can be broken down into inertial forces, centrifugal forces, aerodynamic forces, and the hinge moment associated with the rotor hub. The aerodynamic forces are the combination of lift and drag acting on an individual element, while the hinge moment is a restoring force seeking to pull the rotor blades back into the orthogonal plane.

The fundamental flapping equation is derived by Padfield [33], and can be shown to be,

$$\ddot{\beta} + \lambda_\beta^2 \beta = \frac{2}{\Omega}\left(p \cos \Psi_r + q \sin \Psi_r\right) \tag{2.7}$$

where λ_β is the flapping frequency. This equation neglects the aerodynamic forces, but illustrates a fundamental flapping dependency on pitch and roll rate that is shifted by 90°.

In steady state, the flapping angle can be shown to follow a harmonic form, allowing it to be represented as a sum of sinusoids,

$$\beta\left(t\right) = \sum_{n=0}^{\infty} \beta_{ns} \sin\left(n\Omega t\right) + \sum_{n=0}^{\infty} \beta_{nc} \cos\left(n\Omega t\right) \tag{2.8}$$

This can be simplified by only considering the first harmonic, allowing $\beta\left(t\right)$ to be represented as,

$$\beta\left(t\right) = \beta_0 + \beta_{1s} \sin(\Omega t) + \beta_{1c} \cos(\Omega t) \tag{2.9}$$

In modelling, the coning angle β_0 is ignored with regard to the Tip-Path-Plane, which is instead considered to be the plane formed relative to the body axes by the angles β_{1c} and β_{1s}. These angles, associated with the tip path plane and rotor flapping, are illustrated in Figure 2.5.

In the work by Gavrilets [34], it was found that (for the X-Cell) there was little cross-coupling in a commanded pitch and roll rate, and the flapping angles are represented by effective steady state longitudinal and lateral flapping angles, a_1 and b_1 respectively[3].

[3]It should be noted that swashplate mixing accounts for the phase shift in applied cyclic commands and apparent roll and pitch rate effects.

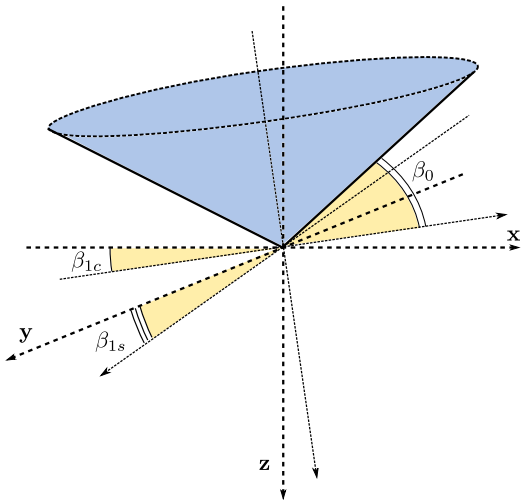

Figure 2.5: Rotor Flapping Illustration

With azimuth angular offsets implicitly accounted for, the first order rotor flapping dynamics are represented by Gavrilets [34] in the following equations,

$$\dot{b_1} = -p - \frac{b_1}{\tau_e} - \frac{1}{\tau_e}\left(\frac{\partial b_1}{\partial \mu_v}\mu_v + B_{\delta_{lat}}\delta_{lat}\right) \tag{2.10}$$

$$\dot{a_1} = -q - \frac{a_1}{\tau_e} - \frac{1}{\tau_e}\left(\frac{\partial a_1}{\partial \mu_u}\mu_u + \frac{\partial a_1}{\partial \mu_z}\mu_z + A_{\delta_{long}}\delta_{long}\right) \tag{2.11}$$

where μ is defined as the advance ratio (see Equation 2.14), while δ_{long} and δ_{lat} refer to the input cyclic controls. The value τ_e is the damping time constant and is defined by Padfield [33] to be,

$$\tau_e = \frac{16}{\gamma_{fb}\Omega} \tag{2.12}$$

Here, the value γ_{fb} is the Lock number[4] associated with the stabilizer bar, and is defined by,

$$\gamma_{fb} = \frac{\rho c a R^4}{I_\beta} \tag{2.13}$$

where ρ is the air density, c is the mean chord, a is the lift curver slope of the paddles, R is the radius of the bar, and I_β is the inertia of the stabilizer bar.

Gavrilets [34] found through experimentation that the values $A_{\delta_{long}}$ and $B_{\delta_{lat}}$ grew with variations in the rotor speed, and defined the effective gains as follows,

$$A_{\delta_{long}} = A^{nom}_{\delta_{long}}\left(\frac{\Omega}{\Omega_{nom}}\right)^2$$

$$B_{\delta_{lat}} = B^{nom}_{\delta_{lat}}\left(\frac{\Omega}{\Omega_{nom}}\right)^2$$

The advance ratio (μ) is defined as the planar velocity of the helicopter, and is used throughout the model to represent the speed of the helicopter relative to its rotor speed. The advance ratio has functional significance as advance ratios close to one imply a large dissymmetry of lift[5], establishing an upper bound on the forward

[4] The Lock number is the ratio of aerodynamic to inertial forces.

[5] A condition where the retreating blade generates far less lift than the advancing blade, due to the reduced relative velocity of the blade to the air as the helicopter increases its velocity relative to the ground.

speed of a particular helicopter. The general calculation of the advance ratio is shown in Equation 2.14.

$$\mu = \frac{\sqrt{(u-u_w)^2 + (v-v_w)^2}}{\Omega R} \tag{2.14}$$

A subscripted version of the advance ratio refers to the advance ratio in a particular direction, as illustrated in the following equations,

$$\mu_u = \frac{u-u_w}{\Omega R} \qquad \mu_v = \frac{v-v_w}{\Omega R} \qquad \mu_w = \frac{w-w_w}{\Omega R}$$

It should be noted that the flapping angle dynamics are directly dependent on the relevant angular rates, velocities and actuator inputs. The partial derivatives based on translational speed are a combination of the influence of the stabilizer bar[6] (modelled as a gain, K_μ), an increase in flapping based on the dissymmetry of lift (as well as flap back - shifted 90° due to the gyroscopic phase lag) and the inflow ratio, λ_0, (defined and discussed in Section 2.1.5). These were analytically derived by Gavrilets [34].

$$\frac{\partial a_1}{\partial \mu_u} = 2K_\mu \left(\frac{4\delta_{col}}{3} - \lambda_0 \right) \tag{2.15}$$

$$\frac{\partial b_1}{\partial \mu_v} = -\frac{\partial a_1}{\partial \mu_u} \tag{2.16}$$

The derivative with respect to downward velocity shows an increase in flapback due to the increase in lift generated from the downward motion [34]. This is represented in the derivative below, adapted from an estimate by Padfield [33],

$$\frac{\partial a_1}{\partial \mu_z} \approx K_\mu \frac{16\mu^2}{8\left|\mu_u\right| + a\sigma} \text{ sign } \mu_u \tag{2.17}$$

Here, σ is the solidity ratio of the blades, and is defined by

$$\sigma = \frac{2c}{\pi R} \tag{2.18}$$

The flapping dynamics described here are intended to describe dynamics for low advance ratios (below 0.15 - approximately 70 Kph (20 m/s) for the X-Cell), and may not be suitable for high speed applications. This work is intended for low speed (near-hover) application, and the advance ratio should remain well below 0.15.

2.1.5 Thrust Generation

The thrust generation model is based on that developed by Padfield [33] and Gavrilets [34]. The model is a simplified thrust generation model, neglecting flapping angles, cyclic inputs and angular rate influences [34]. In order for an idealized value for thrust to be calculated, an iterative approximation must be made to simultaneously solve two equations.

The coefficient of thrust, C_T, is defined [33] as,

$$C_T = \frac{T}{\rho\left(\Omega R\right)^2 \pi R^2} \tag{2.19}$$

There are two primary theories that are used to predict the thrust generated by the rotor blades - Momentum Theory, and thrust generated from Blade Element Analysis. In the model derived by Gavrilets [34], a simplified

[6] Stabilizer Bars increase the inertia of the main rotor blade, causing a stabilizing effect and increasing the damping ratio. On RC Helicopter systems, they also help the servos to actuate the main rotor blades.

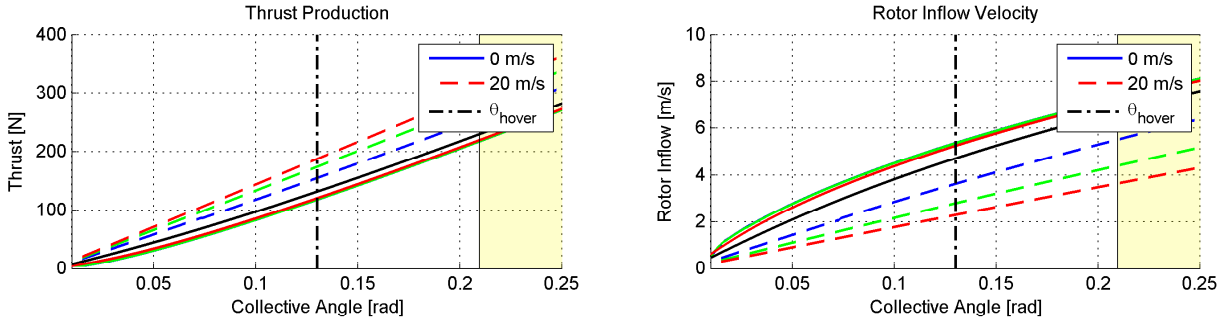

(a) Thrust Collective **(b)** Rotor Inflow Velocity

Figure 2.6: Influence of Forward Speed on Thrust Production

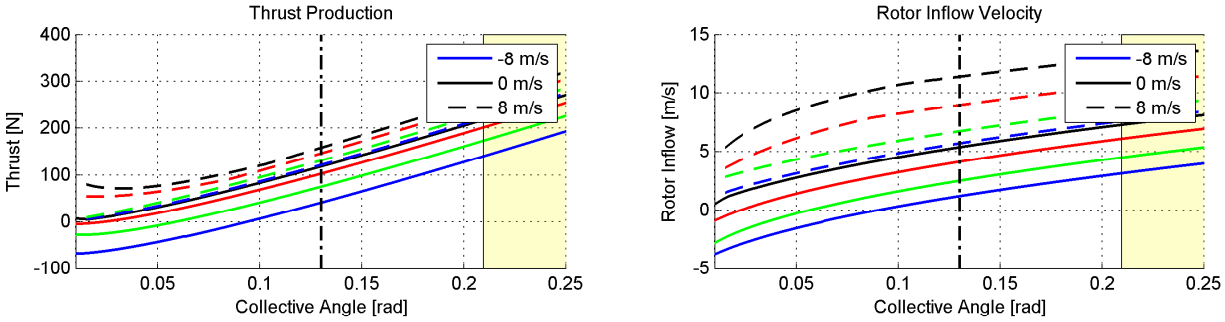

(a) Thrust Collective **(b)** Rotor Inflow Velocity

Figure 2.7: Influence of Downward Speed on Thrust Production

equation for thrust based on momentum theory is used,

$$C_T^{ideal} = \frac{a\sigma}{2}\left(\theta_0\left(\frac{1}{3}+\frac{\mu^2}{2}\right)+\frac{\mu_w-\lambda_0}{2}\right) \tag{2.20}$$

This equation directly disregards components from blade twist, angular rates and cyclic inputs, and does not account for dynamic inflow. In this equation, λ_0 is the inflow ratio, defined as the ratio of main rotor inflow velocity to the blade tip velocity.

$$\lambda_0 = \frac{V_{imr}}{\Omega R_{mr}} \tag{2.21}$$

The inflow ratio is approximated based on momentum theory as,

$$\lambda_0 = \frac{C_T}{2\eta_w\sqrt{\mu^2+(\lambda_0-\mu_w)^2}} \tag{2.22}$$

where η_w is a wake contraction factor found by Gavrilets [39] to be roughly 0.9. These equations are noticeably interdependent and cannot be analytically solved [33]. An iterative scheme, originally set up by Padfield [33], and modified by Gavrilets [39] allows the thrust to be calculated based on a Newton's method iterative solution. For the sake of completeness, the scheme is outlined below,

1. **Zero Function Definition (g_0)** : this is the function for which a solution is required (i.e a value for λ_0 should be found such that g_0 is zero). This zero function is defined to be,

$$g_0 = \lambda_0 - \frac{C_T}{2\eta_w\sqrt{\mu^2+(\lambda_0-\mu_w)^2}} \tag{2.23}$$

   where the thrust coefficient is the ideal coefficient defined in Equation 2.20.

2. **Solution based on Newton's Method** : The derivative of the zero function is found and used to iteratively approximating the solution,

$$\lambda_{0_{j+1}} = \lambda_{0_j} - f_j \frac{g_0}{(\partial g_0/\partial \lambda_0)_{\lambda_0=\lambda_{0_j}}} \tag{2.24}$$

Padfield [33] recommended a convergence factor of 0.6 and Gavrilets [34] found an explicit solution for the convergence iteration value to be,

$$\frac{g_0}{(\partial g_0/\partial \lambda_0)_{\lambda_0=\lambda_{0_j}}} = \frac{\left(2\eta_w \lambda_{0_j} \Delta^{1/2} - C_T\right)\Delta}{2\eta_w \Delta^{3/2} + \frac{a\sigma}{4}\Delta - C_T\left(\mu_z - \lambda_0\right)} \tag{2.25}$$

where the symbol Δ is a shorthand symbol referring to the relative speed,

$$\Delta = \sqrt{\mu^2 + \left(\lambda_0 - \mu_w\right)^2}$$

The scheme was found to perform extremely well, converging within 8 iterations to a g_0 error of approximately 0.001 for hover and forward flight. In testing, an initial estimate of λ_0 was defined based on the momentum theory definition of rotor inflow at hover, defined by Gavrilets [34] as,

$$V_{imr} = \sqrt{\frac{mg}{2\rho\pi R^2}} \tag{2.26}$$

The procedure was found to produce cogent variations in thrust for forward and downward velocities, shown for a variety of velocities in Figures 2.6 and 2.7. Forward flight showed fairly linear gradients for higher velocities ($\geq$ 10 m/s), with lower velocities following a slightly parabolic trajectory. Increases in forward flight speed show a large decrease in the rotor inflow velocity. In the figures shown, the shaded yellow area is the region in which stall would typically begin to occur (12° - 15° blade pitch angle), while a vertical line is used to indicate where typical collective settings (obtained from flight data) are for hover ($\mu \equiv \mu_z \equiv 0$).

Downward flight (positive or negative changes in altitude), illustrates acceptable performance for low velocities, but high velocities at low collective values show proximity to a singularity that may cause errors in simulation (where $\mu_w \equiv \lambda_0$ for small μ)[7]. Interestingly, this is reflected in the performance of actual helicopters, where the helicopter's thrust production is seen to stall in steep descent. This is caused by the helicopter's interaction with its own wake (known as a vortex ring state) which creates a hazardous situation that the pilot has difficulty correcting [38].

2.1.6 Ground Effect

Ground effect was added based on the observations and calculations of Padfield [33], who found that thrust increased by up to 15% when within a rotor radius of the ground. The equation used to simulate ground effect was,

$$G_{GE}(d,u,v) = \frac{1}{\left[1 - \frac{1}{16}\left(\frac{R}{d}\right)^2 / \left(1 + \left(\frac{\sqrt{u^2+v^2}}{v_i}\right)\right)\right]} \tag{2.27}$$

In this equation R is the rotor radius, d is the distance to the ground and v_i is the rotor inflow velocity. Essentially, the ground effect model provides a gain on thrust between 1 and 1.15 (capped value) that is modified based on its distance to the ground. The additional term seeks to model the decrease in ground effect

[7] It is worthwhile to note that momentum theory - upon which this model is based - technically applies to ascending flight, and descending flight extrapolations may not be fully indicative of actual performance.

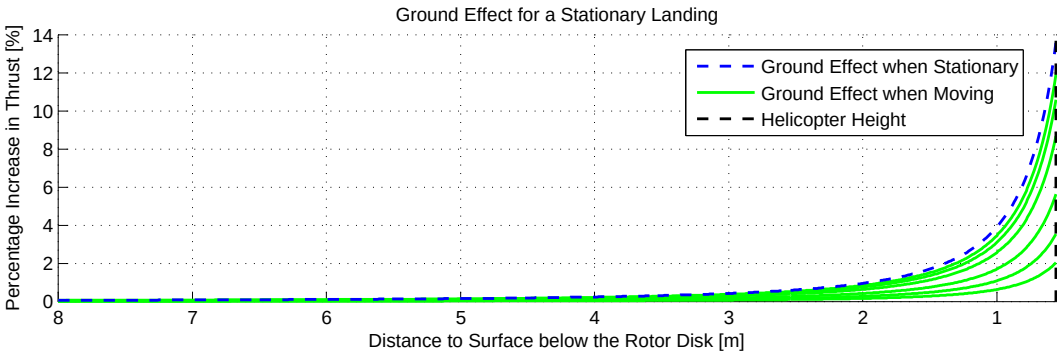

Figure 2.8: Influence of Ground Effect on Thrust Production

when moving at speed, where ground effect becomes negligible when the forward speed is more than twice the main rotor inflow velocity[8] [33].

The effect of this is illustrated in Figure 2.8, in which, based on the helicopter's parameters, the ground effect is simulated. The worst case increase in thrust caused by the helicopter's proximity to the ground is between 8 and 12% (a stationary landing), with rapidly decreasing effects depending on the forward speed of the helicopter (illustrated for simulated values of 0.5 m/s to 20 m/s). The rotor inflow velocity was based on that used for simulated hover, found to be approximately 4m/s. The helicopter height shown refers to the height of the main rotor blades above the ground.

2.1.7 Main Rotor Fuselage Coupling

To represent fuselage coupling, the simplified model detailed by Gavrilets [34] is used. This model, considered to be more than adequate for most cases [33], is implemented via a simple spring moment at the rotor (K_β, producing moment M_k) that acts as a restoring force for the out-of plane flapping. Thrust is modelled as a force perpendicular to the Tip-Path-Plane[9], reorientated by the flapping angle β (the generalisation of the longitudinal and lateral flapping angles, a_1 and b_1).

This simplified model, illustrated in Figure 2.9 and adapted from the work by Gavrilets [34], leads to Equations 2.28 to 2.33. These equations, detailed below, summarise the forces and moments caused directly by the main rotor (which are used in the Equations of Motions (defined in Section 2.1.2) to determine the helicopter's dynamic response for a series of inputs).

$$L_{mr} = (K_\beta + Th_{mr})\, b_1 \tag{2.28}$$
$$M_{mr} = (K_\beta + Th_{mr})\, a_1 \tag{2.29}$$
$$N_{mr} = Q_{mr} \tag{2.30}$$
$$X_{mr} = -Ta_1 \tag{2.31}$$
$$Y_{mr} = Tb_1 \tag{2.32}$$
$$Z_{mr} = -T_{mr} \tag{2.33}$$

Generally small flapping angles allow linear approximations to be used ($\sin a_1 \approx a_1$ for small values of a_1). Here, T refers to the thrust generated by the blades, whilst Q_{mr} refers to the reaction torque, defined by Gavrilets and Padfield as the sum of the induced torque and profile drag on the blades. It is generally notated as a

[8] For the helicopter used in this project, this would be speeds of above 8m/s (given that v_i is approximately 4m/s).
[9] Considered to be an acceptable assumption provided the advance ratio is well below 0.15

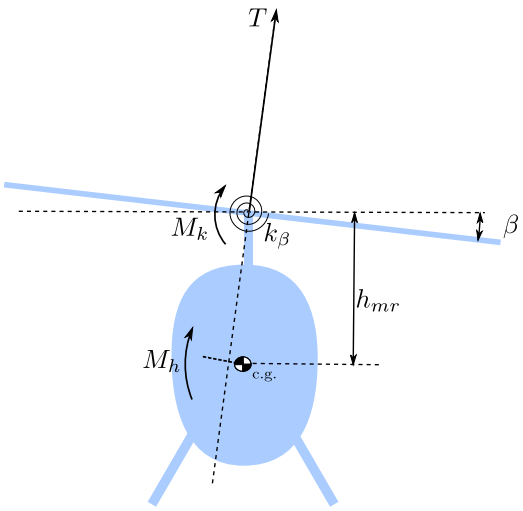

Figure 2.9: Illustration of Fuselage Forces and Moments, adapted from [34]

normalized coefficient, as shown in Equation 2.34.

$$C_Q = \frac{Q_{mr}}{\rho\left(\Omega R\right)^2 \pi R^3} = C_T\left(\lambda_0 - \mu_z\right) + \frac{C_{D_0}\sigma}{8}\left(1 + \frac{7}{3}\mu^2\right) \tag{2.34}$$

2.1.8 Tail Rotor

Tail rotor dynamics were modelled using the same method as used by Gavrilets in his initial work [39], where the same iterative equation used to approximate the main rotor thrust is used to approximate the tail rotor thrust.

In the model used, the tail rotor is modelled using an iterative thrust-inflow calculation, identical in concept (barring values used) to that used for the main rotor. The fin blockage factor suggested by Padfield [33] and introduced by Gavrilets as,

$$f_t = 1.0 - \frac{3}{4}\frac{S_{vf}}{\pi R_{tr}^2} \tag{2.35}$$

is incorporated into the model to model non-linear effects caused by its wake. Additional main rotor wake interaction effects were incorporated, as done by Gavrilets [34], by including a wake interaction factor K_λ that moderates the relative tail rotor velocities.

$$w_{tr} = w_a + l_{tr}q - K_\lambda V_{imr} \tag{2.36}$$

For the tail rotor, the advance ratio is then calculated as,

$$\mu_{tr} = \frac{\sqrt{u_a^2 + w_{tr}^2}}{\Omega_{tr} R_{tr}} \tag{2.37}$$

Gavrilets [34] defined the wake interaction factor K_λ as,

$$K_\lambda = 1.5 \cdot \frac{\frac{u_a}{V_{imr} - w_a} - g_i}{g_f - g_i} \tag{2.38}$$

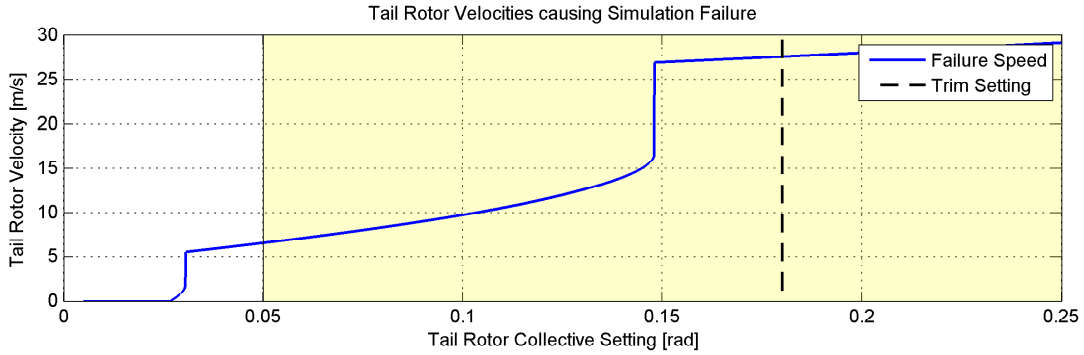

Figure 2.10: Tail Rotor Velocities causing Simulation Failure

where g_f and g_i are trigonometric approximations defined as,

$$g_i = \frac{l_{tr} - R_{mr} - R_{tr}}{h_{tr}} \tag{2.39}$$

$$g_f = \frac{l_{tr} - R_{mr} + R_{tr}}{h_{tr}} \tag{2.40}$$

The wake interaction factor, K_λ, is capped between 0 and 1.5, allowing a maximum interaction as well as incorporating the case when no interaction is taking place (e.g. at hover).

Thrust is calculated in the same manner as for the main rotor, with the side force, Y_{tr}, approximated as,

$$Y_{tr} = C_T^{tr} \rho \left(\Omega_{tr} R_{tr}\right)^2 \pi R_{tr}^2 \tag{2.41}$$

The yawing and rolling moments are then calculated as,

$$N_{tr} = -Y_{tr} l_{tr} \tag{2.42}$$

$$L_{tr} = Y_{tr} h_{tr} \tag{2.43}$$

In the later work by Gavrilets [34], the calculated thrust was replaced with two analytical derivatives to counteract failure modes that were encountered during simulation[10], Gavrilets [34] citing by way of example the case where the tail rotor gets caught in its own wake. To ensure that similar issues were not encountered, the velocities causing approach to singularity at specific collective settings were found through a gradient descent approach. Essentially, this method searched for the velocity that would cause $\lambda_0 \equiv \mu_z$ at $\mu \equiv 0$ (the singularity point). The velocities are shown for the range of collective values in Figure 2.10.

Theoretically analogous to the vortex ring state, tail rotor thrust simulation failure can occur for a large variety of lateral velocities and yaw rates. For low tail rotor collective settings, this can occur at reasonable lateral velocity values and yaw rates, causing potential simulation failure. Higher collective settings would require very large angular (yaw) or lateral velocities to cause simulation failure - considered a potentially unlikely scenario, as the trim point exists in this region and helicopter dynamics are limited to be well below the potential failure velocity.

It is important to note that collective settings close to zero imply negligible downwash, further implying that velocities close to zero would cause the iterative procedure to fail (see Equation 2.22). Low collective settings thus increase the chance of simulation error, and care should be taken to ensure that proximity to this region is avoided or that analytical derivatives are used instead of the iterative thrust algorithm.

[10]Dr. Gavrilet's work involved the autonomous aerobatic flight of an unmanned helicopter, which would involve several complex flow problems that would cause the iterative algorithm to fail.

In the case of this work, the trim setting for the tail rotor collective setting is relatively high (0.18 rad or 10.31°). The helicopter's simulated dynamics were limited to yaw rates of 3.141 rad/s and the tail rotor collective deflection to 8° (or 0.1396 rad) - implying a worst case tail rotor collective setting of 2.35° (≈ 0.05 rad). The resulting region of operation is illustrated in the yellow region in Figure 2.10. At such collective settings, failure is unlikely as a lateral velocity of higher than 7 m/s (or a yaw rate of higher than 8 rad/s) is required to cause simulation errors. Due to this, the use of the iterative procedure was considered acceptable for the work.

2.1.9 Drag and Empennage Contributions

The drag force contributions are based on the force experienced by a flat plate exposed to a dynamic pressure. For the fuselage, the drag forces are approximated by Gavrilets [34] as,

$$V_\infty = \sqrt{u_a^2 + v_a^2 + (w_a + V_{imr})^2} \tag{2.44}$$

$$X_{fus} = -0.5\rho S_x^{fus} u_a V_\infty \tag{2.45}$$

$$Y_{fus} = -0.5\rho S_y^{fus} v_a V_\infty \tag{2.46}$$

$$Z_{fus} = -0.5\rho S_z^{fus} (w_a + V_{imr}) V_\infty \tag{2.47}$$

where S_i^{fus} refers to the relevant approximate drag areas. The forces are assumed to be centred around the C.G. and therefore produce negligible moments.

The empennage forces are stabilizing forces, approximated by Gavrilets [34] using first order lift approximations. Two stabilizing elements provide direct contributions - the vertical fin, and the horizontal stabilizer. Their force and moment contributions are defined below,

$$Y_{vf} = -0.5\rho S_{vf} \left(C_{L\alpha}^{vf} V_\infty^{tr} + |v_{vf}| \right) v_{vf} \tag{2.48}$$

$$N_{vf} = -Y_{vf} l_{tr} \tag{2.49}$$

$$L_{vf} = Y_{vf} h_{tr} \tag{2.50}$$

$$Z_{ht} = 0.5\rho S_{ht} \left(C_{L\alpha}^{ht} |u_a| w_{ht} + |w_{ht}| w_{ht} \right) \tag{2.51}$$

$$M_{ht} = Z_{ht} l_{ht} \tag{2.52}$$

The lift coefficients were approximated by Groenewald [6]. The force contributions from both the horizontal stabilizer and vertical fin are capped at a maximum value to account for aerodynamic stall. The relative velocities are defined by Gavrilets [34] using the following equations,

$$v_{vf} = v_a - \epsilon_{vf}^{tr} V_{itr} - l_{tr} r \tag{2.53}$$

$$w_{ht} = w_a + l_{ht} q - K_\lambda V_{imr} \tag{2.54}$$

$$V_\infty^{tr} = \sqrt{u_a^2 + w_{tr}^2} \tag{2.55}$$

2.1.10 Summary of Helicopter Forces and Moments

The forces and moments acting on the helicopter are combined together in simulation to provide a test bed for the designed systems. A summary of the forces acting on the helicopter are described in Equations 2.56 to 2.61.

$$\sum X_i = X_{mr} + X_{fus} + X_g \tag{2.56}$$
$$\sum Y_i = Y_{mr} + Y_{tr} + Y_{fus} + Y_{vf} + Y_g \tag{2.57}$$
$$\sum Z_i = Z_{mr} + Z_{fus} + Z_{ht} + Z_g \tag{2.58}$$
$$\sum L_i = L_{mr} + L_{tr} + L_{vf} \tag{2.59}$$
$$\sum M_i = M_{mr} + M_{ht} \tag{2.60}$$
$$\sum N_i = N_{mr} + N_{tr} + N_{vf} \tag{2.61}$$

These forces are passed into a six degree-of-freedom force simulation block (governed by the equations described in Section 2.1.2) and the relevant physical responses are generated. In the equations above, the only contribution not previously mentioned is that of gravity, which can be computed simply as,

$$\begin{bmatrix} X_g \\ Y_g \\ Z_g \end{bmatrix} = DCM_h \begin{bmatrix} 0 \\ 0 \\ g \end{bmatrix} \tag{2.62}$$

This summary specifies the core of the non-linear helicopter model, and is used for the full non-linear simulation of the X-Cell .90 Helicopter in near hover conditions.

2.2 Deck Interaction

The interaction between the helicopter and the deck is an important aspect of the landing problem, where the required model is used both to design the landing system as well as to predict the physical responses from the landing. Ground effect was included in the model, and was implemented based on the work by Padfield [33] (see Section 2.1.6 for a detailed description).

2.2.1 Ship-Deck Modelling

For simulation, the ship was modelled as a point mass subjected to various transients and disturbances in order to provide stimuli for its interactions with the helicopter. The deck itself was then modelled as a point linearly offset from the ship's centre of gravity (c.g.), as illustrated in Figure 2.11. The deck's angular and linear velocities can be described based on those occurring at the centre of gravity of the ship - illustrated in Equations 2.63 and 2.64. The orientation of the deck remains the same as that of the ship.

$$\omega_{deck} = \omega_{ship} \tag{2.63}$$
$$\mathbf{V}_{deck} = \mathbf{V}_{ship} + \omega_{ship} \times \mathbf{r}_{ship} \tag{2.64}$$

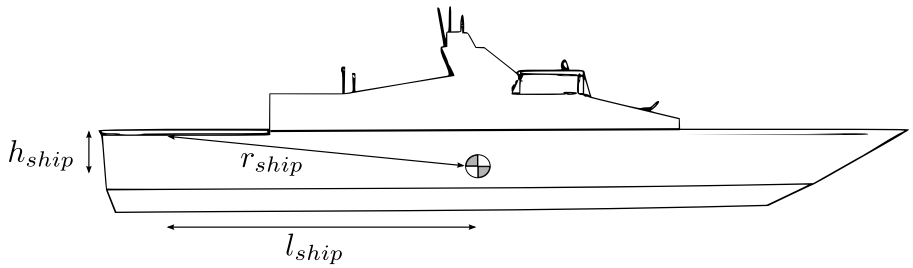

Figure 2.11: Ship Deck Physical Offset

where the vector $\mathbf{r}_{ship}$ is the deck's position relative to the ship's centre of gravity and is defined as,

$$\mathbf{r}_{ship} = \{l_{ship}, w_{ship}, h_{ship}\} \tag{2.65}$$

In testing, landing was accomplished either with actual ship motion data obtained from the South Africa Navy, or using data simulated to conform to the limitations described in the following section.

2.2.2 Deck Limitations for Landing

Operational limits for landing on a helicopter deck are defined in terms of angular limits, rates and absolute heave motion of the c.g. In this work, limit estimates provided by the South African Navy were used, as well as operational limits used in commercial missions. These limitations, consisting of angular rates, attitude, velocity and position dynamics, are detailed in Table 2.1. In order to conform to a safe landing, the requirements are stringent - very low velocities and attitude / position deviations are required in order for the dynamics to conform to a safe landing opportunity. These stringent requirements are primarily due to the large accelerations experienced by the helicopter when deviating from its angular trim values (potentially causing dynamic rollover and other unwanted effects). The large dimensions of the ship are also significant, as an offset of around 40m - typical for a Corvette class ship - can equate to over 1.3m additional heave deviation for a pitch angle of 2°.

The limit standards considered in this work are detailed in Table 2.1. Operational limits from the Helicopter Certification Agency (HCA) [40], NATO STANAG 4154 [41] and those obtained from the South African Navy are shown for comparison. In this case, the heave values cited for the HCA are those for the wave heave motion, not that of the ship[11]. Should the ship's physical length be greater than the wavelength of the sea waves, the actual heave motion of the ship itself may be lower.

The values quoted from the HCA are for a medium sized helicopter landing on a large ship (Class A Helicopter landing on a Class 2 Helideck). Considering the values obtained from the South African Navy, it can be seen that the heave rate values given imply a shorter (more aggressive) heave period when at maximum amplitude

[11]It should be noted that the HCA has begun to consider the Heave Motion Criteria to be deprecated. [40]

Standard	Roll/Pitch Angles (deg)	Roll/Pitch Rates (deg/s)	Heave Rates (m/s)	Heave Motion (m)
Helicopter Certification Agency	±3	-	1.0	3.0
South African Navy	P: ±2, R: ±3	±2	2	1.2
NATO STANAG 4154	R: 2.5°, P: 1.5° (RMS)	-	1	-

Table 2.1: Ship Operational Limits for Landing

(at around 4 seconds as opposed to 19 seconds for the HCA standards). The limitations suggested by the South African Navy are deferred to in this work.

2.2.3 Deck Reaction Modelling

To emulate the expected forces at impact, a simplified force model adapted from Swart [42] (based on the work by Blackwell [43]) was used, in which a single-stage spring damper reaction force was used to model the force experienced by one of the helicopter legs. The reaction force was defined as follows,

$$F_s(d) = \begin{cases} 0 & \text{if } d \geq 0 \\ K_s d + B_d \dot{d} & \text{if } d < 0 \end{cases} \tag{2.66}$$

In Equation 2.66, the value d is the deflection of the helicopter leg into the deck while K_s and B_d are spring and damper coefficients that define the dynamic response of the reaction. To approximate the deflection of the helicopter's leg into the deck, the position of the helicopter's legs were found relative to the deck's inertial frame of reference using Equation 2.67.

$$D_{ijk} = DCM_d \times (X_h - X_d) \tag{2.67}$$

Similarly, the velocity of the helicopter's leg, translated to the deck's inertial frame of reference, can be expressed as shown in Equation 2.68.

$$\dot{D}_{ijk} = DCM_d \cdot \left(\dot{X}_h - \dot{X}_d\right) \tag{2.68}$$

In these equations, X_h is a matrix representing the inertial position of the helicopter's legs in the NED coordinate system (i.e. the rotated and offset values from the Helicopter's fixed body axis, modelled as points in space). Similarly, X_d is the inertial position of the deck's centre of gravity in NED coordinates. The DCM matrix is used to translate the relative offset vector into the Deck's coordinate system. Due to the offsets from the CG, the velocity components incorporate the angular rates and relevant moment arms through the following equation,

$$\dot{X}_b = DCM_b^T \cdot (v_b + \omega_b \times r_b)$$

From this context, the k component can be used to calculate the vertical reaction force which can then be translated back to the helicopter through Equation 2.69.

$$F_h = \sum_i DCM_h \cdot DCM_d^T \cdot F_s \tag{2.69}$$

The landing gear moments were obtained by crossing the forces with the relevant moment arms (or individual skid location relative to the helicopter body, X_{s_i})

$$M_h = \sum_i F_{h_i} \times X_{s_i} \tag{2.70}$$

The spring-damper constants, K_s and B_d were found by equating the bounce reaction in simulation to a perceived reaction in real life. Values of $K_s = 1200N/m$ and $B_d = 53.9Ns/m$ were found to perform adequately for the task.

Planar forces were implemented through a dynamically calculated reaction force that cancels the current i,j,k body force and yaw moment of the helicopter using a Moore-Penrose Pseudo inverse. The nature of the inverse ensures the solution closest to the origin is chosen (as the solution is underconstrained) and ensures that the effective lateral and longitudinal forces are cancelled from the helicopter in such a way as to ensure that the

yaw moment on the helicopter is also cancelled.

Each leg was modelled as exhibiting a single in plane force, expressed in orthogonal i, j components. These forces are responsible for a net force and yaw moment that can be expressed in matrix form as shown in Equation 2.71. The reaction force at each leg can be found if the matrix is at full rank and invertible[12], and the desired output forces are known.

$$\begin{bmatrix} F_i \\ F_j \\ M_k \end{bmatrix} = \begin{bmatrix} 1 & 0 & 1 & 0 & 1 & 0 & 1 & 0 \\ 0 & 1 & 0 & 1 & 0 & 1 & 0 & 1 \\ S_{1j} & S_{1i} & S_{2j} & S_{2i} & S_{3j} & S_{3i} & S_{4j} & S_{4i} \end{bmatrix} \begin{bmatrix} F_{1i} \\ F_{1j} \\ \vdots \\ F_{4i} \\ F_{4j} \end{bmatrix} \tag{2.71}$$

Pseudo-inverting this matrix presents a minimalist solution for the component forces acting at the individual helicopter legs. These forces were then capped based on theoretical friction limitations to ensure that if a single force exceeds the theoretical limit ($\mu\vec{N}$) then the limit is given as the solution.

In order to bring the helicopter to a standstill, the current in-plane forces acting on the helicopter alongside parasitic friction functions are specified for the forces and moments acting on the helicopter. These forces are summarised in Equation 2.72, where v_i and v_j refer to the helicopter's velocity component in the i and j directions, and ω_k refers to the helicopter's rotational velocity around the k axis.

$$\begin{bmatrix} F_i \\ F_j \\ M_k \end{bmatrix} = - \begin{bmatrix} F_i \\ F_j \\ M_k \end{bmatrix}_H - \alpha \begin{bmatrix} B_{v_i} v_i \\ B_{v_j} v_j \\ B_{\omega_k} \omega_k \end{bmatrix} \tag{2.72}$$

This solution was found to perform well, arresting the helicopter when making contact with the deck, and providing believable sliding reactions when the deck was at an angle. Simulation problems did occur, primarily impacting Hardware-in-the-Loop simulation, where the simulation was found to significantly slow down to better approximate the reaction to the produced forces. During hardware-in-the-loop simulations this functionality was disabled to ensure that real-time updates were maintained, limiting the theoretical fidelity of the calculated response during hardware tests.

2.3 Modelling Limitations and Benefits

In modelling the helicopter and its interactions with the ship deck, there are approximations and assumptions made that may impact both the fidelity of the simulation as well as the designed control laws. While the majority of these assumptions are made with this specific project in mind, these same assumptions can have lasting effects that limit the times during which the simulation holds fidelity.

Of particular note are the implications of the assumptions and approximations to the helicopter's sphere of operation (within the context of this work), as well as the implications of the helicopter's interaction with the ship deck.

[12]This matrix will be invertible for all cases but for when only one leg is in contact with the deck - at which point it is no longer necessary.

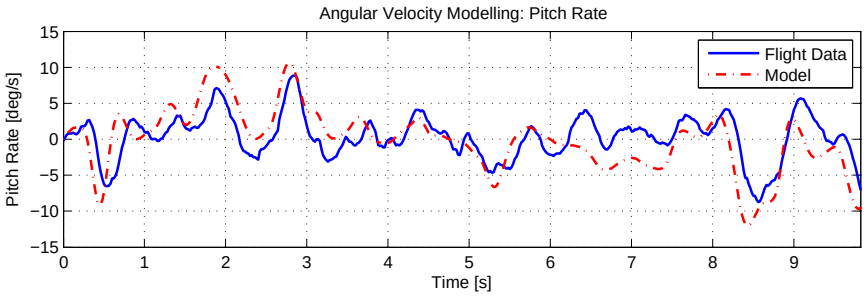

Figure 2.12: Model Calibration Results for Pitch Rate

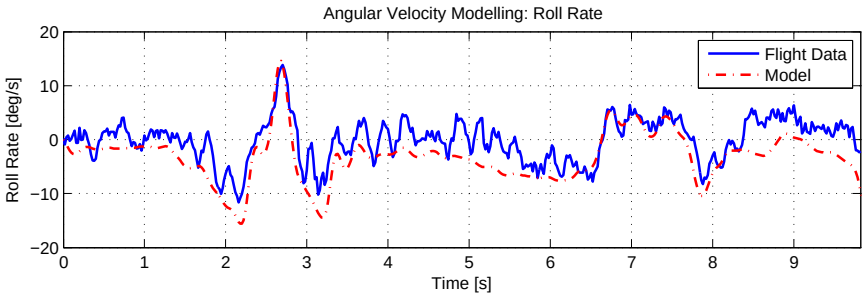

Figure 2.13: Model Calibration Results for Roll Rate

2.3.1 Helicopter Modelling

A helicopter has an incredibly complex interaction of forces, the effects of many of which are not modelled here. The linear flapping approach and the use of first order flapping angles in thrust production and lateral / longitudinal actuation ability may differ from the effects seen in the real world, particularly in the presence of wind or other disturbances. Additionally, the calculation of thrust does not account for dissymmetry of lift, implying that the model used will deviate from reality for large velocities and accelerations. Vortex ring states are modelled, although the extrapolations may be not be appropriate for descending flight.

The helicopter model also assumes that the centre of gravity coincides with its physical centre, and the main rotor blades sit directly above this centre. While the implications of this assumption are not necessarily dire, it is important to note as a large imbalance would significantly affect the coupling of forces.

In this work the designed system will operate predominantly around hover modes, with typical operational velocities of around 5 m/s - equivalent to an advance ration of 0.03, well below the theoretical modelling accuracy limit of 0.15 [34]. The tail rotor failure mode, discussed in Section 2.1.8 is unlikely to occur given the operational limits of the helicopter.

As part of a system verification process, the model was recalibrated to ensure that it matched the responses seen in the field. Typical flight data[13] is shown for the roll and pitch rate responses in Figures 2.12 and 2.13. Theoretical responses for the same actuator inputs are shown overlayed on the figures, illustrating congruous behaviour of both model and flight.

While, these responses do not match perfectly (influenced by a variety of factors, such as wind, variations in air pressure or sensor noise), the system is seen to perform similarly around trim in the model as it does in practice. Actuator commands are seen to give similar responses and dynamic responses are congruous with those predicted by the model.

[13] This data was collected during piloted flight, on a fairly wind still day.

2.3.2 Deck Interaction Modelling

In deck landing operations, particularly once landed, there are several effects that are of particular importance that must be modelled. These include the effects of slipping and sliding on the deck, bouncing associated with a hard impact, as well as the more complicated interactions associated with ground effect and dynamic rollover. The large velocity gains associated with a slight angular deviation from helicopter trim imply fairly stringent limits on the actual motion and orientation of the deck.

In the modelling approach used, the orientation of the deck does not feed back into the thrust generation model when close to the deck - which may imply that the thrust produced by the model when on the deck may not be indicative of the true response should large angular deviations occur.

Ground effect, without an active means to sense its influence, plays a significant and unpredictable role in deck landing, modified by cross winds and the motion of the deck. While this unpredictable force must be accounted for in design, it also presents a very difficult effect to accurately model. The empirical approximation suggested by Padfield is used in design, but the approximation may not be appropriate for different landing areas, decks or small rotor craft.

The effect of the ship's superstructure on landing capabilities was considered out of the scope of this work, but the effect is still considered in landing approaches so that simulations will be indicative of effects experienced in practice. While superstructure wake effects have been neglected in modelling, the SHOL limits described by Padfield [33] give an indication on where deck landings are typically safe. In testing the outcome of this work, it is assumed that the wind gusts are relatively small and that the effect of wake interaction can be neglected.

The deck model should provide believable interactions for the helicopter in simulation provided that velocities are fairly low. Profile drag is not excluded from the aerodynamic model once landed[14] and so frictional forces must account for this as an additional load.

[14] Profile drag tends to be a very small force at the velocities used in this work - typically hitting 3N at a forward speed of 8m/s.

Chapter 3

Control System Design

The helicopter control system was redesigned to improve controller performance at hover as well as to allow functional tracking of moving targets. In the analysis, the updated gains sets are shown for the controllers, as well as detailed description on how they were designed.

The redesign focuses on finding gains appropriate for rapid tracking in forward flight as well as ensuring that functional performance is maximized. The linear model was estimated by using MATLAB's *linmod* functionality before fitting the model to a modified version of the model specified by Mettler *et al.* [18]. The controller was then designed by successively closing the required loops in a manner that maximises the performance of the controller. The control structure is intended for use in near-hover (low velocity) scenarios, and bank-to-turn style control (suitable for very fast manoeuvres) is neglected in this design.

3.1 Control Structure

The control structure is shown in Figure 3.1. Based on the design by Rossouw [8], this control structure was augmented with reference feed-forward states for position (to ensure asymptotic tracking of constant velocity moving targets) and additional feed-forwards to reduce disturbance to the system when in different modes of operation. These included feed-forwards from collective to the rudder command (to decrease the effect of the cross-coupling contribution from collective changes on yaw rate), as well as a feed-forward to reduce altitude loss in aggressive forward flight (where the collective signal is modified by the attitude of the helicopter).

The control structure is successively closed, and poses several advantages in terms of implementability, including a propensity towards robustness or aggressiveness, depending on the design choices of the designer. The structure is heuristically defined and is logically tunable, ensuring an intuitive design scheme open to optimisation through various techniques. The controllers' implementation includes integrators at key points (trim and actuator inputs), and is implemented as a tiered architecture with four layers of PID based controllers.

The heave and heading plants are first order, stable plants (in terms of their relevant pole placements) and a PI (proportional-integral) loop can be used to stabilize and control their relevant rates (see sections 3.3.2 and 3.5.1). A simple proportional controller is then adequate to command particular altitude or heading setpoints.

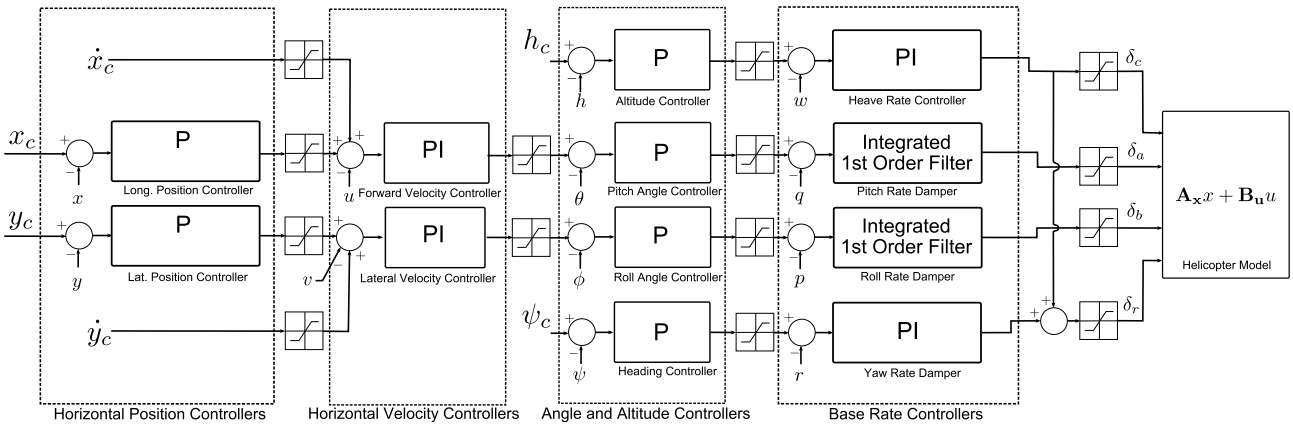

Figure 3.1: Helicopter Control System Structure

The lateral and longitudinal plants are slightly more complex, requiring a more sophisticated control strategy to ensure stability. The actuation of cyclic command inputs allows for immediate roll and pitch rate responses, and the resulting new orientation of the Tip-Path-Plane causes lateral and longitudinal accelerations. The control structure uses this to control position and velocity commands by precisely controlling the attitude of the craft. The poles associated with the flapping states were found to vary dramatically in their positions with slight perturbations in model trim and the control structure design was intended to ensure stability in the presence of particular model uncertainty.

In the work by Gavrilets, a reduced order model was used to design an LQR (Linear Quadratic Regulator) controller, with notch filters on collective implemented to reduce potential gain margin problems [34]. There are many alternative system designs that have been suggested, including the use of LQI (Linear Quadratic Integral Control) and MPC (Model Predictive Control) [24], a successively closed structure similar to the one suggested here [9], as well as a CNF (Composite Non-Linear Feedback) [26] control approach, among many others. In a comparison of many of these techniques, [24] found that loop-shaping design remained the most suitable design methodology for the autonomous landing of an unmanned helicopter on a moving ship deck.

3.2 Linear Model

The full 13-state linear model, defined by Mettler [18], was reduced into a 10-state model and is shown in Equation 3.1. Two of the removed states correspond to flapping states associated with the stabilizer bar, the effect of which has been incorporated into the main rotor flapping dynamics in the linear model. The additional state is an augmented yaw rate state included by Mettler [2] to account for the artificial yaw rate feedback system used on their helicopter. The yaw rate feedback was considered unnecessary for this model owing to the bypass of the on-board gyroscope in the control system, as well as the direct measurement of the actuator inputs to the system.

The linear model was split into two separate systems to ease the design, largely motivated by the work done in [34]. The lack of cross-coupling in the suggested states supported this design step, and the full linear model was split into two separate linear models, dubbed the longitudinal and the lateral model. The longitudinal model contained the states associated with the longitudinal and heave dynamics ($x_{long} = \{u, a_1, w, q, \theta\}$) while the lateral model contained the states associated with the lateral and yaw dynamics ($x_{lat} = \{v, b_1, p, r, \phi\}$).

The resulting two systems are generally described by the following equations, where A_x refers to the state-space

$$\begin{bmatrix} \dot{u} \\ \dot{v} \\ \dot{p} \\ \dot{q} \\ \dot{\phi} \\ \dot{\theta} \\ \dot{a_1} \\ \dot{b_1} \\ \dot{w} \\ \dot{r} \end{bmatrix} = \begin{bmatrix} X_u & 0 & 0 & 0 & 0 & -g & X_a & 0 & 0 & 0 \\ 0 & Y_v & 0 & 0 & g & 0 & 0 & Y_b & 0 & 0 \\ L_u & L_v & 0 & 0 & 0 & 0 & 0 & L_b & L_w & 0 \\ M_u & M_v & 0 & 0 & 0 & 0 & M_a & 0 & M_w & 0 \\ 0 & 0 & 1 & 0 & 0 & 0 & 0 & 0 & 0 & 0 \\ 0 & 0 & 0 & 1 & 0 & 0 & 0 & 0 & 0 & 0 \\ 0 & 0 & 0 & -1 & 0 & 0 & -1/\tau_e & A_b/\tau_e & 0 & 0 \\ 0 & 0 & -1 & 0 & 0 & 0 & B_a/\tau_e & -1/\tau_e & 0 & 0 \\ 0 & 0 & 0 & 0 & 0 & 0 & Z_a & Z_b & Z_w & Z_r \\ 0 & N_v & N_p & 0 & 0 & 0 & 0 & 0 & N_w & N_r \end{bmatrix} \begin{bmatrix} u \\ v \\ p \\ q \\ \phi \\ \theta \\ a_1 \\ b_1 \\ w \\ r \end{bmatrix} + \begin{bmatrix} 0 & 0 & 0 & 0 \\ 0 & Y_{tail} & 0 & 0 \\ 0 & 0 & 0 & 0 \\ M_{col} & 0 & 0 & 0 \\ 0 & 0 & 0 & 0 \\ 0 & 0 & 0 & 0 \\ 0 & 0 & A_{\delta_{lat}}/\tau_e & A_{\delta_{long}}/\tau_e \\ 0 & 0 & B_{\delta_{lat}}/\tau_e & B_{\delta_{long}}/\tau_e \\ Z_{col} & 0 & 0 & 0 \\ N_{col} & N_{tail} & 0 & 0 \end{bmatrix} \begin{bmatrix} \delta_{col} \\ \delta_{tail} \\ \delta_{lat} \\ \delta_{long} \end{bmatrix} \tag{3.1}$$

matrix mapping the interconnecting internal system dynamics, and B_x refers to the state-space matrix mapping the actuator inputs to the internal dynamics.

$$\dot{x}_{lat} = A_{lat}x_{lat} + B_{lat}u \tag{3.2}$$

$$\dot{x}_{long} = A_{long}x_{long} + B_{long}u \tag{3.3}$$

Using the helicopter's full non-linear model, estimates were obtained for these matrices around trim using the *linmod* functionality in MATLAB. These estimates were then used to manually fit the model to the non-linear responses to ensure congruity. The resulting linear models showed remarkable symmetry in the distribution of the poles and provided a useful system from which the controller could be designed.

The distribution of the longitudinal and lateral poles shows remarkable symmetry, and is shown in Tables 3.1 and 3.2. The corresponding state-space systems are shown in Equations 3.4 and 3.5. In both systems, a fast underdamped second-order system mode can be seen that corresponds directly to the coupled flapping angle-angular rate dynamics. Each system contains a double velocity pole close to the origin, indicative of the helicopter's inability to correct its orientation when disturbed (similar to the inverted pendulum effect). Lastly, each system has a single linear pole, relating to the heave rate in the case of the longitudinal system, and the yaw rate in the case of the lateral system.

The lateral system contains a fairly complicated interaction in which the roll rate directly disturbs the yaw rate, motivating the need for high bandwidth yaw rate control to mitigate the effect of lateral manoeuvres on the helicopter's heading. Additionally, when considering the B_{lat} matrix, a contribution from the collective setting to the yaw rate dynamics is evident, indicative of the increase in the rotor hub torque (and so the yaw rate) when a change in collective setting is made. This was found to be a fairly poor indication of the collective setting's ability to disturb the yaw rate system, and a direct linearization is performed to deduce the required gain for the system in Section 3.3.1.

In the work by Gavrilets [44], the fast flapping poles were removed and a steady state approximation to the relevant angular rate was used. This necessitated the use of notch filters to remove potential gain margin

$$\begin{bmatrix} \dot{v}(t) \\ \dot{b_1}(t) \\ \dot{p}(t) \\ \dot{r}(t) \\ \dot{\phi}(t) \end{bmatrix} = \begin{pmatrix} -0.141 & 34.88 & 0 & 0 & 9.81 \\ 0 & -21.99 & -0.8667 & 0 & 0 \\ -0.004542 & 565.6 & 0 & 0 & 0 \\ 0.05166 & 0 & 0.1843 & -0.858 & 0 \\ 0 & 0 & 1.0 & 0 & 0 \end{pmatrix} \begin{bmatrix} v(t) \\ b_1(t) \\ p(t) \\ r(t) \\ \phi(t) \end{bmatrix} + \begin{pmatrix} 0 & -52.06 & 0 & 0 \\ 0 & 0 & 5.498 & 0 \\ 0 & 0 & 0 & 0 \\ 0.001575 & 137.4 & 0 & 0 \\ 0 & 0 & 0 & 0 \end{pmatrix} \begin{bmatrix} \delta_c(t) \\ \delta_r(t) \\ \delta_a(t) \\ \delta_b(t) \end{bmatrix} \tag{3.4}$$

Pole Value	States	Inputs	Natural Freq.
-1.0629	w	δ_{col}	1.0629
$-12.64 \pm 11.32\ i$	q, a_1	δ_{long}	16.968
-0.0555	u	δ_{long}, a_1	0.0555
0.0011	u	δ_{long}, a_1	N/A

Table 3.1: Longitudinal Poles

Pole Value	States	Inputs	Natural Freq.
-0.85799	r	δ_{tail}	0.85799
$-10.99 \pm 19.22\ i$	p, b_1	δ_{lat}	22.14
-0.016028	v	δ_{lat}, b_1	0.016028
-0.12472	v	δ_{lat}, b_1	0.12472

Table 3.2: Lateral Poles

problems. The flapping poles were found to represent a fairly indeterminate mode that shifted with slight perturbations in the linear model fit, and as such the poles were monitored in the design to ensure that their associated root loci were stable and damped, regardless of their absolute position.

It should be noted that actuator time constants are significantly faster than the dynamics discussed here (barring the flapping dynamics) and were disregarded in the greater control design. For each controller, the effect of the other controllers is included as the design expands, ensuring that the controllers do not inadvertently disrupt each other. In this design, no further simplifications have been made.

$$\begin{bmatrix} \dot{u}(t) \\ \dot{a_1}(t) \\ \dot{w}(t) \\ \dot{q}(t) \\ \dot{\theta}(t) \end{bmatrix} = \begin{pmatrix} -0.05432 & -52.32 & 0 & 0 & -9.81 \\ 0 & -25.29 & 0 & -0.7 & 0 \\ 0 & 0 & -1.063 & 0 & 0 \\ -0.00007186 & 411.3 & 0.0004441 & 0 & 0 \\ 0 & 0 & 0 & 1.0 & 0 \end{pmatrix} \begin{bmatrix} u(t) \\ a_1(t) \\ w(t) \\ q(t) \\ \theta(t) \end{bmatrix} + \begin{pmatrix} 0 & 0 & 0 & 0 \\ 0 & 0 & 0 & 4.398 \\ -142.0 & 0 & 0 & 0 \\ 0 & 0 & 0 & 0 \\ 0 & 0 & 0 & 0 \end{pmatrix} \begin{bmatrix} \delta_c(t) \\ \delta_r(t) \\ \delta_a(t) \\ \delta_b(t) \end{bmatrix} \tag{3.5}$$

3.3 Heading Control Systems

The design of the heading control system is particularly influential on the overall dynamic response and performance of the helicopter. This is largely due to the wide range of disturbances that the heading plant is sensitive to, ranging from the interactions caused by the main rotor and the lateral dynamics, to general atmospheric disturbances such as variations in wind speed and air pressure.

In order to combat these disturbances to the helicopter's yaw rate system, high bandwidth control is desired to minimize the effect of their interactions. In addition to this, to reduce the effect of a change in collective setting on the yaw rate plant, a feed-forward link from the collective setpoint directly to the rudder setpoint is implemented. The presence of fast, high frequency measurements from the gyroscopes and magenetometer, as well as a particularly high-bandwidth servomotor driving the tail rotor link, allows for this control scheme to be implemented as a fast, aggressive control system.

3.3.1 Collective Feed-forward

The collective feed-forward is an open-loop link designed to mitigate the disturbance experienced when a change in the collective setting is made, thus reducing the requirement for the yaw rate controller to directly combat the disturbance. The gain between collective and yaw rate was not adequately predicted by the linmod function,

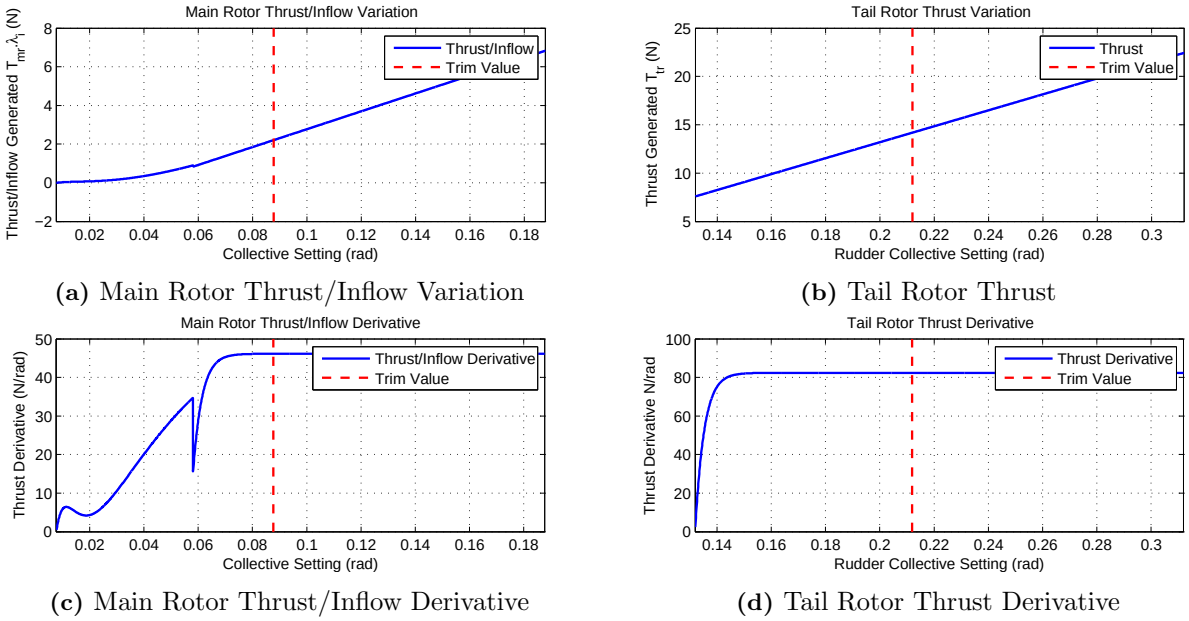

(a) Main Rotor Thrust/Inflow Variation

(b) Tail Rotor Thrust

(c) Main Rotor Thrust/Inflow Derivative

(d) Tail Rotor Thrust Derivative

Figure 3.2: Thrust Variation Results around Hover

and an analytical approximation based on the non-linear model was used instead. The mathematics from which the gain was derived is detailed in the following analysis.

The reaction torque experienced by the helicopter due to thrust was shown in Equation 2.34 and is repeated in Equation 3.6. It is this change in torque that creates the disturbance to the yaw rate system.

$$N_{mr} = \left(C_T\left(\lambda_0 - \mu_z\right) + \frac{C_{D_0}\sigma}{8}\left(1 + \frac{7}{3}\mu^2\right)\right)\left(\rho\left(\Omega R_{mr}\right)^2 \pi R_{mr}^3\right) \tag{3.6}$$

In Equation 3.6, the coefficient of thrust, C_T, is a normalized coefficient and is produced using the iterative method. For the sake of the derivation, an assumption is made that the helicopter is at trim and that the velocities are zero. This leads to a simplified equation for N_{mr}, shown in Equation 3.7.

$$N_{mr} = \left(C_T \cdot \lambda_0 + \frac{C_{D_0}\sigma}{8}\right)\left(\rho\left(\Omega R_{mr}\right)^2 \pi R_{mr}^3\right) \tag{3.7}$$

In order to compute the feed-forward gain, an equivalent linearisation to the thrust/downwash curve as a function of collective setting is required, $\frac{\partial(C_T\cdot\lambda_0)}{\partial\delta_c}\delta_c$. Replacing the coupled interaction leads to Equation 3.8 for the reaction torque.

$$N_{mr} = \left(\frac{\partial\left(C_T \cdot \lambda_0\right)}{\partial\delta_c}\delta_c + \frac{C_{D_0}\sigma}{8}\right)\left(\rho\left(\Omega R_{mr}\right)^2 \pi R_{mr}^3\right) \tag{3.8}$$

An approximation to the change in reaction torque, caused by a change in collective setting, can be represented as shown in Equation 3.9.

$$\frac{\partial N_{mr}}{\partial\delta_c} = \frac{\partial\left(C_T \cdot \lambda_0\right)}{\partial\delta_c}\left(\rho\left(\Omega R_{mr}\right)^2 \pi R_{mr}^3\right) = \frac{\partial\left(T_{mr} \cdot \lambda_0\right)}{\partial\delta_c} R_{mr} \tag{3.9}$$

To equate the derivatives and find the desired gain, a similar linearisation for the torque caused by the tail rotor (N_{tr}) based on the rudder collective command (δ_r) is needed. The can be derived using Equations 2.41 and 2.42, and is shown in Equation 3.10.

$$N_{tr} = -Y_{tr} l_{tr} = -l_{tr} C_T^{tr} \rho\left(\Omega_{tr} R_{tr}\right)^2 \pi R_{tr}^2 \tag{3.10}$$

The change in torque caused by the tail rotor based on a change in rudder collective setting, based on Equation

3.10 and the same logic as used for the collective linearisation, is shown in Equation 3.11.

$$\frac{\partial N_{tr}}{\partial \delta_r} = -l_{tr}\frac{\partial T_{tr}}{\partial \delta_r} \tag{3.11}$$

Equating the contributions, such that they negate each other, allows an estimate for the collective feed-forward gain to be approximated through Equation 3.12.

$$K_{col} = \frac{\partial N_{mr}}{\partial \delta_c} \Big/ \frac{\partial N_{tr}}{\partial \delta_r} = \frac{R_{mr}}{l_{tr}} \cdot \left(\frac{\partial \left(T_{mr} \cdot \lambda_0 \right)}{\partial \delta_c} \Big/ \frac{\partial T_{tr}}{\partial \delta_r} \right) \tag{3.12}$$

The analytical derivatives for the main rotor thrust/inflow as well as that for the tail rotor thrust are shown in Figure 3.2. Steady state derivative values can be seen to be around 46 N/rad for Collective, and around 81 for Rudder. The final gain is then $K_{\delta_{col}} = 0.4769$ rad/rad

3.3.2 Yaw Rate Control

The yaw rate control system, illustrated in Figure 3.3, is implemented as a proportional-integral (PI) controller and is shown with the feed-forward input from the collective setpoint that was discussed in the previous section. The system contains limits on the commanded yaw rate, as well as a limit on the commanded rudder collective

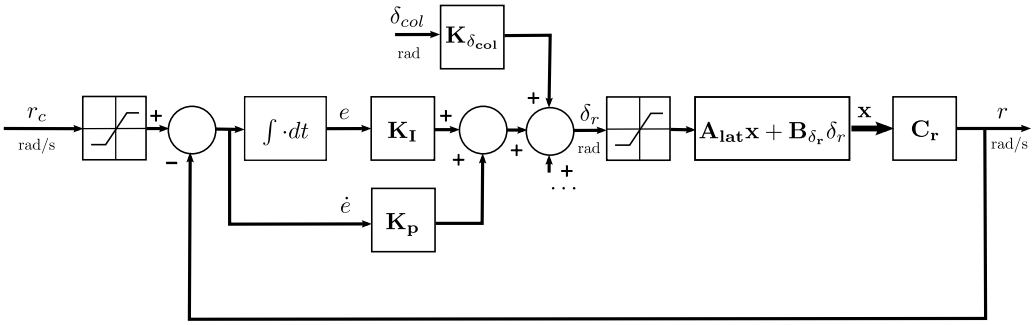

Figure 3.3: Yaw Rate Control System

setpoint (implemented as a limit on the control authority of the controller, before the trim setpoint is added to the final value). Included, but not shown, is anti-windup logic for the integrator, where the integrator contribution is limited to values less than the saturation limit.

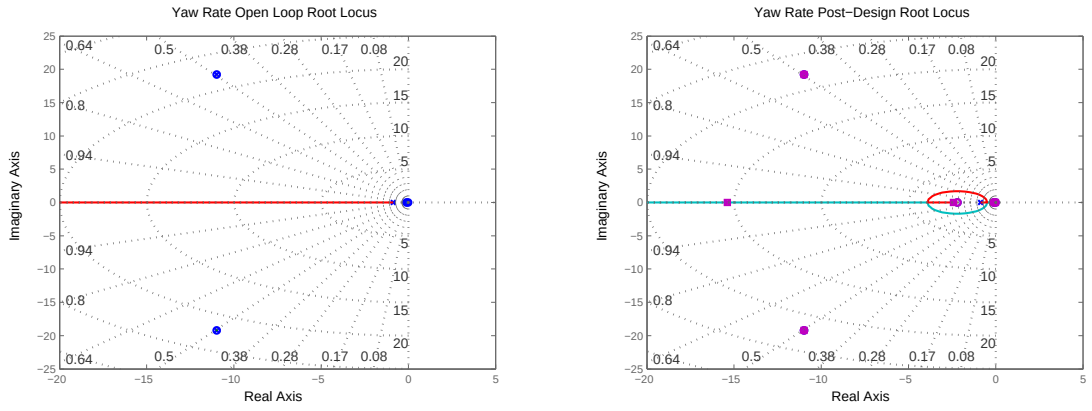

(a) Root Locus **(b)** Root Locus with Dynamic Compensation

Figure 3.4: Yaw Rate Design Root Loci

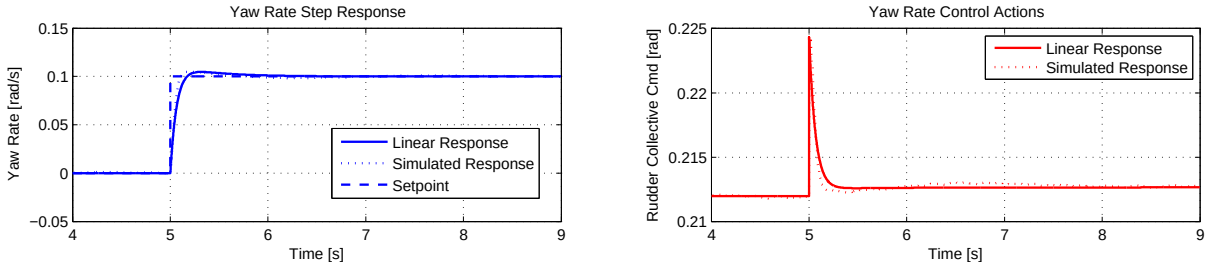

(a) Yaw Rate Step Response

(b) Yaw Rate Control Signal

Figure 3.5: Yaw Rate Control Responses

Considering the root loci shown in Figure 3.4, it can be noted that the yaw rate plant is dominated by a single, linear pole that is stable for all linear gains. The inclusion of an active integrator caters for increased performance while rapidly attenuating disturbances, allowing the desired aggressive behaviour to be achieved. This design causes oscillation at low gains, but damped, aggressive responses at high gains. The responses shown were developed using the PI controller described in Equation 3.13.

$$K_r = \frac{0.12324\,(s + 2.2)}{s} \tag{3.13}$$

The linear plots shown in Figure 3.5a where generated using an augmented state-space system. The **A** and **B** matrices describing these are detailed in Equations 3.14 and 3.15.

$$\mathbf{A_r} = \begin{bmatrix} A_{lat} & 0 \\ -C_r & 0 \end{bmatrix} \tag{3.14}$$

$$\mathbf{B_r} = \begin{bmatrix} B_{\delta_{tail}} \\ 0 \end{bmatrix} \tag{3.15}$$

The closed loop yaw rate dynamics of the system can then be linearly described by the state-space system shown in Equation 3.16 (where the yaw rate output is determined by $y = \mathbf{C}_r\mathbf{x}$).

$$\dot{\mathbf{x}} = \left(\mathbf{A_r} - \mathbf{B_r}\begin{bmatrix} 0 & 0 & 0 & K_p & 0 & -K_I \end{bmatrix}\right)\mathbf{x} + \left(K_p\mathbf{B_r} + \begin{bmatrix} 0 \\ 1 \end{bmatrix}\right)\mathbf{r_c} \tag{3.16}$$

This resultant root locus and step response was shown in Figures 3.4b and 3.5a respectively. The linear system was found to match well with the non-linear simulation for lower frequencies, illustrating a high-bandwidth and well damped system.

3.3.3 Heading Control

The design of the heading control system relies on the design of the yaw rate system, as the successively closed nature of the system ensures that the dynamics of the heading open loop plant are primarily stipulated by the design of the closed loop yaw rate plant. The natural integrator in the heading plant, coupled with the artificial integrator in the yaw rate controller, ensures that the system will always have asymptotic tracking with zero steady state error, provided that no significant bias exists on the yaw rate measurement. This allows, given the fast yaw rate response, for fast and aggressive heading control to be implemented using a simple proportional feedback scheme, the diagram for which is illustrated in Figure 3.6.

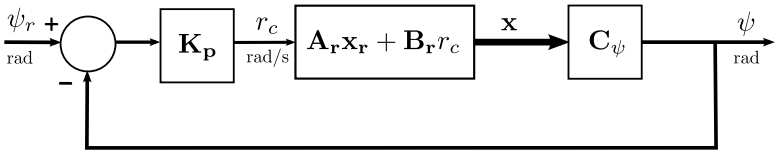

Figure 3.6: Heading Control System

In order to implement the linear heading system, the closed loop yaw rate system, illustrated in Equation 3.16, must be augmented with the heading state. This leads to the state-space matrices shown in Equations 3.17 and 3.18 (where $\mathbf{A_r^*}$ and $\mathbf{B_r^*}$ are the closed loop equivalent matrices).

$$\mathbf{A}_\psi = \begin{bmatrix} A_r^* & 0 \\ C_r & 0 \end{bmatrix} \tag{3.17}$$

$$\mathbf{B}_\psi = \begin{bmatrix} B_r^* \\ 0 \end{bmatrix} \tag{3.18}$$

The closed loop response can then be simulated using Equation 3.19.

$$\dot{\mathbf{x}} = \left(\mathbf{A_r^*} - \mathbf{B_r^*} \begin{bmatrix} 0 & K_\psi \end{bmatrix} \right) \mathbf{x} + K_\psi \mathbf{B}_\psi \psi_\mathbf{c} \tag{3.19}$$

The root locus illustrated in Figure 3.7a implies stable operation of the heading control system for all gains. However, due to unmodelled vibration on the tail rotor, K_ψ was chosen to be 2.7 $rad/rad \cdot s$. This provided a rapid and well damped response from the controller.

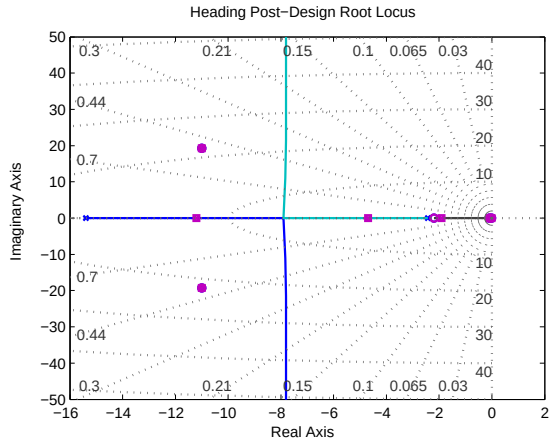

(a) Heading Root Locus

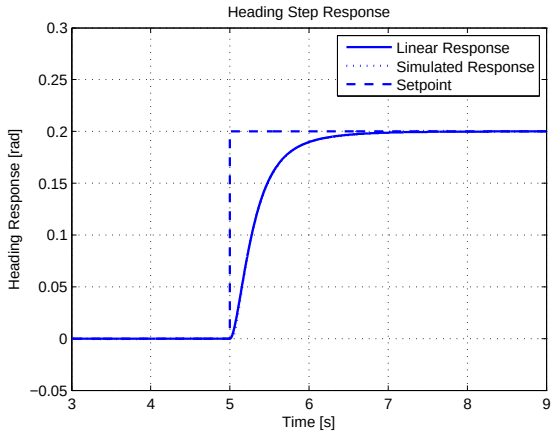

(b) Heading Step Response

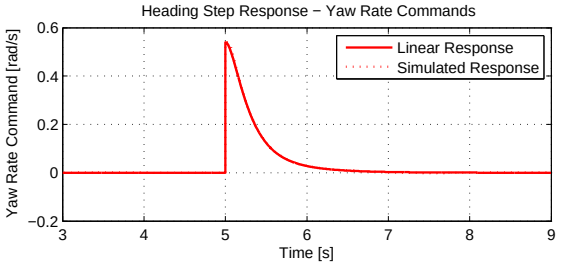

(c) Heading Loop - Yaw Rate Loop Control Action

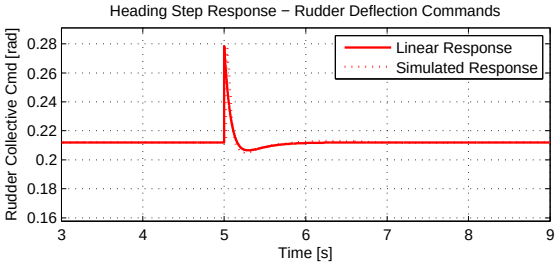

(d) Heading Loop Control Action

Figure 3.7: Heading Control Design, Setpoint Tracking Response and Control Responses

3.4 Lateral Control

The lateral position control scheme depends on a series of successively implemented controllers. On the outer loop, a position error commands a velocity control loop; the velocity control loops commands a change in the required roll angle, and the roll angle commands the change in roll rate. The roll rate controller directly commands the lateral cyclic actuator. This is intuitive as a similar perspective is experienced from a pilot's observational viewpoint.

The flapping angle contribution acts as an additional state that cannot be directly controlled due to the unavailability of the required measurements. To overcome this, the control system is defined in such away as to ensure that the loci emanating from the variable, unmeasurable flapping poles are pushed further into the left hand plane, ensuring stability in the system's operation. The implementation of this is in the roll rate controller, which is discussed in Section 3.4.1.

The design of the lateral control system builds on the state-space system developed in the heading control system. This ensures that any induced dynamics from the other controllers are accounted for in the design. This section begins with a discussion on the roll rate controller, before proceeding to the roll angle, lateral velocity and lateral position controllers.

3.4.1 Roll Rate Controller

The design of the roll rate controller defines a large part of the helicopter's operational capability, and a poorly designed roll rate controller can negatively impact the helicopter's stability, as well as its performance. Accounting for the flapping-roll rate poles provides a challenge in the design task, as not only are the pole positions of the coupled mode relatively unknown, the flapping angle state is not directly measurable. Additionally, the dynamics of the flapping angles are such that online estimation of the flapping angle values may be impractical and imprecise.

In order to combat this, feedback is performed using roll rate measurements alone. The control structure is designed so that the controller poles dominate, pushing the loci of the open loop flapping/roll rate poles further into the left hand plane, ensuring stability despite the uncertainty surrounding the precise location of the flapping poles. This controller makes use of a passive filter, an integrator and a gain as shown in the structure illustrated in Figure 3.8.

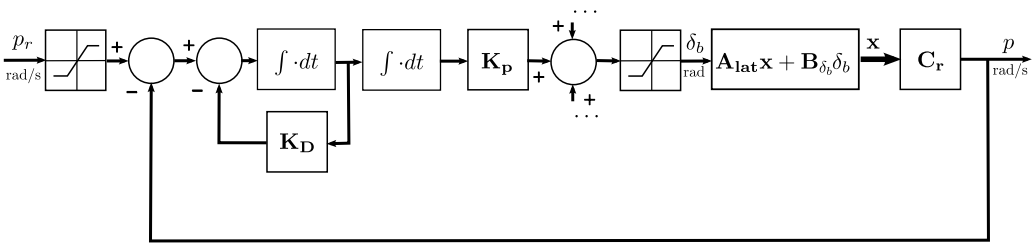

Figure 3.8: Roll Rate Control System

To illustrate the operation of the controller, a pre- and post-design root locus is shown for the controller in Figure 3.9. The first figure illustrates the root locus without the presence of the controller. The loci illustrate stability in open loop but highly oscillatory behaviour with increased proportional feedback (although in real

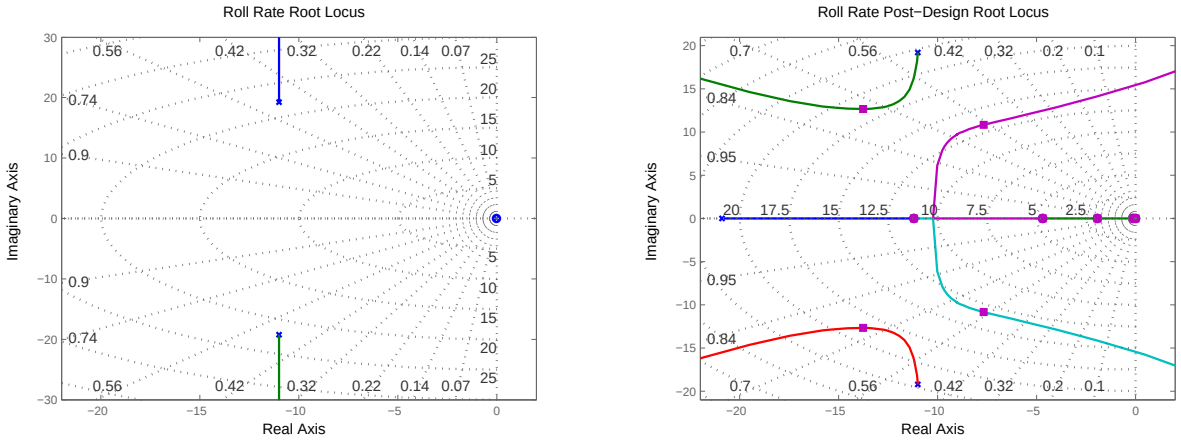

(a) Root Locus **(b)** Root Locus with Dynamic Compensation

Figure 3.9: Roll Rate Root Locus Design

world operation the effects could be entirely different, as the pole positions are not precisely known). The implementation of the controller, as seen in Figure 3.9b, forces the loci trajectory originating at the open loop pole positions further into the left hand plane, instead causing the dominant response to be the action of the controller (the pole positions of which are known). This ensures stable behaviour in the face of uncertainty.

The statespace matrices used in the design of the roll rate controller are augmented versions of the closed loop heading control system, and are described in Equations 3.20 and 3.21.

$$\mathbf{A}_p = \begin{bmatrix} A_\psi & 0 & 0 \\ 0 & 0 & 1 \\ -C_p & 0 & -K_{DR} \end{bmatrix} \tag{3.20}$$

$$\mathbf{B}_p = \begin{bmatrix} B_{lat} \\ 0 \\ 0 \end{bmatrix} \tag{3.21}$$

The closed loop equation, using these matrics, is illustrated in Equation 3.22.

$$\dot{\mathbf{x}} = \left(\mathbf{A}_p + \mathbf{B}_p \begin{bmatrix} 0 & 0 & K_{PR} \end{bmatrix}\right) \mathbf{x} + \begin{bmatrix} 0 \\ 1 \end{bmatrix} p_c \tag{3.22}$$

To implement the system, a controller pole of $K_{DR} = 22.9$ (implying a fairly high bandwidth of around 3.3 Hz),

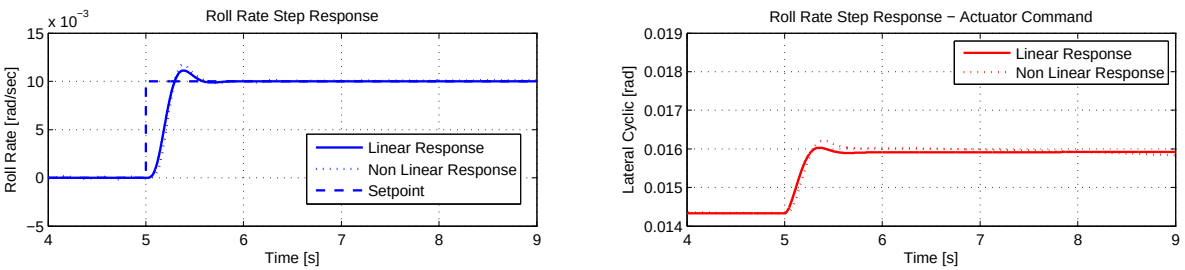

(a) Roll Rate Step Response **(b)** Roll Rate Step Response - Actuator Command

Figure 3.10: Control Responses

and a gain of $K_{PR} = 19.9$ (equivalent to an effective gain of 0.86917) was found to stabilize the system, whilst creating minimal oscillations. The response is illustrated in Figure 3.10, alongside the actuator control action.

3.4.2 Roll Angle Controller

The roll angle controller is a simple proportional controller that gives a roll rate command to the roll rate controller, the structure of which is shown in the diagram below. The addition of the roll angle trim condition, ϕ_t, was included to reduce transients when initiating the system.

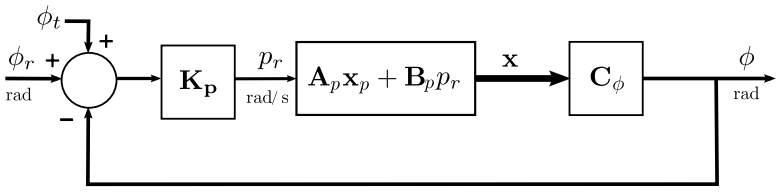

Figure 3.11: Roll Angle Control Structure

The controller, with a gain of $K_\phi = 3.3\ rad/rad.s$, has a design root locus shown in Figure 3.12a. The loop is theoretically stable for low gains, with the response primarily dominated by the poles occurring on the path emanating from the roll rate controller's closed loop pole locations. The exact position of the poles on the loci originating with the flapping poles is still unknown, but pushes further into the left hand plane, implying stability despite potential variability in the pole location.

The roll angle response, illustrated in Figure 3.12b, shows fast tracking with a mild overshoot, and similar

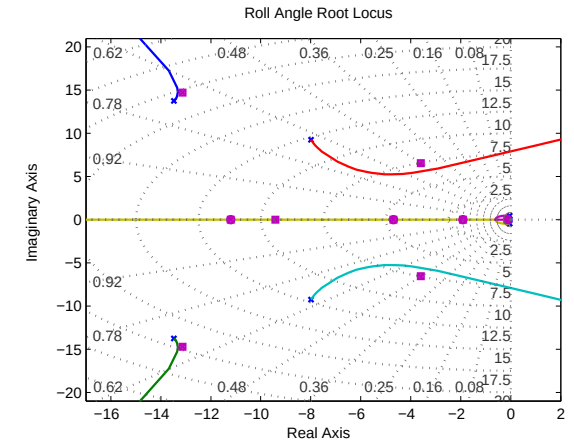

(a) Root Locus Plot

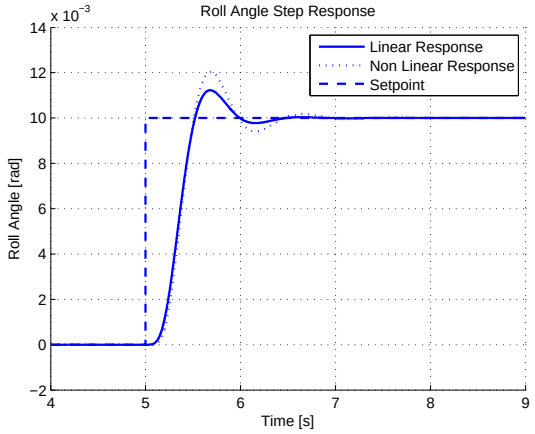

(b) Closed Loop Step Response

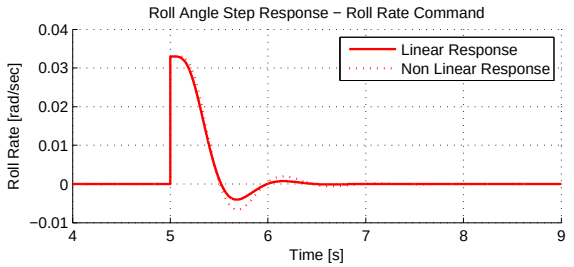

(c) Closed Loop Step Response - Roll Rate Command

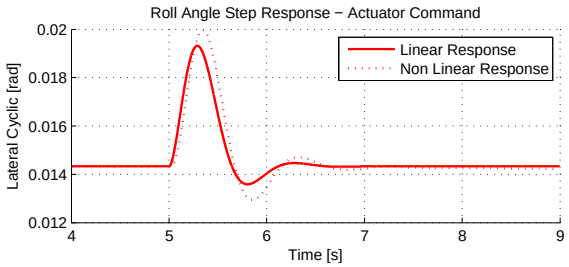

(d) Closed Loop Step Response - Actuator Command

Figure 3.12: Roll Angle Control Design

performance in both linear and non-linear control systems. Actuator and lower loop commands are displayed in Figures 3.12d and 3.12c.

3.4.3 Lateral Velocity Controller

Lateral velocity control is implemented using a PI controller, illustrated in Figure 3.13. Saturation blocks on the controller ensure that the helicopter remains within the bounds of its lateral flight trim condition, while the integrator ensures that the required velocity command is met with zero steady state error. The system is limited to low bank angles to ensure that underlying non-linearities are not aggravated.

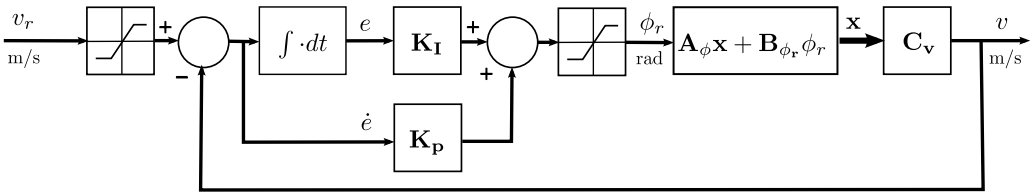

Figure 3.13: The Lateral Velocity Controller Structure

The velocity controller was implemented with a proportional gain of $K_p = 0.14413$ and a zero at 0.1838 (equivalent to an integrator gain of $K_I = 0.026491$). The state space system representing the closed loop roll angle controller was augmented with an additional state to model the integrator, shown in Equation 3.23.

$$\mathbf{A}_v = \begin{bmatrix} A_\phi & B_\phi \\ \underline{0} & 0 \end{bmatrix} \tag{3.23}$$

$$\mathbf{B}_v = \begin{bmatrix} B_\phi \\ {}^{K_I}/_{K_p} \end{bmatrix} \tag{3.24}$$

The final closed loop system can then be represented as shown in Equation 3.25.

$$\dot{\mathbf{x}} = \left(\mathbf{A}_v + \mathbf{B}_v \begin{bmatrix} -K_p & \underline{0} \end{bmatrix}\right)\mathbf{x} + K_p\mathbf{B}_v v_r \tag{3.25}$$

The root loci used in the design process are shown in Figure 3.14. The controller gains are small (due to the

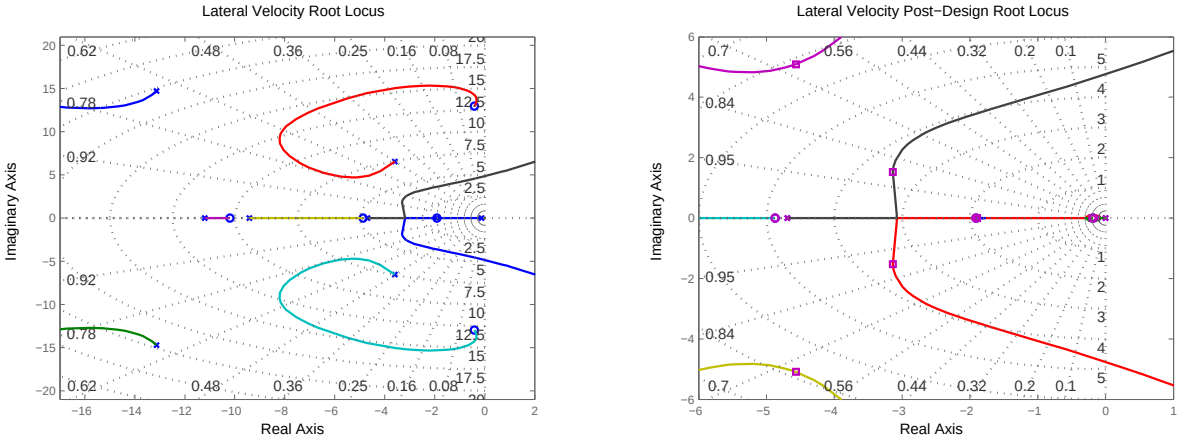

(a) Lateral Velocity Root Locus

(b) Root Locus with Dynamic Compensation

Figure 3.14: The Root Locus Design for the Lateral Velocity Control System

large open loop gains between roll angle and lateral velocity), and fairly fast system poles dominate the response. Illustrated in Figure 3.15a, the velocity controller response shows fairly rapid tracking of velocity steps with mild overshoot, and a ±2% settling time of around 1 second.

The design of the lateral velocity controllers is primarily limited by the implementation of the lower loops, as well as the estimation of the velocity state. In this implementation, the controller made use of GPS velocity estimates, which typically had a 0.1 m/s white noise on the measurement alongside a 100ms delay (updated at 10Hz). These measurements were fed into an estimator without accelerometer propagation (as the noise on the accelerometer measurements was greatly increased due to the vibration on the helicopter).

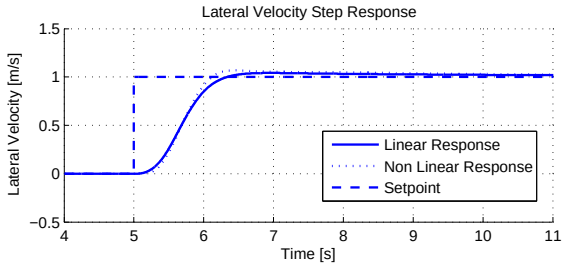

(a) Lateral Velocity Step Response

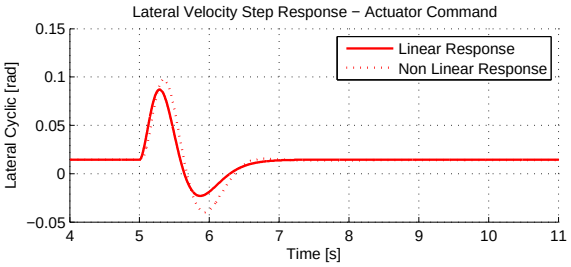

(b) Lateral Velocity Step Response - Actuator Command

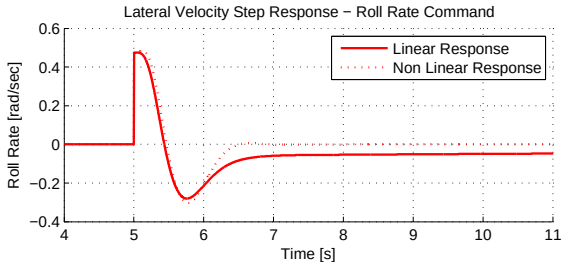

(c) Lateral Velocity Step Response - Roll Rate Command

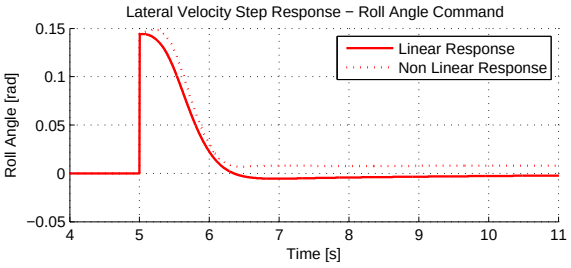

(d) Lateral Velocity Step Response - Roll Angle Command

Figure 3.15: Lateral Velocity Control Responses

3.4.4 Lateral Position Controller

The controller structure, shown in Figure 3.16, makes use of a proportional controller as well as a direct feed forward link from the reference velocity (shown for the purpose of illustration as the derivative of the reference signal). The reference, Y_r, is the (N, E) reference coordinate transformed through the current heading angle to be relative to the body axis (X, Y).

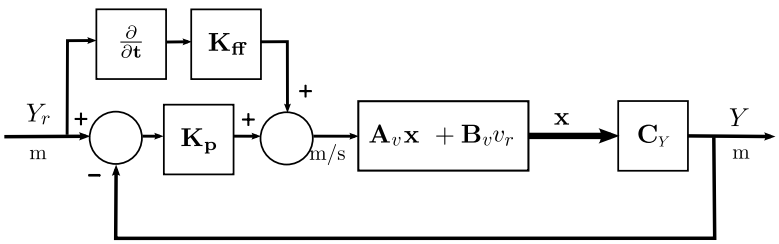

Figure 3.16: The Lateral Position Control Structure

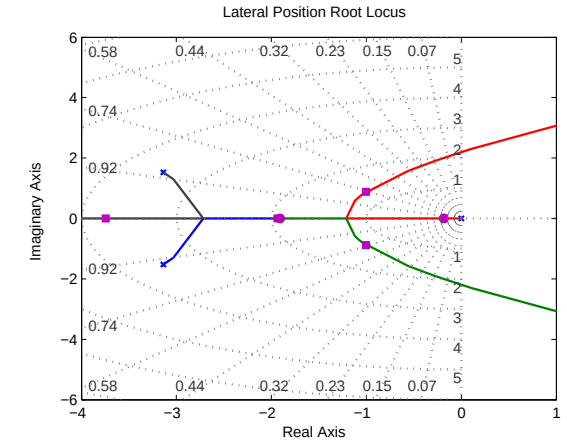

(a) Lateral Position Design Root Locus

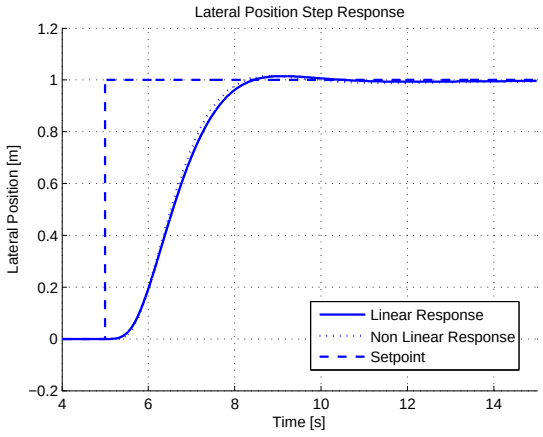

(b) Lateral Position Step Response

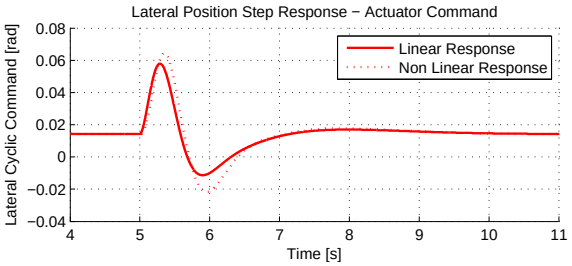

(c) Lateral Position Step Response - Actuator Command

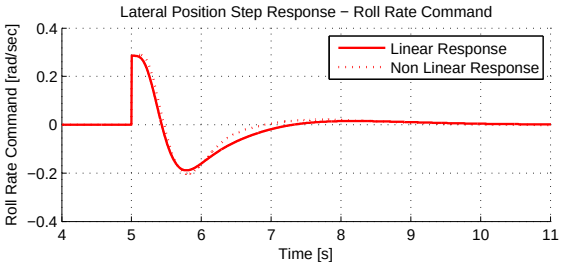

(d) Lateral Position Step Response - Roll Rate Command

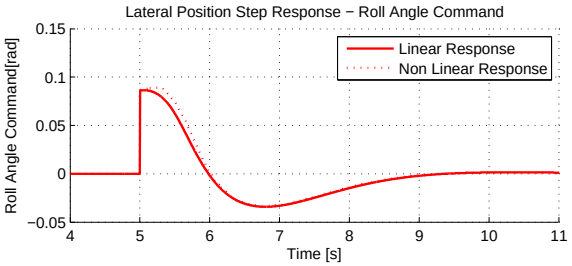

(e) Lateral Position Step Response - Roll Angle Command

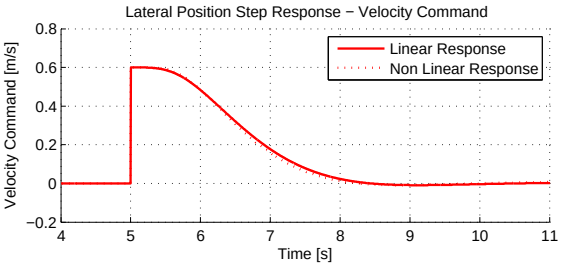

(f) Lateral Position Step Response - Velocity Command

Figure 3.17: Lateral Position Control Design

The purpose of the reference velocity feed-forward link is to facilitate the absolute tracking of a reference signal moving with constant velocity. The gain K_{ff} is illustrated for completeness and typically holds a value of one in regular circumstances. The design and implementation of the reference velocity feed-forward signals is discussed in detail in Section 3.7.

The integrator in the velocity controller, as well as the implicit integration between the states, allows the use of a proportional gain to precisely and asymptotically control the position. Fairly modest gains were chosen for the position control as GPS delays, in practice on the order of around 0.15 seconds, cause oscillations in simulation for large gains.

The controller was found to operate well with a gain of $K_p = 0.6$, and was designed according to the root locus and response shown in Figure 3.17. The control response was designed to be fast as possible without causing oscillation in full non-linear simulation. The response, seen in Figure 3.16, illustrates a fast, rapidly attenuating control system with minimal overshoot.

3.5 Heave Control Systems

Heave control, alternatively referred to as altitude control, makes use of the collective input to command the desired altitude or heave velocity. The design of this system is important to ensure good disturbance rejection in the altitude loops, as well as to minimize the altitude loss in aggressive forward flight. With regard to landing controllers, the heave and heave rate controllers are required to have a relatively high bandwidth, in order to minimize the disturbance due to ground effect.

In this section the design of the heave controllers is detailed, alongside a means of reducing the altitude loss when in aggressive forward flight. Altitude control is implemented as a successively closed control structure, building on the heave rate control system.

3.5.1 Heave Rate Controller

The heave rate control system makes use of a proportional-integral control law, fed directly into the collective input. The structure for the heave rate controller is illustrated in Figure 3.18.

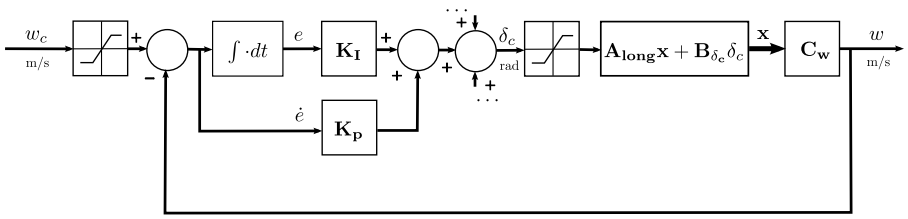

Figure 3.18: Heave Rate Control System

Considering the linear model shown in Section 3.2, it can seen that the heave rate is dominated by a single, linear pole. This is illustrated in the root locus shown in Figure 3.19a. The use of a PI controller allows for accurate asymptotic tracking of references as well as ensuring that the trim condition will be met in light of modelling uncertainties. The controller is illustrated in Equation 3.26.

$$K_w(s) = \frac{-0.04\,(s+0.9)}{s} \tag{3.26}$$

To encapsulate the new controller dynamics, the state space system must be augmented with the controller integrator states show in Equations 3.27 and 3.28.

$$\mathbf{A_w} = \begin{bmatrix} A_{long} & 0 \\ -C_w & 0 \end{bmatrix} \tag{3.27}$$

$$\mathbf{B_w} = \begin{bmatrix} B_{\delta_{col}} \\ 0 \end{bmatrix} \tag{3.28}$$

The dynamics of the closed loop system can then be described using Equation 3.29

$$\dot{\mathbf{x}} = \left(\mathbf{A_w} - \mathbf{B_w}\begin{bmatrix} 0 & 0 & K_p & 0 & 0 & -K_I \end{bmatrix}\right)\mathbf{x} + \left(K_p\mathbf{B_w} + \begin{bmatrix} 0 \\ 1 \end{bmatrix}\right)\mathbf{r_c} \tag{3.29}$$

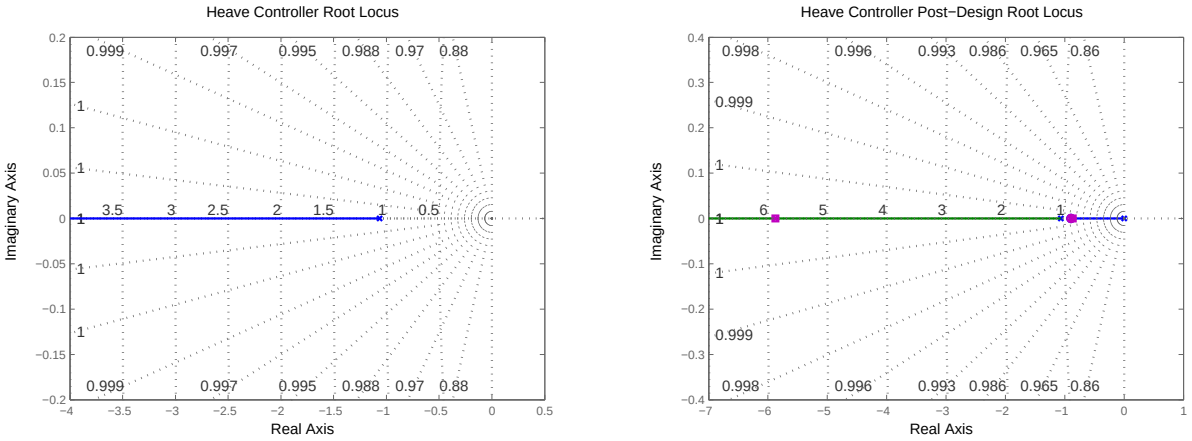

(a) Heave Rate Root Locus

(b) Heave Rate Root Locus with Dynamic Compensation

Figure 3.19: Heave Rate Control Design

The root locus plots shown in Figure 3.19, illustrates a simple linear system that, when implemented with a PI controller containing a zero below the primary system pole, causes no overshoot or oscillatory behaviour but ensures absolute tracking with a fast response. The response is designed to be well below the dynamic capabilities of the system to ensure stability and minimal tracking deviations when interacting with ((and disturbing) the other controllers.

The controller response is illustrated in Figure 3.20, alongside the collective command given by the controller. The system shows a fast tracking response to a velocity step, settling to $\pm 2\%$ within 1 second, with no overshoot. In the hardware implementation, the controller was implemented with respect to the altitude-rate measurement ($\dot{D}$) to reduce tracking errors and altitude loss in forward flight. Around hover, this is approximately equivalent to w and only significantly deviates for large roll or pitch angles ($\theta, \phi > 20°$).

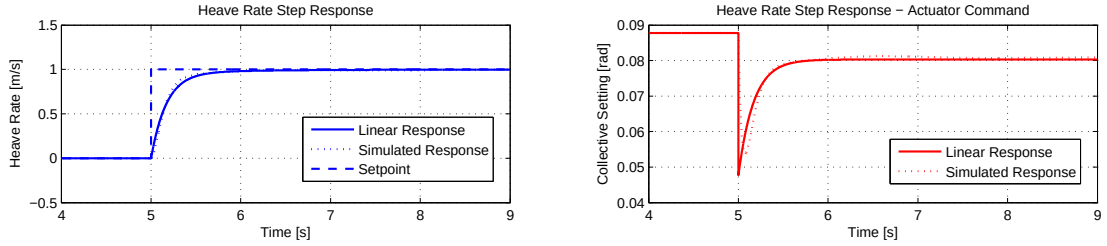

(a) Heave Rate Step Response

(b) Heave Rate Control Signal

Figure 3.20: Heave Rate Control Response

3.5.2 Altitude Control

The altitude feedback control system is implemented as a simple proportional feedback, illustrated in the diagram shown in Figure 3.21. The altitude control system works by directly commanding the heave rate control system. The integrator in the heave rate control system, coupled with the natural integration in the altitude state, ensures that the closed loop altitude system has absolute tracking.

In practice, GPS drift and update delays limit the gains that can be practically used with such a control system. However, in theory, larger gains are only acceptable provided fast, high bandwidth measurement updates are

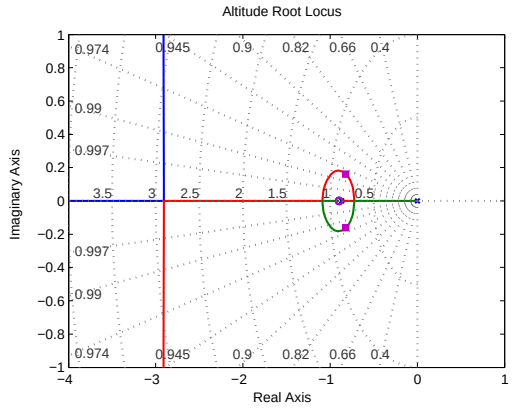

(a) Altitude Root Locus

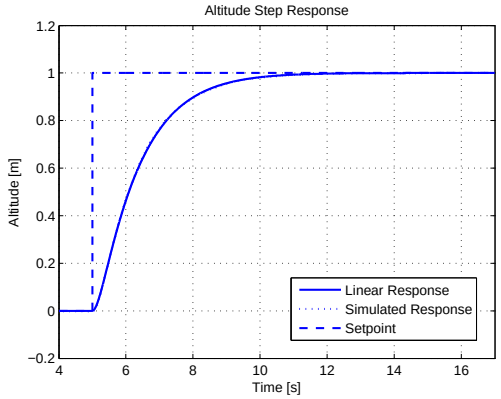

(b) Altitude Step Response

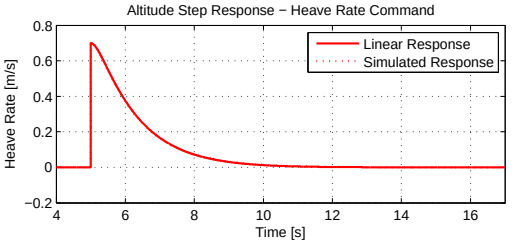

(c) Altitude Loop - Heave Rate Loop Control Action

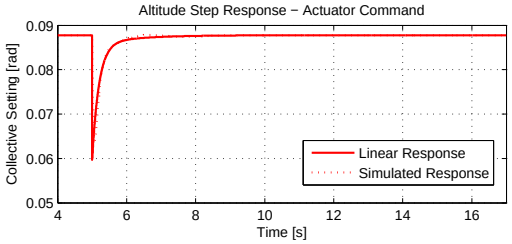

(d) Altitude Loop Control Action

Figure 3.22: Altitude Control Design, Setpoint Tracking Response and Control Responses

available.

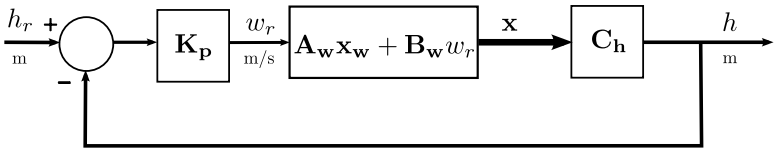

Figure 3.21: Heave Control System

In order to implement the linear heave state-space system, the system must be augmented with the heave state. This leads to the matrices shown in Equations 3.30 and 3.31 (where $\mathbf{A_w}$ and $\mathbf{B_w}$ are the matrices corresponding to the heave rate closed loop plant)

$$\mathbf{A_h} = \begin{bmatrix} A_w & 0 \\ C_w & 0 \end{bmatrix} \tag{3.30}$$

$$\mathbf{B_h} = \begin{bmatrix} B_r \\ 0 \end{bmatrix} \tag{3.31}$$

The closed loop dynamics can then be encapsulated in the linear system shown in Equation 3.32,

$$\dot{\mathbf{x}} = \left(\mathbf{A_w} - \mathbf{B_w} \begin{bmatrix} 0 & K_h \end{bmatrix}\right) \mathbf{x} + K_h \mathbf{B_w w_r} \tag{3.32}$$

The altitude controller gain, K_h, was chosen to be 0.7. This provided a rapid and well damped response from the controller. To minimize disturbance to the other controllers, a slew rate limiter (of 1 m/s^2) was implemented to mitigate significant disturbances to the lateral and heading plants when undergoing a large altitude step.

3.5.3 Reducing Altitude Disturbance in Aggressive Forward Flight

Altitude disturbance in forward flight is caused by the new orientation of the tip-path-plane (and the resulting re-orientation of the thrust vector) when undergoing planar accelerations. Fast or aggressive control manoeuvres, such as those that would occur in a fairly large velocity step, can cause large altitude deviations for low altitude control law gains. In order to mitigate the effect, the estimated roll and pitch angles are fed forward to the controller in such a way as to modify the collective setting of the helicopter. The required increase in thrust can be analytically determined based on the following considerations.

At hover, the thrust produced must equate the gravitational force experienced, i.e, $T_{hover} = mg$. While in forward flight however, the thrust, assumed perpendicular to the tip-path-plane, must produce a thrust of $T = mg/\cos\Theta$ (where Θ is the roll/pitch angle or intersection angle with the NE plane). The increase in required thrust can then be represented as,

$$T = T_{hover} + \Delta T \tag{3.33}$$

The difference in thrust, ΔT, can then be shown to be,

$$\Delta T = \frac{mg}{\cos\Theta} - mg = T_{hover}\left(\sec\Theta - 1\right) \tag{3.34}$$

Presuming linearity in thrust production, the thrust produced, T_{hover}, can be replaced with the current collective setting at hover, δ_{col}. Replacing $\sec\Theta$ with its second order taylor series approximation, and replacing Θ with a small angle approximation for roll and pitch ($\Theta = \sqrt{\phi^2 + \theta^2}$) gives,

$$\Delta T = \delta_{col}^{ff} = \frac{1}{2}\delta_{col}\left(\phi^2 + \theta^2\right) \tag{3.35}$$

Gavrilets [34] in his work, used the angle commands as opposed to the angle measurements, likely for the additional phase advance. As the system is controlled relative to the altitude measurement, this was found to

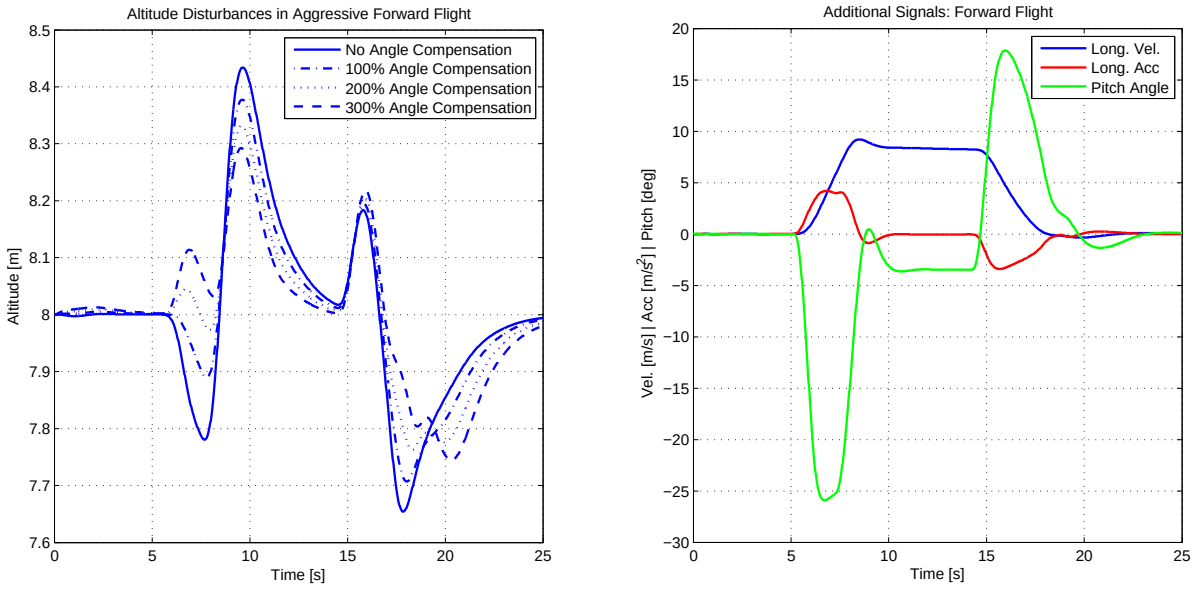

(a) Altitude Response during Aggressive Forward Flight

(b) Additional Signals

Figure 3.23: Angle Compensation Effect on Altitude Disturbance Reduction

induce unwanted non-linearities, and the estimator values were used instead. The influence of the final feed forward link, referred to as Angle Compensation on Thrust, is shown in Figure 3.23a, with varying levels of compensation.

The feed forward link illustrated a slight reduction (between 13% and 16%) in minor altitude loss for accelerations exceeding 4 $m.s^{-2}$ when used with the standard gain. Increasing the gain was found to add increased reductions when accelerating, but was found to excite non-linearities when decelerating. The best response was found to be when a gain of 200% was implemented as it provided increased altitude loss reduction, while exciting only minor non-linearities on the deceleration profile (resulting in a reduction in altitude deviation of between 20% and 30%). Additional Signals are shown in Figure 3.23b, illustrating the velocity command given to the helicopter, the acceleration experienced by the helicopter, as well as the pitch angle.

3.6 Longitudinal Control

The structure for longitudinal control is equivalent to that for the lateral control system. Notable differences lie in the increased inertia of the plant, as well as the decrease in profile drag due to the smaller surface area. These factors result in moderately different controller gains for the longitudinal plant when compared to the lateral plant. The control laws were designed in such a way as to maximise performance without compromising on the stability of the plant.

3.6.1 Pitch Rate Controller

To account for the induced dynamics, the pitch rate state space is includes the model of the heave system. The controller structure used on this plant is identical to that used on the lateral plant, barring alternate gains due to the increased inertia. The controller makes use of a passive filter, integrator and a linear gain as illustrated in the structure shown in Figure 3.24.

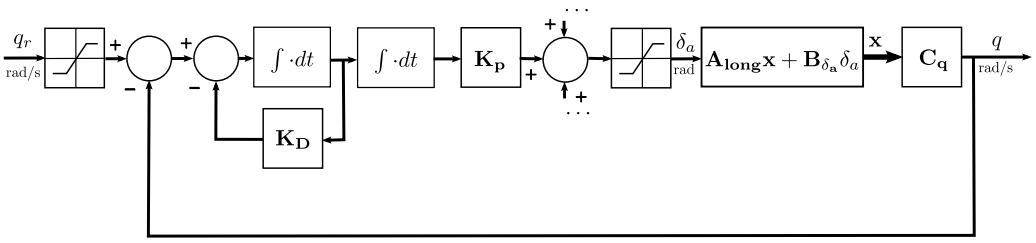

Figure 3.24: Pitch Rate Control System

As was the case with the lateral plant, the longitudinal plant needs to be augmented with the integrator states to ensure accurate linear modelling of the control system. This results in the new state-space matrices, shown in Equations 3.36 and 3.37.

$$\mathbf{A}_q = \begin{bmatrix} A_D & 0 & 0 \\ 0 & 0 & 1 \\ -C_q & 0 & -K_D \end{bmatrix} \tag{3.36}$$

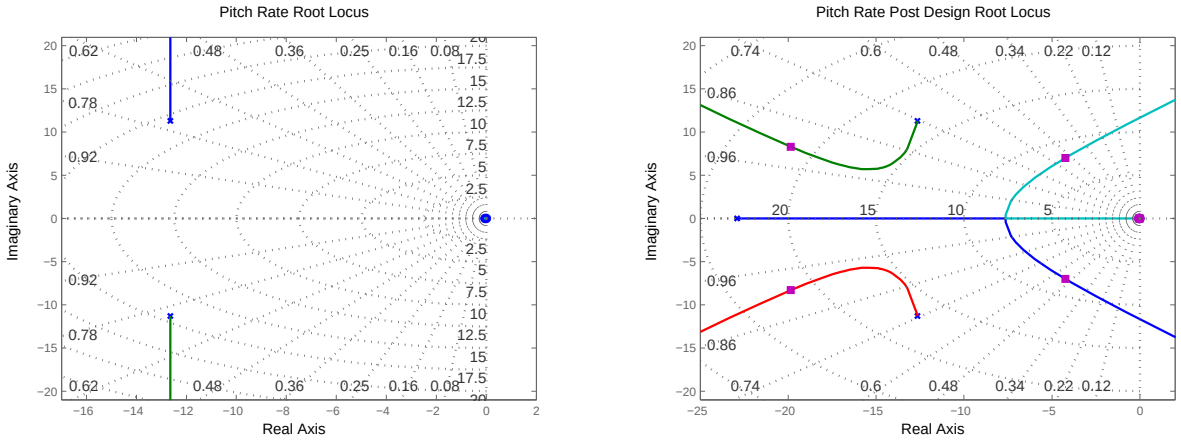

(a) Pitch Rate Root Locus

(b) Pitch Rate Root Locus with Dynamic Compensation

Figure 3.25: Pitch Rate Root Locus Design

$$\mathbf{B}_q = \begin{bmatrix} B_{long} \\ 0 \\ 0 \end{bmatrix} \tag{3.37}$$

The closed loop equation based on these matrices is shown in Equation 3.38.

$$\dot{\mathbf{x}} = \left(\mathbf{A}_q + \mathbf{B}_q \begin{bmatrix} 0 & 0 & K_P \end{bmatrix} \right) \mathbf{x} + \begin{bmatrix} 0 \\ 1 \end{bmatrix} q_c \tag{3.38}$$

To implement the system, a controller pole of $K_{DR} = 22.9$ (implying a fairly high bandwidth), and a gain of $K_{QR} = 17.16$ (equivalent to an effective gain of 0.74956) was found to stabilize the system, whilst creating minimal oscillations. The root locus, before and afterwards, is shown in Figure 3.25.

The response, illustrated in Figure 3.26, shows a rise time of around 0.5s and an overshoot of around 20%. The increased inertia causes a longer settling time, when compared to the lateral controller and performance is maximised to ensure minimal settling times and overshoot. Absolute tracking is ensured through the implementation of the integrator, and allows for the rapid trimming of the aircraft to hover. The non-linear simulation was found to adequately match the linear simulation, with similar actuator and pitch rate performance.

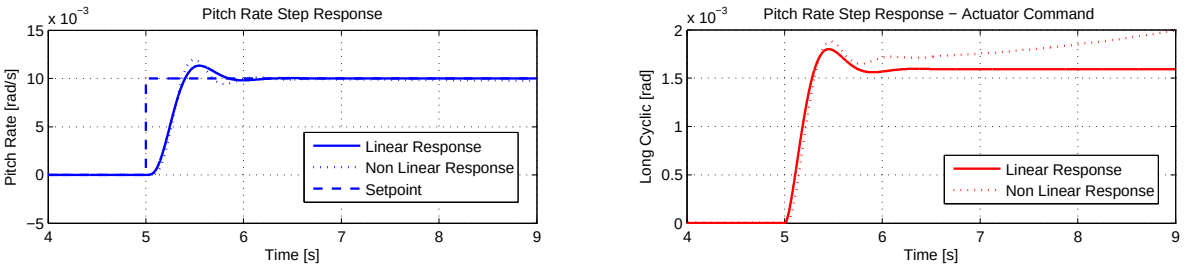

(a) Pitch Rate Step Response

(b) Pitch Rate Step Response - Actuator Command

Figure 3.26: Pitch Rate Response

3.6.2 Pitch Angle Controller

The pitch angle controller is a proportional controller that gives a pitch rate command to the pitch rate controller. The structure of the controller, identical to the roll angle controller in all but the gain, is shown in Figure 3.27. The controller makes use of proportional feedback to command the pitch rate controller.

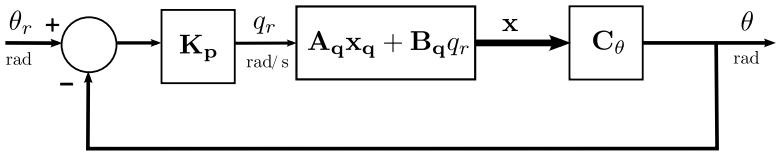

Figure 3.27: Pitch Angle Control Structure

The controller, with a gain of $K_\theta = 2.3 rad/rad.s$, has a design root locus shown in Figure 3.28a. The controller gains were chosen to provide a fast settling time and well-damped response. The controller is theoretically stable for low gains, and the chosen response shows asymptotic tracking behaviour with little overshoot.

The distribution of the poles in the pitch angle controller differs slightly from that in the roll angle controller, largely caused by the increased inertia and the greater filter bandwidth chosen.

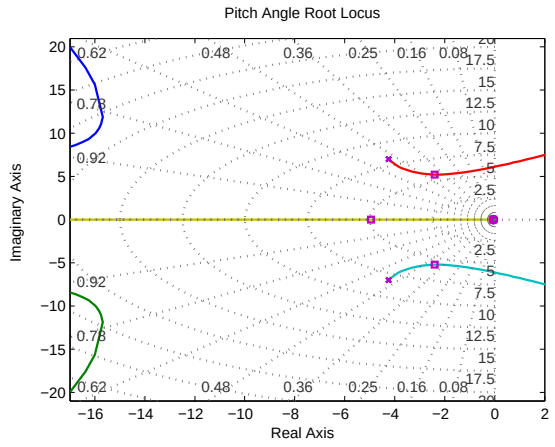

(a) Root Locus Plot

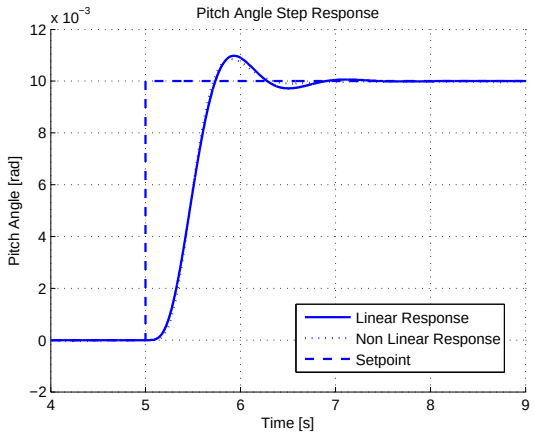

(b) Closed Loop Step Response

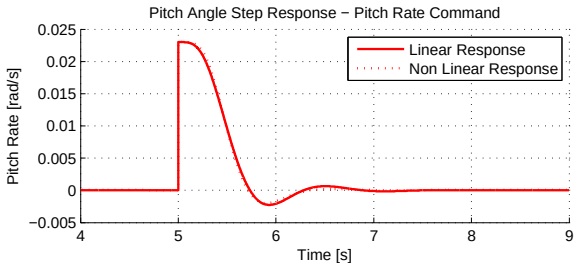

(c) Closed Loop Step Response - Pitch Rate Command

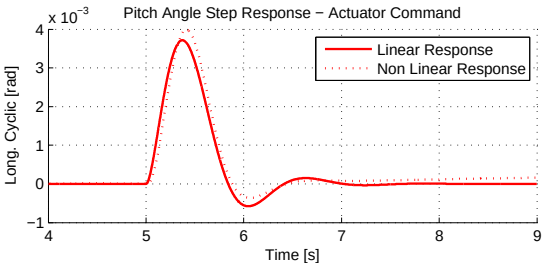

(d) Closed Loop Step Response - Actuator Command

Figure 3.28: Pitch Angle Control Design

3.6.3 Longitudinal Velocity Controller

The Longitudinal velocity controller, like the lateral velocity controller, makes use of a PI controller but has the addition of a slew rate limiter to limit the forward acceleration. The controller design is illustrated in Figure 3.29.

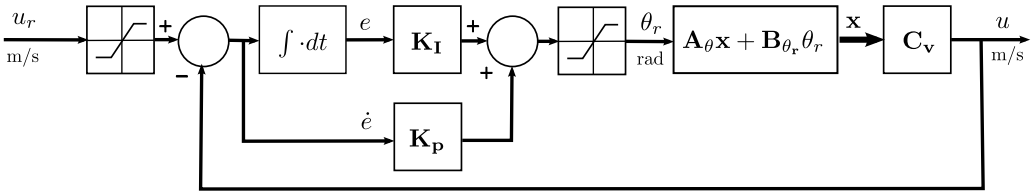

Figure 3.29: The Longitudinal Velocity Controller Structure

The longitudinal velocity controller was implemented with a proportional gain of $K_p = -0.10749$ and a zero at 0.15 (equivalent to an integrator gain of $K_I = -0.016123$). The state space system from before was augmented with an additional state to include the integrator. The root loci used in the design process are shown in Figure 3.30, where the post design root locus is enlarged so as to see the dominant poles.

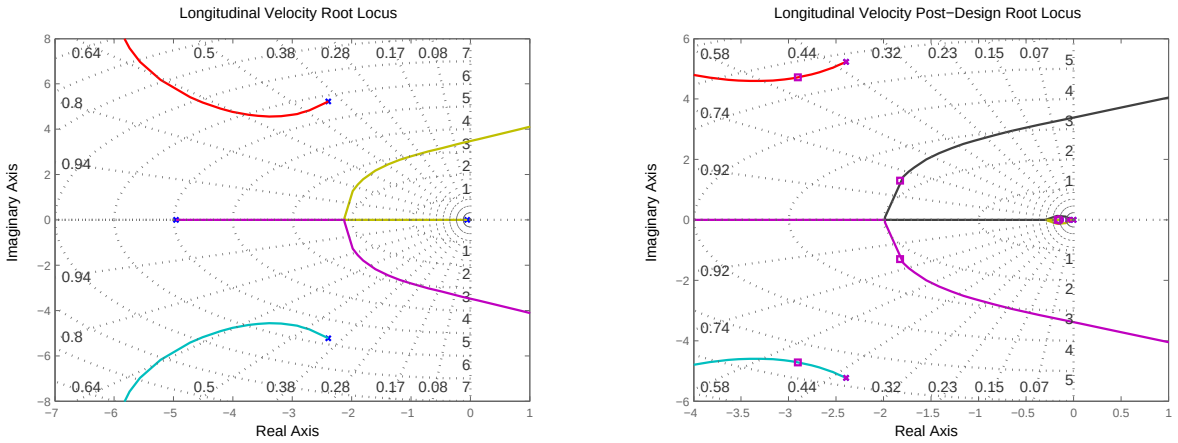

(a) Root Locus

(b) Root Locus with Dynamic Compensation

Figure 3.30: The Root Locus Design for the Longitudinal Velocity Control System

The matrices used in the design are augmented with the integrator states and are shown in Equations 3.39 and 3.40.

$$\mathbf{A}_u = \begin{bmatrix} A_\theta & B_\theta \\ \underline{0} & 0 \end{bmatrix} \tag{3.39}$$

$$\mathbf{B}_u = \begin{bmatrix} B_\theta \\ {}^{K_I}/_{K_p} \end{bmatrix} \tag{3.40}$$

The final closed loop system can then be represented as shown in Equation 3.41.

$$\dot{\mathbf{x}} = \left(\mathbf{A}_u + \mathbf{B}_u \begin{bmatrix} -K_p & \underline{0} \end{bmatrix}\right)\mathbf{x} + K_p\mathbf{B}_u u_r \tag{3.41}$$

The longitudinal system was found to have a longer settling time than the lateral system - likely due to the increased inertia. The longitudinal control responses are illustrated in Figure 3.31. As can be seen, the system shows a fast rise time, mild overshoot and asymptotic tracking. In the design, a faster rise time was favoured over a fast settling time to maximise the performance of the helicopter.

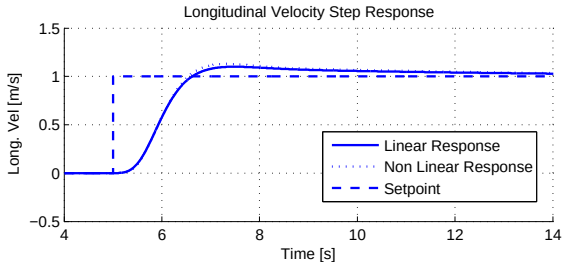

(a) Closed Loop Step Response

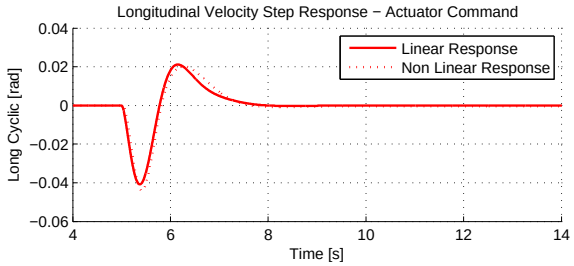

(b) Closed Loop Step Response - Actuator Command

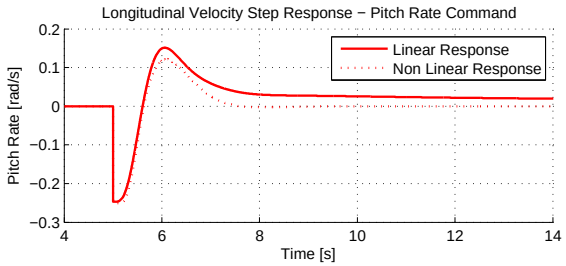

(c) Closed Loop Step Response - Pitch Rate Command

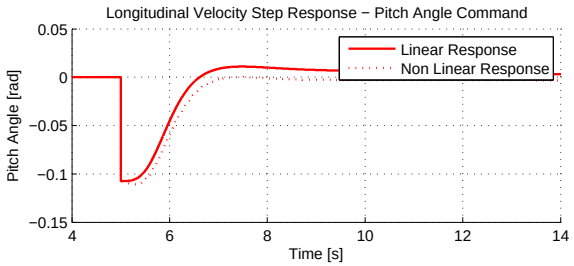

(d) Closed Loop Step Response - Pitch Angle Command

Figure 3.31: Longitudinal Velocity Step Responses

3.6.4 Longitudinal Position Controller

The longitudinal position controller is implemented using a proportional controller. The integrator in the velocity controller, as well as the implicit integration between the states, ensures absolute tracking in the face of low frequency disturbances, allowing effective position tracking to be implemented using a simple proportional feedback law. The controller is illustrated in Figure 3.32.

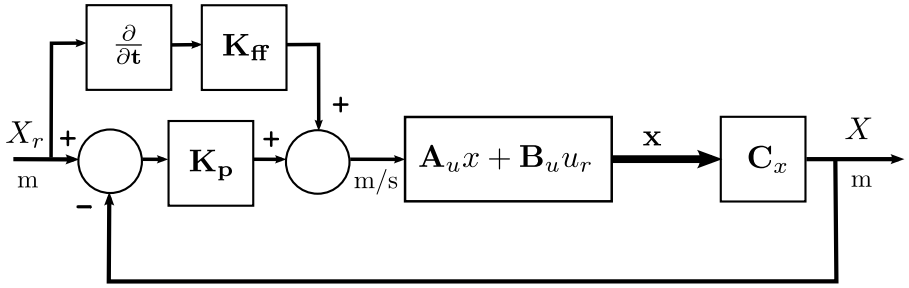

Figure 3.32: The Longitudinal Position Control Structure

The controller was found to operate well with a gain of $K_p = 0.45$, and was designed according to the root locus and response shown in Figure 3.33. The longitudinal controller, despite a larger inertia, is able to match the lateral position controller in performance, asymptotically approximating a position in around 5 seconds. Once again, moderate control gains were chosen to make it robust to GPS drift and delays. With better estimates on position, larger, more aggressive gains can be implemented.

The velocity feed-forward illustrated in Figure 3.32 is implemented to enable tracking of a moving reference (that matches a type 2 profile - moving at constant speed). For generality, the link is illustrated as a derivative and a gain, directly linked to the reference - in practice, the feed-forward link should have unity gain and the derivative would typically be replaced with a measurement of the reference velocity.

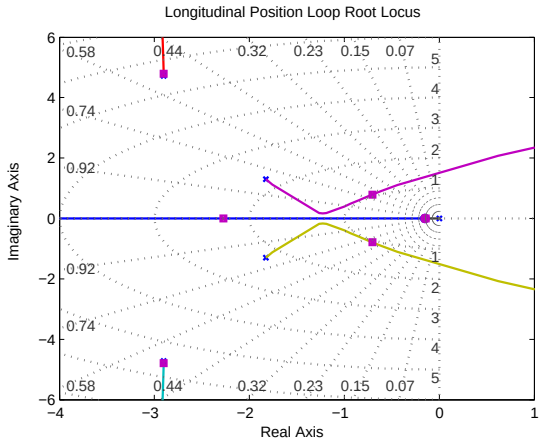

(a) Longitudinal Position Root Locus

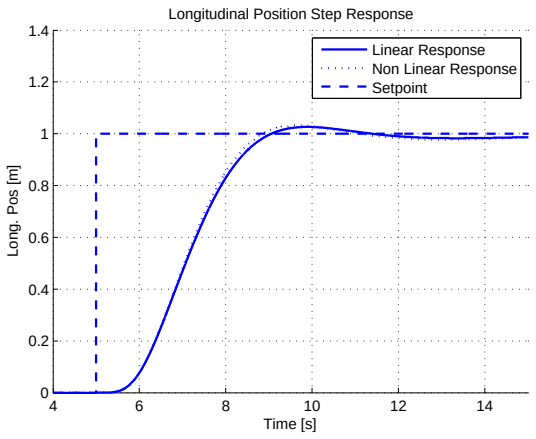

(b) Longitudinal Position Step Response

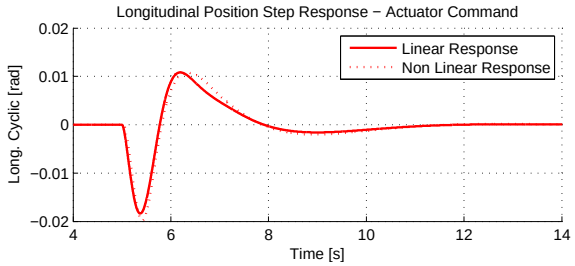

(c) Longitudinal Position Step Response - Actuator Command

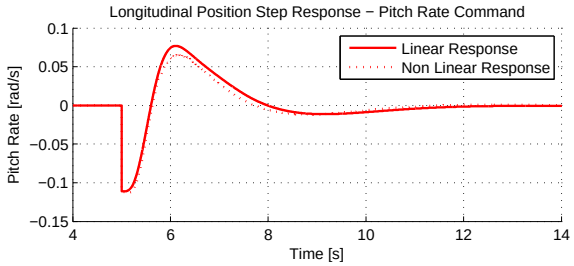

(d) Longitudinal Position Step Response - Roll Rate Command

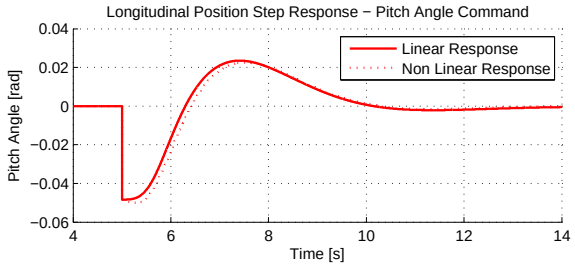

(e) Longitudinal Position Step Response - Roll Angle Command

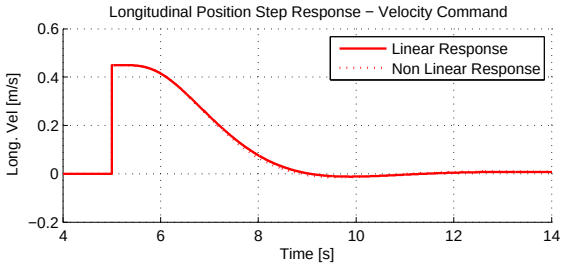

(f) Longitudinal Position Step Response - Velocity Command

Figure 3.33: Longitudinal Position Control Design

3.7 Velocity Feed-Forward Design

In order to ensure good asymptotic tracking of a position reference moving at a constant velocity (a type 2 reference), a reference velocity feed-forward is critical in minimizing the steady-state separation distance. The velocity feed-forward design, as illustrated in the position controllers (Figure 3.32 and 3.16), feeds the velocity of the reference signal into the system as a means of counteracting the steady state offset that would otherwise occur. The rate at which updates are received is important, as for practical implementation the reference velocity will be transmitted wirelessly to the helicopter and the required update rate defines the required capabilities of the data link.

To define the required minimum reference velocity update rate, in so doing defining the system's tracking capability with regard to moving reference signals, a low pass filter was added to the feed forward system to help ascertain the practical bandwidth of the non-linear system used to describe the helicopter. When given a temporarily moving reference (an almost trapezoidal position reference), the filter bandwidth could be altered to establish at which point the filter is below the bandwidth of the system (seen when the response profile

deviates from the higher bandwidth response) and so determine the practical update rate required that would not limit the tracking response of the helicopter. The effect of various filters is illustrated in Figure 3.34.

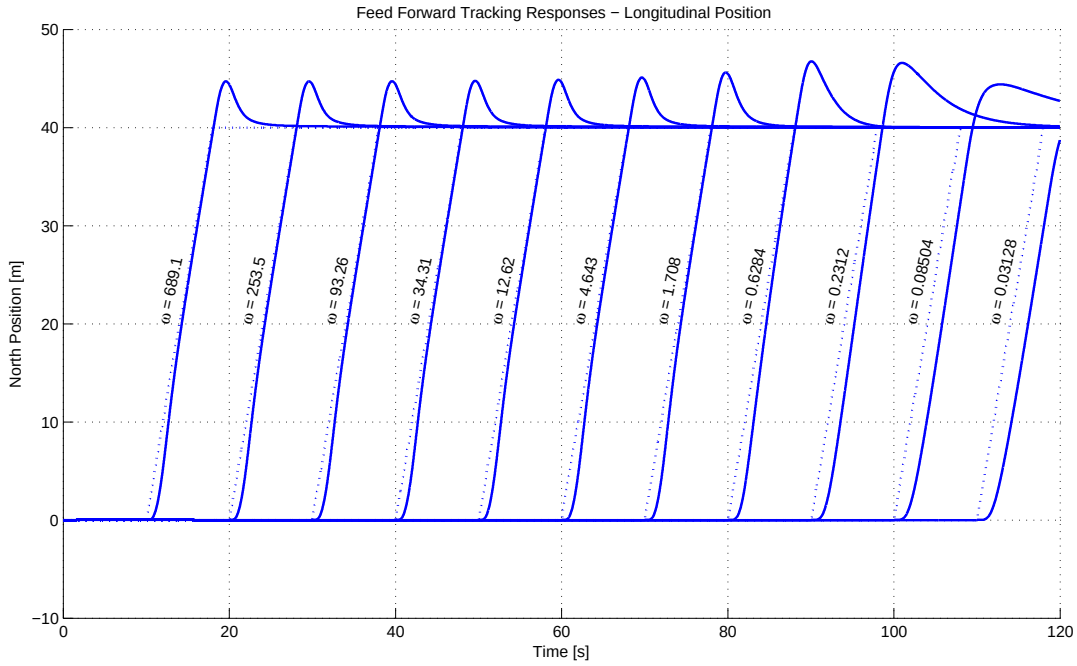

Figure 3.34: Tracking Response when tracking a velocity of 5 m/s

As can be seen, the system begins to deviate at a filter bandwidth of 4.643 rad/s (0.7 Hz), implying that the bandwidth at the velocity feedforward input is similarly positioned. It can thus be extrapolated that higher frequency contents will be damped out of the system, and velocity updates above 2Hz should be sufficient in providing information that ensures the optimum performance of the feedforward system.

This design outcome became particularly useful when implemented with the Novatel Align[1] functionality where a relative velocity measurement was not directly available, and was instead obtained via a separate telemetry link. This is discussed further in Chapter 5.

3.8 Wind Gust Attenuation

Performance in the presence of wind based disturbances such as gusts, thermals or turbulence is a critical quality in the evaluation of the control system's performance. While many characteristic noise models are used to generate wind disturbances (such as the Dryden or von Kármán models for aeroplanes), many of these models are not directly appropriate for a helicopter due to the implied directionality. To establish the system's susceptibility to wind gusts, the wind inputs were instead perturbed using a low pass filtered band limited white noise. This noise was then multiplied up in frequency to determine frequency bands that the helicopter is particularly susceptible to.

The multiplier approach, analogous to that used in the heterodyning of radio signals, ensures that both noise

[1]Novatel Align is a function of the Novatel DGPS in which an accurate position difference can be obtained from a moving base-rover setup.

power and bandwidth are preserved for a given test band in the frequency spectrum, allowing different bands to be analysed in the system for the same input energy. An illustration of the system is shown in Figure 3.35.

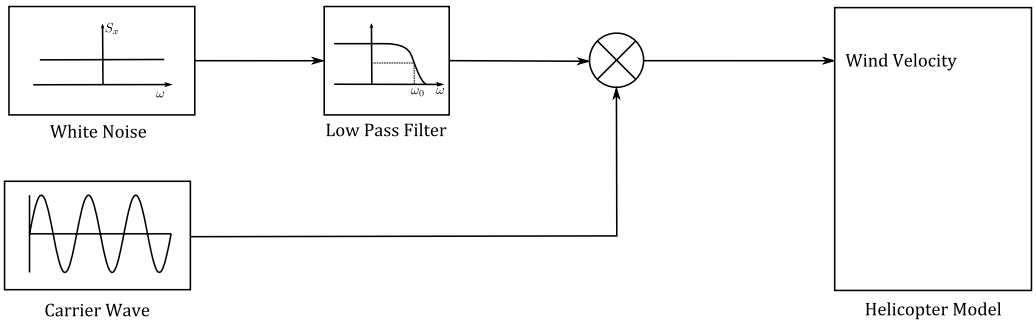

Figure 3.35: Wind Sensitivity Analysis

The system does favour specific frequencies at low carrier wave frequencies due to the overlapping of spectral envelopes. This effect is illustrated in Figure 3.36, and care should be taken for responses generated for frequency intervals lower than the bandwidth of the white noise.

With regard to isolating specific frequencies of interest, low noise power values were used in order to test the controllers without aggravating significant non-linearities inherent in the model. This approach has a number of advantages in that it ensures a realistic approximation of relevant frequency bands of interest that show susceptibility to wind noise, while avoiding statistical dependence on amplitude. In addition to this, it has the advantage of providing an indication of the helicopter's wind rejection performance in the presence of frequency based wind gusts.

In order to analyse the wind rejection qualities of the system, it is necessary to generate system responses based on the standard deviation of the output. The performance measure is the logarithmic ratio of the standard deviation of the system velocity response to the standard deviation of the generated wind velocity, termed the Disturbance Sensitivity Ration (DSR) and defined as follows,

$$DSR = 20 \log_{10} \frac{\sigma_{vel}}{\sigma_{wind}} \tag{3.42}$$

Figure 3.37 was generated for the control gains discussed in this section. The control system shows remarkable stability in the presences of wind gusts, showing only minor deviations before inertia attenuates the system responses. Generally speaking, performance is best in the longitudinal axes and worst in the heave axes, implying that best performance in windy conditions would be obtained by pointing the nose into the wind.

Significant drops in amplitude are seen after 10 rad/s, implying that the helicopter will show fairly good performance in high-frequency turbulence. However, the modelling approach does not specifically account for

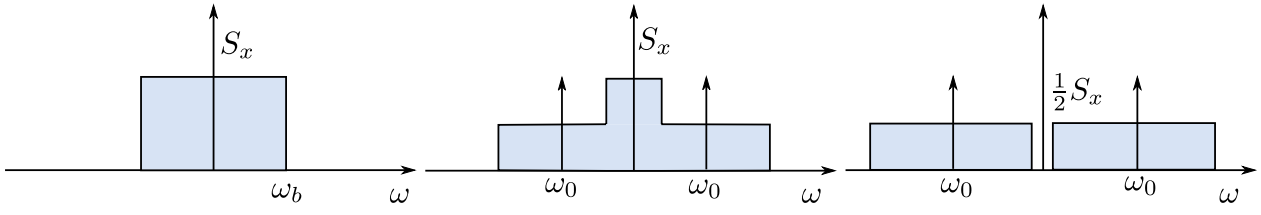

(a) $\omega_0 = 0$ **(b)** $\omega_0 < \omega_b$ **(c)** $\omega_0 > \omega_b$

Figure 3.36: Anomalies caused by Spectral Overlap

turbulent wind conditions and such extrapolations should be the subject of further study.

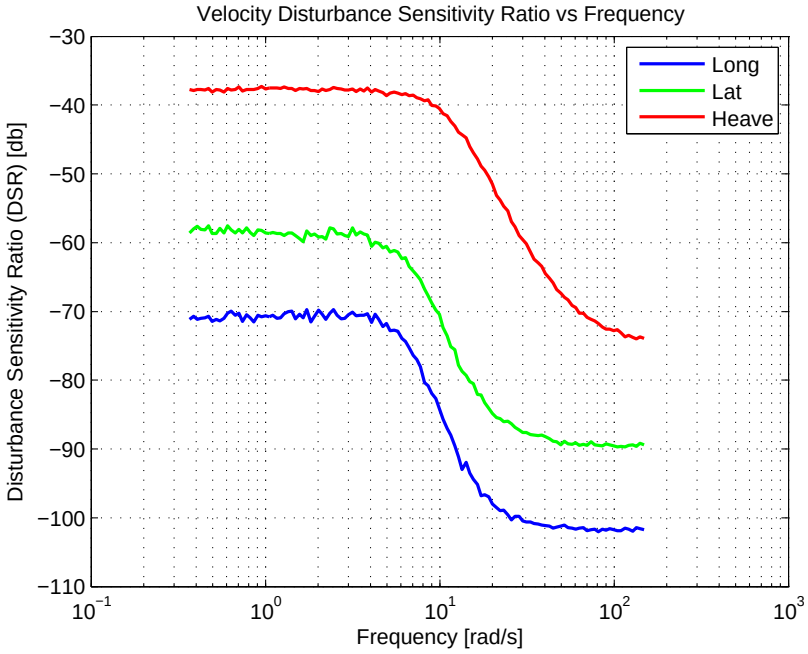

Figure 3.37: Wind Velocity Disturbance Sensitivity

3.9 Discretization of Control Laws

The OBC structure described in Chapter 5 allows the propagation of control laws at 50Hz, while measurement updates are provided at a similar frequency. In this design the fastest poles in the system exist well below 30 rad/sec (~5Hz), allowing accurate implementation in a digital control system by direct digital conversion. Integrators are implemented using discrete time-step integration, and filters through their direct ZOH equivalent values.

Chapter 4

Autonomous Behaviour

The autonomous behaviour of the helicopter is defined by high-level control functionality and state machines designed to ensure stability, ease of testing and abstracted functionality. This section is broken down into a description of the general state machine design, the state flow description before delving into individual system functionality.

4.1 State Machine

The helicopter's control system is directed by a state-machine that ensures functional system behaviour and simplifies testing procedures. The states (or modes) in the system are described in the table below,

No.	State	Description
0	Error State	The helicopter is completely disarmed (including servo motors)
1	Disarmed	The RC pilot has complete control.
2-5	Piloted References	In these modes the RC pilot references are sent to the relevant controller inputs. These references were not used in the actual flight testing in the end.
6	Controller Test States	Allows for full control testing. This mode allows the Groundstation operator to dynamically enable and test control loops using step commands.
7	Hold State	This completely enables the control system, and sets it to maintain its current position. Also functions as an emergency stop.
8	Home State	The helicopter will return to its original starting position.
9	Pseudo Deck Tracking	The helicopter will track a moving reference with additional altitude
10	Pseudo Deck Landing	Here a landing will be attempted on a moving/non-moving reference but will 'complete' the landing several meters above the target.
11	Deck Tracking	The helicopter will track a moving reference
12	Deck Landing	A landing will be attempted on the moving/non-moving target.
13	Waypoint Navigation	The helicopter will track waypoint references/commands.
14	Landed State	The helicopter is landed and will disable relevant controllers.

Table 4.1: States in the State Machine

4.2 State Flow Diagram

The state flow diagram describes how state transitions occur. In the diagram below, dashed lines represent actions by the RC pilot, whilst solid lines indicate transitions from the ground station.

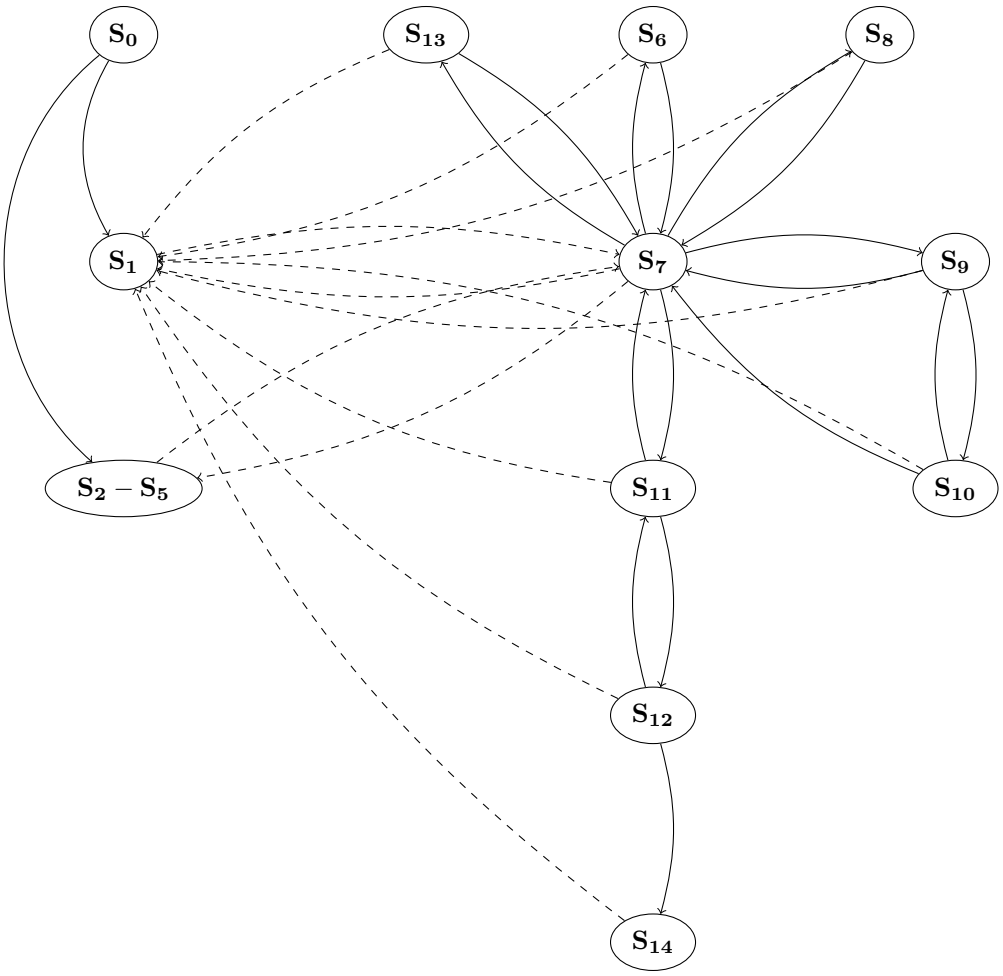

Figure 4.1: State Flow Diagram

The primary philosophy in the design of the state machine is safety. With this in mind, the RC pilot has absolute authority on the states - if the pilot disengages the autopilot at any time, control is automatically and immediately returned. At take off, the pilot begins with control authority and can fly the helicopter to a desired altitude. On engaging the autopilot, the helicopter automatically enters a hold mode.

The hold mode is the centre point of the state machine. In this state, the helicopter will maintain it's current reference, and it is from here that the other modes can be activated. The ground station controller is able to active the other modes of the helicopter - waypoint tracking, control loop testing (step tests etc.), pseudo landing and tracking operations and actual landing and tracking operations. The final state (the landed state) occurs once a touch down has occurred. In this case, elements of the controller are deactivated, and authority returned to the pilot should it be requested.

4.3 Waypoint Tracking

In this mode, the helicopter is able to track a series of given waypoints. In addition to dynamic waypoint tracking, the waypoint tracking algorithm is bounded by the following settings,

1. **Proceed** : This sets whether the helicopter will automatically proceed to the next waypoint when tracking.
2. **Wrap Around** : This sets whether the helicopter will revert to the first waypoint on tracking the last one.
3. **Hold Heading** : This is intended primarily for testing, and forces the controller to maintain its current heading reference - relying instead on the lateral and longitudinal position controllers to track the waypoints.

The control system design used in this work does not favour tracking waypoint manoeuvres at speed (at speed helicopters mimic aircraft in terms of bank-to-turn behaviour, and the control system is set up to use the tail rotor as the principal actuator in heading command tracking). As such, it is necessary to reduce velocity before a heading change command is given.

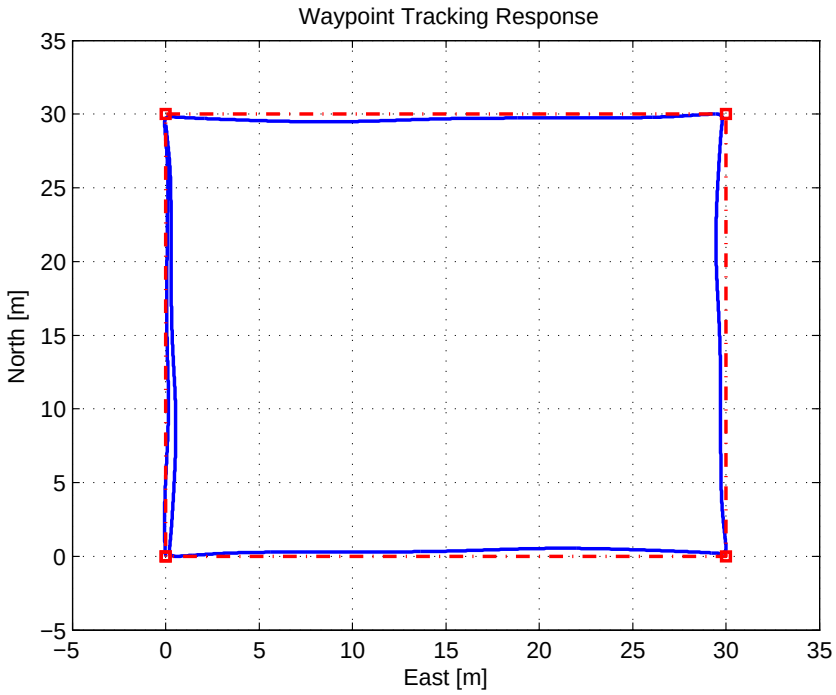

Figure 4.2: Waypoint Tracking Simulation Results

In order to implement waypoint tracking in this case, a simplified cross-track model was used. Upon reaching a waypoint, the helicopter is pointed in the direction of the next waypoint (if heading hold is not enabled), and the next coordinate is passed to the position references of the control system when the heading error is less than 15°. The cross track behaviour of the helicopter is ensured for small deviations through the behaviour of the lateral positioning system. Tracking results are shown in Figure 4.2.

The slight deviation in position when transitioning between waypoints is due to the helicopter performing the last portion of the heading change command when the references are passed. The response is predictable and will occur between waypoints if a change in heading command is issued in order to transition to a waypoint.

4.4 Hold Mode

The hold mode is the functional centrepiece of the autonomous behaviour and acts to ensure the stability and integrity of the system in between active modes. If a hold command is given, position is locked to it's current position if velocity is below 1m/s, else velocity is driven to zero, at which point position hold is engaged.

This system ensures safety in the case of the command being issued whilst the helicopter is in forward flight. Results for the issuance of an 'emergency hold' command (at T=15 s) are shown in Figure 4.3,

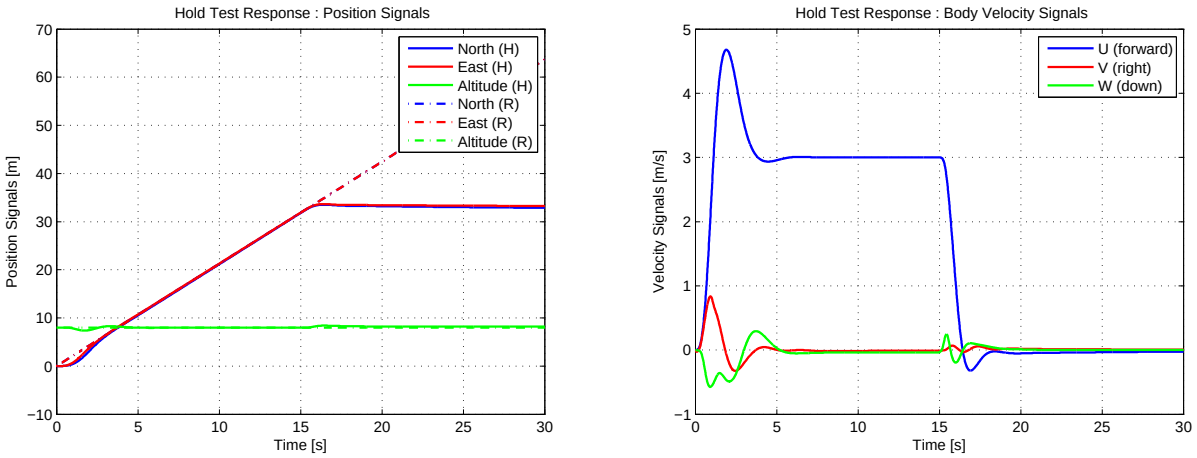

(a) Position References for Hold Command **(b)** Helicopter Velocity Signals for Hold Command

Figure 4.3: Hold Mode Functionality - 'Emergency Stop' Results

As can be seen in the figure, the issuance of a hold command causes an immediate cessation in the helicopter's motion, bringing the helicopter to an abrupt halt. In Figure 4.3a, the dashed lines refer to the position reference, whilst the solid lines refer to the helicopter's position values.

4.5 Deck Tracking Modes

In order to land on a moving deck, it is necessary to track the deck itself with no steady state error. This is achieved via the position control commands coupled with the base velocity commands fed forward as an additional reference into the velocity controllers.

The helicopter's control system is intended for implementation at hover, and is generally unsuited to high-speed manoeuvring (lacking bank-to-turn style functionality). However, long range tracking of a moving target (with a potentially changing reference heading) can be accomplished through the implementation of a two-state tracking state machine, each commanding a different style of control.

The first style of control deals with a distant reference point (the landing target on the ship) - the standard method of control (i.e. commanding a longitudinal and a lateral position loops to a particular coordinate) is subject to lateral oscillation when far from the target (assuming the helicopter is aligned with the ship), as a small change in the heading angle of the helicopter causes large changes in the lateral position error. When the object is distant enough this causes oscillations in the system due to the small angle changes.

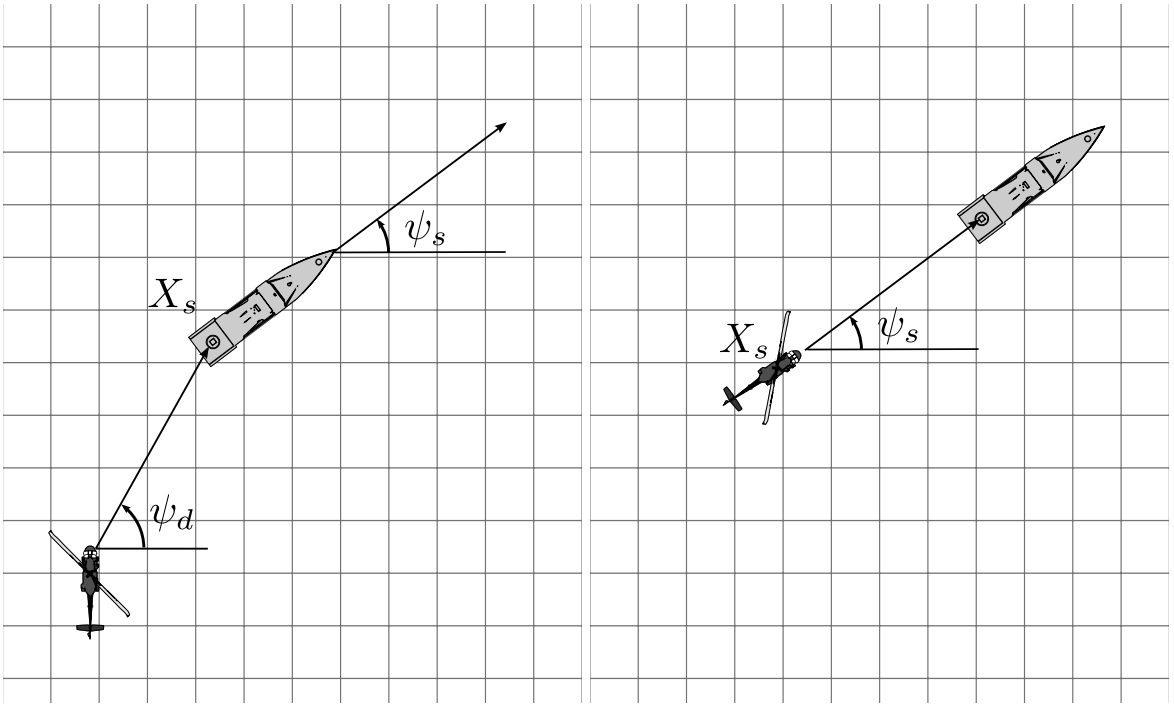

(a) Stage 1 : Tracking the Deck using Heading and Longitudinal Position Errors (Lateral Position Controller Disabled)

(b) Stage 2 :Tracking the Deck's Position using Long. and Lat. Position Feedback (Heading Reference Set to Heading of Ship)

Figure 4.4: Deck Tracking Procedure

The reason for this is due to the conversion of a North-East coordinate to a body axis (X-Y) coordinate. When considering a position error, the error calculation would typically take the form shown in Equation 4.1.

$$\begin{bmatrix} Err_X \\ Err_Y \end{bmatrix} = \begin{bmatrix} \cos\psi & \sin\psi \\ -\sin\psi & \cos\psi \end{bmatrix} \begin{bmatrix} N - N_{ref} \\ E - E_{ref} \end{bmatrix} \tag{4.1}$$

Reconstructing the coordinate frame to be relative to the current heading (presumed to be pointing directly at the target, with only a large longitudinal offset, $|Err|$), the matrix shown in Equation 4.2 is obtained. For the purpose of this explanation, the angle conversions have been simplified using the small angle considerations.

$$\begin{bmatrix} \Delta Err_X \\ \Delta Err_Y \end{bmatrix} = \begin{bmatrix} 1 & \Delta\psi \\ -\Delta\psi & 1 \end{bmatrix} \begin{bmatrix} |Err| \\ 0 \end{bmatrix} \tag{4.2}$$

As can be seen, a small change in the heading angle when aligned with the target reference can infer a large position error which the control system will attempt to minimize. When combined with small fluctuations in the heading angle (caused either by disturbances, noise or simply predictable transients), this leads to oscillation or instability.

To counteract this, the helicopter is simply controlled with reference to the absolute heading and magnitude of the position error, using only the longitudinal position controller and the heading controller (the lateral position controller is disabled). When the absolute position error has dropped to below a specified limit (in this case, a limit of 15m was chosen), the helicopter is commanded to instead use both position errors, and aligns itself with the heading of the reference. This procedure is illustrated in Figure 4.4.

The procedure ensures the safety of the helicopter in light of it's controller implementation. For small changes in heading when the controller mode is changed (smaller than 10°), the reference transition is immediate.

Should a large change in heading angle be required, the helicopter is first slowed down before attempting to approximate the deck. This ensures that major transients are avoided when changing the mode without bank-to-turn functionality implemented on the helicopter.

Ship tracking was found to work well in theory, tracking the deck with no offset and with no overshoot. Typical responses are shown in Figure 4.5 for a standard tracking command. In the figure shown, the tracking system is initiated after 5 seconds.

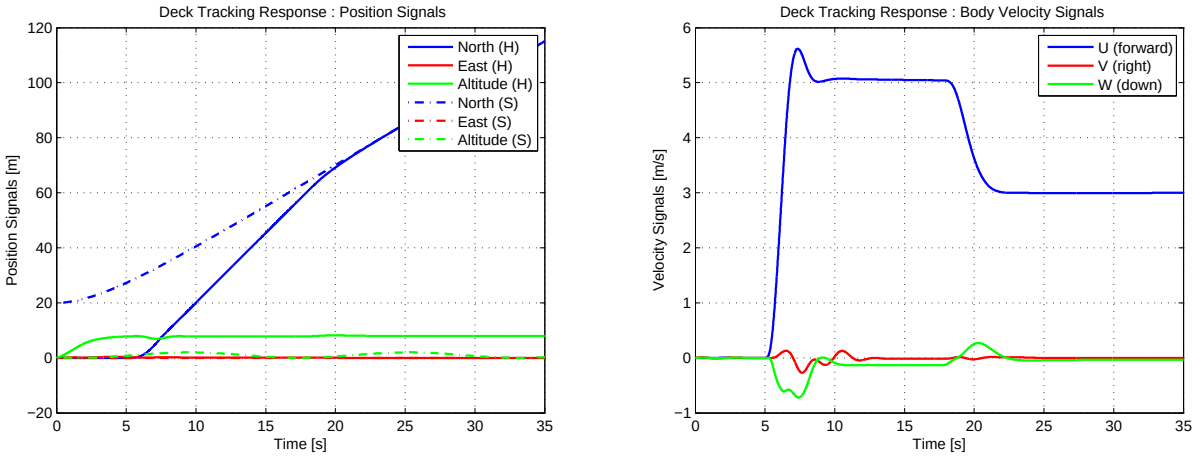

(a) Asymptotic Position Tracking

(b) Velocity Commands in Tracking

Figure 4.5: Deck Tracking System Response

4.6 Deck Landing Modes

The deck landing modes are only accessible from within the deck tracking modes. For the purpose of practical testing, two landing modes were implemented: a pseudo-landing mode, wherein a landing is attempted a fixed distance above the deck (allowing algorithmic testing before an actual landing is attempted), and an actual landing mode, where the helicopter is commanded to land on the moving ship deck.

In order for a landing to be attempted, the helicopter must be located within 1.5m of the deck's North-East position, and a landing command must be given should landing conditions be within operational bounds. This command can either be given by an operator, or by an autonomous system (the implementation and applicability of such a system is discussed in Chapter 7).

The system is designed to revert to the tracking state should it diverge from the 1.5m radius of the deck's centre position (illustrated in Figure 4.6). If the ship is moving faster than 1m/s at the time of landing, the helicopter's heading is set to match that of the ship's. Should the ship be moving slower than 1 m/s, the heading command is free to point into the wind. The controller used to implement the safe landing is an augmented version of the standard altitude controller, illustrated in Figure 4.7. The controller design accounts for both static and moving landings.

Essentially this controller design is intended to minimize landing times for ship deck landings, as quiescent periods are not necessarily quiescent for long and as little time as possible should be wasted. The controller design is the standard altitude controller with several modifications to ensure a repeatable and firm impact velocity. The modifications are detailed as follows, with reference to the diagram in Figure 4.7.

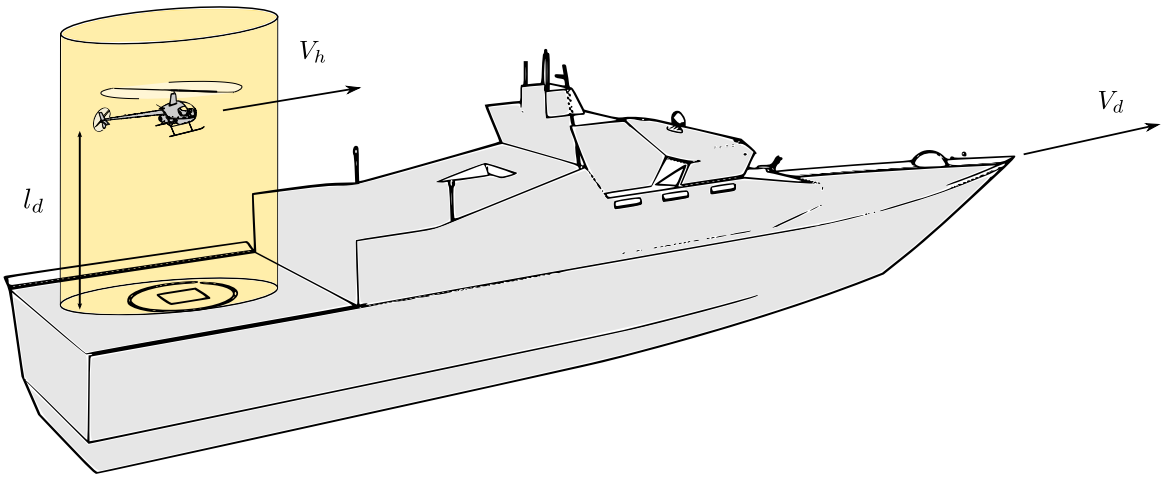

Figure 4.6: Illustration of the Deck Landing Procedure

1. **Offset Velocity (w_0) :** The offset velocity is analogous to the intended impact velocity. This ensures that the helicopter has a solid impact with the deck.

2. **Deck Heave Velocity Feed Forward (w_c) :** Intended to reduce relative velocities in the event of a potentially large heave rate, the deck's heave velocity is added to the controller to allow the helicopter to match, in part, the heave velocity of the deck. This ensures that, upon impact, the offset velocity is the intended impact velocity. The function $f(h)$ was include to allow the offset velocity to be phased in - i.e. that the helicopter only matches the velocity of the deck when close to the deck, and not necessarily the instant that landing is enabled. This helps to ensure a linear response and removes unnecessary reference tracking when high above the deck.

3. **Increase Saturation and Relaxed Gain for Altitude Control:** Landing presents a variety of hazards, and the proportional controller is limited to reduce the speed of response for initial practical testing. The velocity command emanating from the proportional altitude controller is further limited to ensure that large velocity commands are not given and the proportional gain is reduced to slow the dynamic response of the helicopter. These could potentially be modified to improve the performance of the landing times, but may also affect the stresses on the aircraft while landing.

In the standard landing mode, once a successful landing has occurred, the helicopter autonomously reverts to a landed state. In this state, the controller is completely disabled, barring yaw rate damping, and a reduced collective signal to ensure deck traction. Yaw rate damping is enabled on landing to ensure that the rudder collective angle does not induce unnecessary dynamics. The transition takes place based on the detection of an acceleration spike when within range of the deck.

In the pseudo-landing mode, the deck reference has an additional altitude offset, and when this is passed the controller maintains the altitude reference instead of transitioning to the landed state. From here, the RC pilot is able to take over to safely land the helicopter.

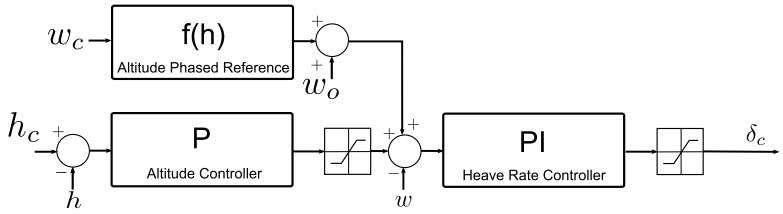

Figure 4.7: Augmented Landing Controller

Simulations show that impact velocity is typically around the offset velocity. The results of a pseudo landing (a landing at a fixed offset above the deck) are shown in Figure 4.8. A 2m sinusoid reference is used for ease of illustration, the landing was initiated with a desired impact velocity of 0.5m/s, and an offset of 2.5m. Note that the offset velocity in the controller causes the reference tracking to occur slightly below the reference. The vertical line on the figures shown indicate the instant at which a theoretical touchdown would occur in an actual landing simulation.

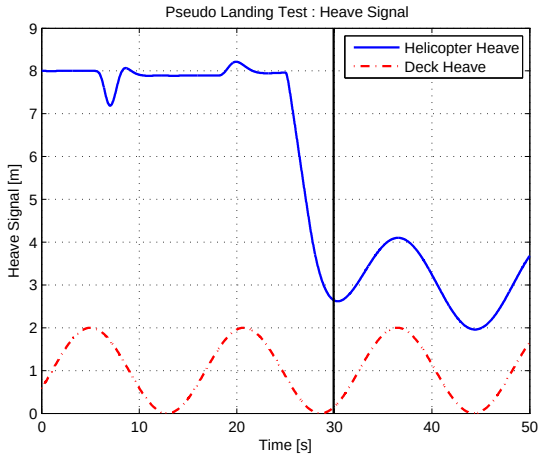

(a) Position Tracking (Altitude)

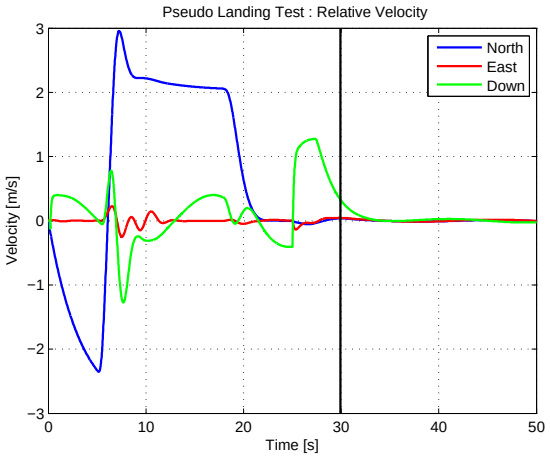

(b) Relative Velocity

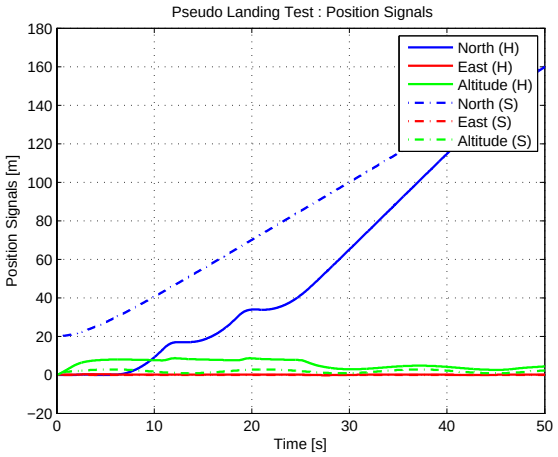

(c) Position Tracking

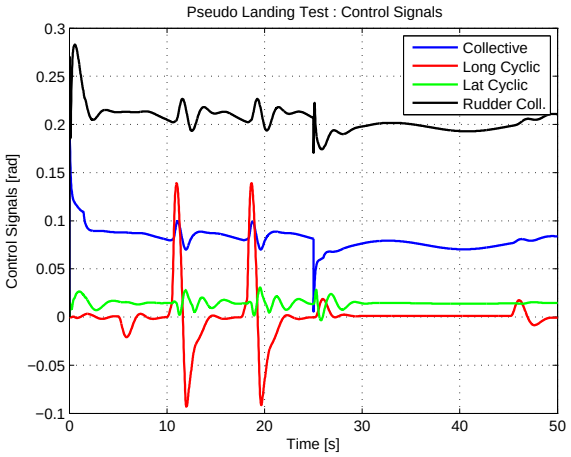

(d) Control Signals

Figure 4.8: Pseudo Landing System Response

Chapter 5

Hardware, Hardware-in-the-Loop Testing and System Design

Hardware-in-the-Loop (HIL) testing is the testing of all hardware, avionics and algorithms on a real-time computer simulated model. This ensures the proper functioning of hardware and systems before flights. In this chapter, the structure, interaction and operation of the hardware and software systems, as well as descriptions of estimator and sensor capabilities are discussed.

5.1 Structural Overview

The overall operation of the helicopter is governed by both the ground station controller and the safety pilot. The safety pilot's responsibility is to ensure the safety of the helicopter in the case of system failure, while the ground station controller has the authority to activate high level functionality of the control system. The safety pilot has absolute authority over the procedure and can assume control of the helicopter instantly via a switch on the RC remote. The structural overview of the system is illustrated in Figure 5.1.

The servomotors used to actuate the helicopter are controlled via a separate servomotor control board. In order to ensure the safety of the helicopter in the event that the commands from the On-Board Computer (OBC) fail, absolute control authority is enforced via the servomotor control board. In this manner, the pilot maintains authority over the helicopter until such time as both the ground station controller and the safety pilot authorize the autopilot. Should the on-board computer (OBC) fail, control is automatically returned to the safety pilot.

The on-board computer is used to estimate system states based on the sensor readings, and executes the control and estimation algorithms when enabled. It also provides high-level functionality including the deck homing, waypoint navigation and autonomous landing algorithms. These commands are communicated to the On-Board Computer via an RF link connected to the ground station software.

Hardware-in-the-Loop (HIL) functionality is implemented via a separate HIL board that replaces the sensed values with simulated values in order to verify the integrity of the system. In this mode, the values sent to the servo board from the on-board-computer are sent back to the emulation computer and run through an

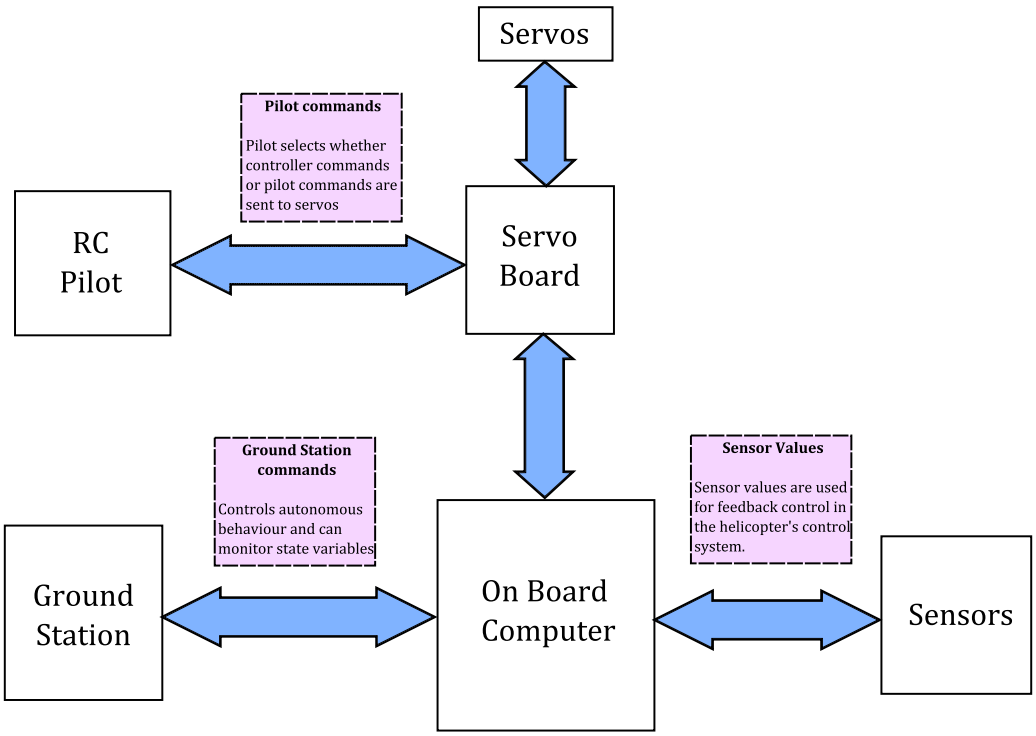

Figure 5.1: Overview of the Helicopter Avionics Structure

emulated helicopter environment in order to calculate theoretical state values. These values are then converted to theoretical sensor measurements and sent back to the on-board computer. The real-time toolbox is used in MATLAB to maintain real-time accuracy.

5.2 Hardware Setup

The hardware structure for the system is based on a general hardware structure used at the Electronics Systems Laboratory, an overview of which is illustrated in Figure 5.2.

The on-board computer (OBC) is a custom designed Printed Circuit Board (PCB) based on two dsPIC32f microcontrollers (produced by Microchip), as well as a series of auxiliary components to allow external communication and circuit protection. The microcontrollers feature on board CAN bus controllers that are used to provide communication between the integrated modules. One of the microcontrollers is used exclusively for GPS message parsing whilst the other processor is featured as a general purpose chip (this is utilized to run the estimation, control and data transmission algorithms). The OBC stack allows additional modules to be directly connected via the CAN bus, which include the IMU board, the magnetometer and the servoboard. The RF link is implemented via a paired 9600 bps Maxstream 24XStream module produced by Digi International, capable of maintaining a 10 mile line of sight link.

The sensor boards for the IMU and the Magnetometer also used the dsPIC microcontrollers to facilitate CAN bus communication and Analog to Digital value conversion. The magnetometer used on the X-Cell Aerobatic Helicopter is the HMC2003 produced by Honeywell, while inertial measurement information is obtained using the ADIS16355 IMU from Analog Devices (an embedded unit containing 3 axis accelerometers and gyroscopes). The GPS used in this setup is the Novatel OEMV-1G single frequency receiver operated with the ProPak V3 to provide differential position estimation capabilities. Communication to the unit on board the helicopter is

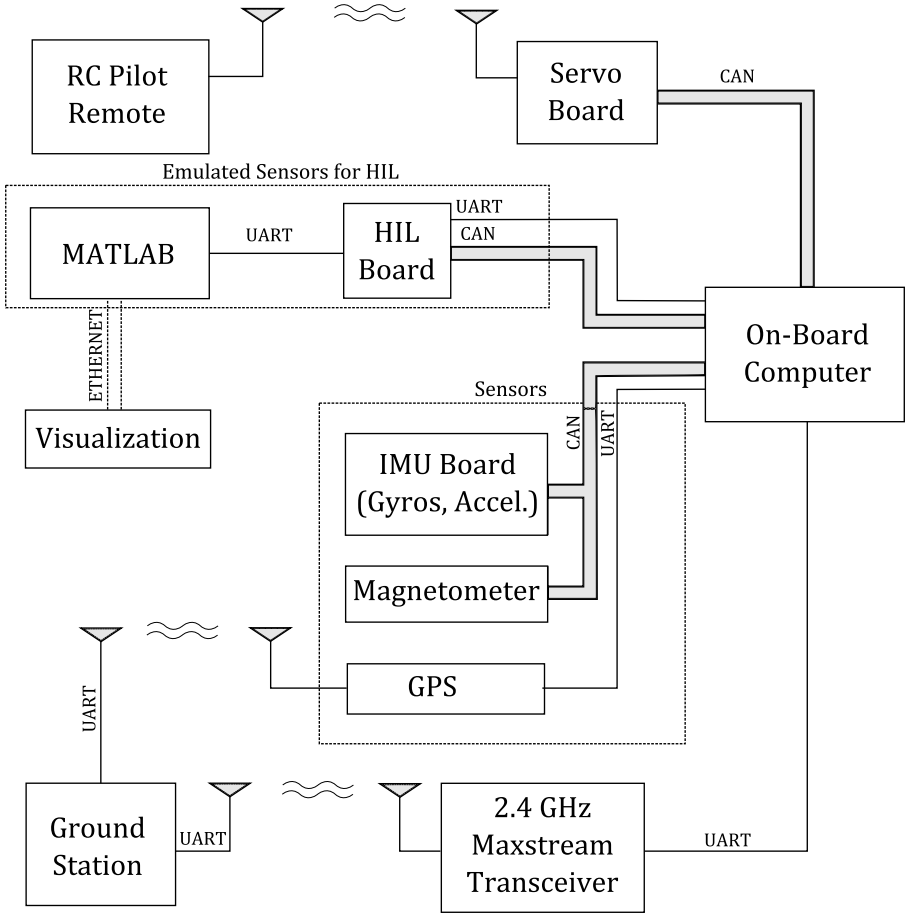

Figure 5.2: Hardware System Structure Overview

implemented using UART.

In order to make use of the Novatel ALIGN functionality, an additional high-bandwidth communication link is required between the helicopter and ground based GPS units. This was implemented in the form of a WiFly RN134 roving wireless network, running at 230400 BPS.

Hardware-in-the-Loop functionality is introduced via connection (using both CAN and UART) to a HIL board. The HIL board contains another dsPIC microcontroller that communicates information between the simulation computer and the OBC by converting between the necessary protocols. Specifically, the HIL board is required to maintain a high speed serial link for communicating servo values to, and sensor information from the simulation computer. Simultaneously, it is required to retrieve servomotor values from the CAN bus while relaying sensor information on to the CAN bus. GPS packet emulation is implemented on the HIL board, directly transcribing sensor information into the relevant GPS packets via a separate UART link. This system allows for high fidelity simulation of hardware using a software based model. The switch between the two sensor value sources is made using an embedded software command.

In order for the helicopter to obtain estimates of the base velocity [1], the logs are requested on the base station, and transferred to the helicopter via the RF link (typically at a rate of 2Hz, although higher rates can be implemented if necessary). In the HIL environment, this was implemented through an s-function that emulates the GPS base station that the software ground station connects to. This allowed for the base velocity estimates to be sent directly to the helicopter via the RF link in HIL simulation.

[1]The base velocity estimates are not directly available to the helicopter and must be obtained directly from the Base Station using the Ground Station software.

5.3 Embedded Software

State estimation is implemented via an Extended Kalman Filter (EKF) based on GPS, IMU and Magnetometer readings. The implementation used in the ESL allows for accelerometer based propagation of position estimates, as well as two different methods of calculating angle measurements (the TRIAD and Tilt/Heading update methods). This system is capable of providing position accuracy to within 0.1m in Differential mode (up to 1.5m in Single Point), and angle estimates to within 2 degrees. Different GPS modes are catered for in the system, including Single Point GPS, RTK (Real Time Kinematic) as well as the Novatel ALIGN GPS functionality.

Estimation and control algorithms are propagated at 50Hz. IMU and magnetometer measurements are received at 50 Hz through the CAN bus, while GPS measurement updates are received at 10 Hz. Autonomous capabilities are implemented in a state machine, with high level state transitions commanded by the ground station.

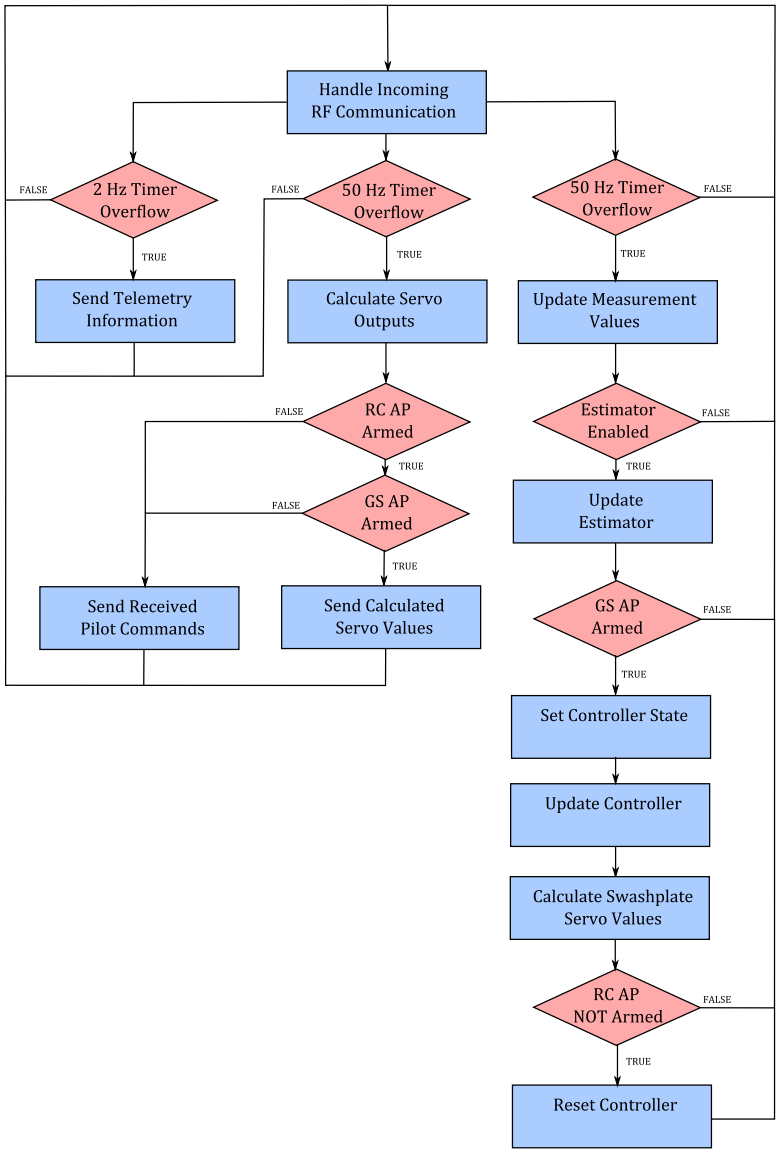

Figure 5.3: OBC Execution Flow Diagram

A typical system cycle is illustrated in Figure 5.3. Received commands are handled in every cycle of the OBC, ensuring that commands are interpreted as soon as they are received. A 50 Hz control cycle dominates the system, updating servo values based on the system mode and propagating controller and estimator systems if

they are enabled.

Measurement updates occur at 50 Hz, and the estimator is propagated if enabled. The controller requires that the estimator be enabled, and is itself propagated only if enabled by the Ground Station. The controller is reset until such time that the controller is fully enabled by the safety pilot. When reset, the controller commands are set to zero, the integrators are flushed and the outer setpoints are set to the relevant measurement values. This ensures that when fully enabled close to hover, the controller should be close to stable and to its independent command variables.

Servo commands are calculated in a 50 Hz control cycle, and the received pilot references are reflected until such time as both the ground station and the safety pilot enabled the autopilot. Telemetry data is sent at 2 Hz due to the scope of information and the limited capabilities of the RF link.

5.4 Ground Station

Ground Station capabilities are outlined here, and include several modifications to the standard Ground Station design. The Ground Station was adapted from that developed for the SLADe quad rotor UAV.

The ground station operates through a direct RF link to the helicopter. Due to the relatively low bandwidth link, telemetry values are limited to 2Hz, 1Hz and 0.5Hz updates, and include updates on controller and estimator states and variables, specific status information relating to servo outputs and battery information as well as operation times and general system information. Uplink commands are sent asynchronously as required.

An overview of the helicopter ground station capabilities is discussed in Table 5.1. An image of the Ground Station application is shown in Figure 5.4.

No.	Information Class	Description
0	General Status Information	Information relating to General System States (OBC Uptime, Battery Voltages, OBC states, etc.)
1	Controller Commands and Status Information	Commands can be given to test individual control loops, and controller references and saturations can be monitored for stability.
2	Autonomous Behaviour	Commands can be given that enable specific modes, including way-point tracking and autonomous landing behaviours. System states and behaviours are monitored, and limits and gains can be modified.
3	Estimator Initialization and Status Information	Estimator can be initialized for different configurations, and estimated variables are monitored.
4	Actuator Monitoring and Configuration	Display actuator settings and readings that can be used to test the calibration of remote controls and actuator trims.
5	GPS Setup	GPS can be initialized in a series of different modes depending on hardware used. Allows for setup to be initialized and monitored.
6	Swashplate Mixing Testing and Calibration	Allows the theoretical swashplate model to be calibrated and tested based on the theoretical actuator values.

Table 5.1: Information and Communication Capabilities of the Ground Station

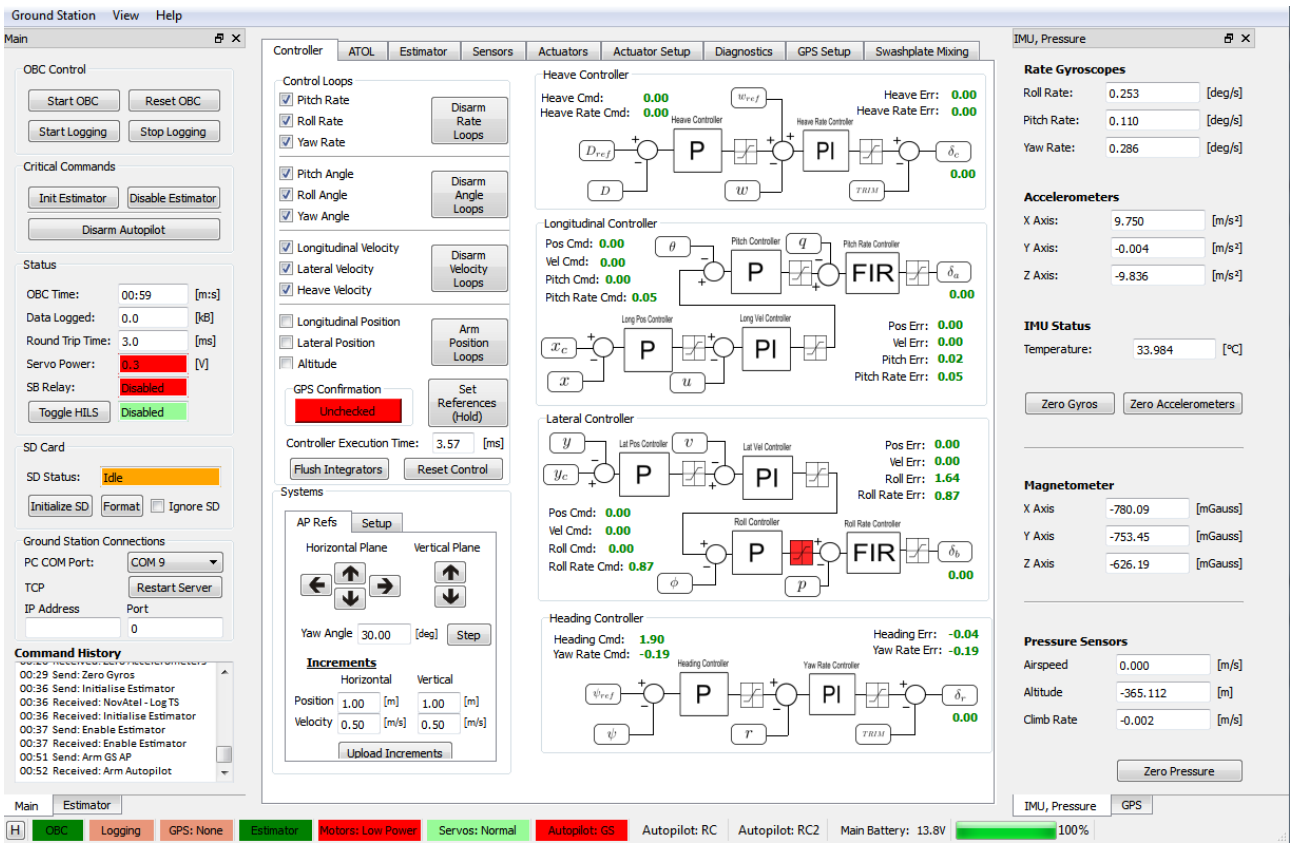

Figure 5.4: Ground Station User Display

5.5 Hardware-in-the-Loop Testing

Hardware-in-the-Loop (HIL) testing involves supplying the avionics with emulated sensor information and evaluating the hardware system's performance. Sensor noise and delays are generated based on estimates obtained from datasheets and empirical data.

The HIL environment makes use of several MATLAB s-functions that convert the simulated response values into the relevant measurement values, coupled with the associated drifts and noise levels. Simultaneously, the environment extracts the calculated servo values placed on the CAN bus (and transferred to the simulation via the HIL board), and uses these in the simulation to calculate the appropriate changes in the dynamics.

The hardware systems show congruency with the non-linear responses when simulated. The measurement values show accurate and timeous functioning of the on-board estimator, with estimation and control loops executing within 8ms. The full MATLAB-based HIL simulation was generally found to execute within 10ms, with occasional spikes of up to 50ms (worst case latency of around 2 to 3 control cycle executions, usually occurring during complicated manoeuvres with significant changes in dynamics).

On board logging was found to provide the most significant overhead, with occasional spikes of up to 100ms occurring - implying in a worst case a 5 control cycle execution loss. This is illustrated for a typical scenario in Figure 5.5. The cause of these spikes is assumed to be associated with the formatting of specific blocks when logging. Single Layer SD cards were found to improve the write performance, although occasional spikes were still found to occur. Telemetry processing was found to have a negligible execution time.

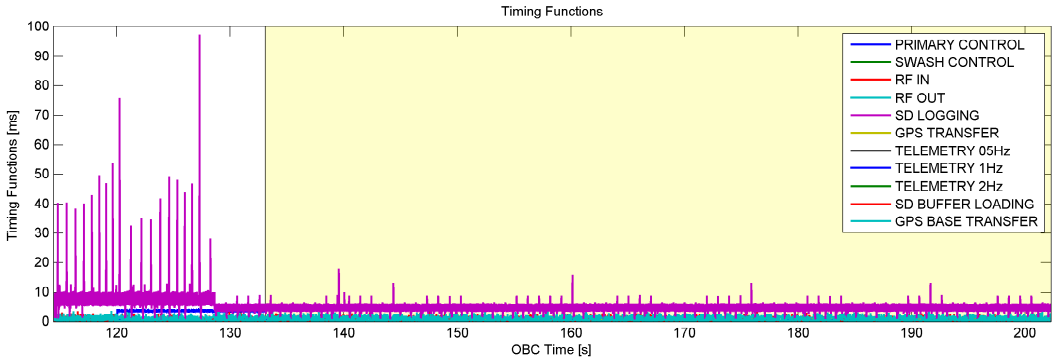

Figure 5.5: Typical Execution Times for OBC Tasks

GPS log processing is handled on the secondary dsPIC, and relayed to the primary dsPIC via the CAN Bus. This includes all GPS conversions as well as the Novatel ALIGN packet processing. As the communication between the separate GPS modules is facilitated via the WiFLY units, the availability of the ENU relative vector values were particularly sensitive to the separation distance between the units. When tested, the update rate was found to be around 4-5 Hz when close by (closer than 10m away) and occasionally less than 0.5 Hz (a 2 second interval) when fairly far away (at distances of around 30 to 40m). Practically, this limits the operation of the high fidelity position error measurements to use within 20m or so, requiring the system to make use of alternative measurements when further away. Random fluctuations in communication both far away and close by cause inconsistent performance.

The performance of the WiFLY link (measured as the frequency of updates on the OBC) is illustrated in Figures 5.6a and 5.6b. The update frequency is illustrated both as a one second and 10 second average (obtained by convolving the packet received signal with a square signal of T/T_s data points), illustrating the average frequency

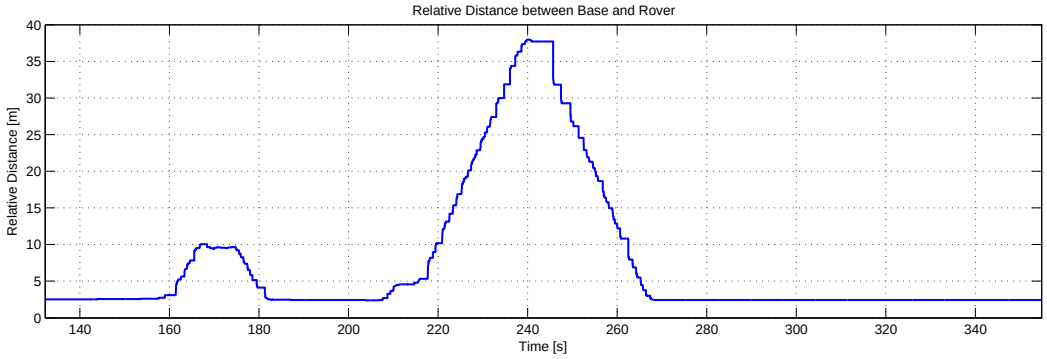

(a) Novatel ENU NE Error between Rover and Base

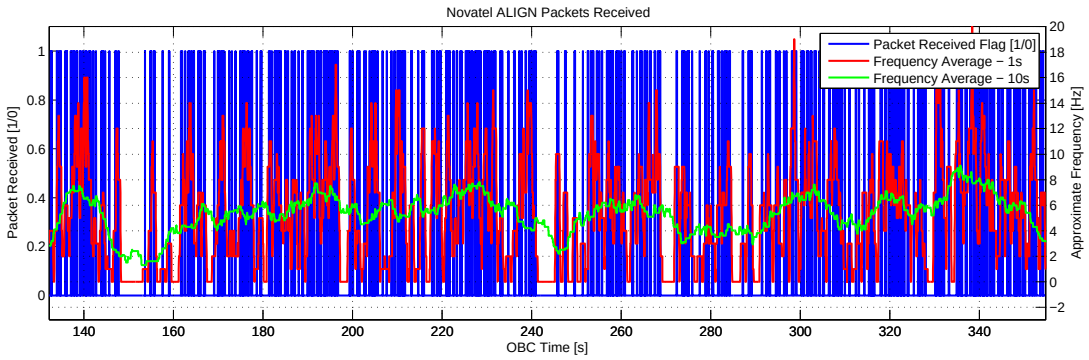

(b) Novatel ALIGN Update Rate Performance

Figure 5.6: Typical Novatel ALIGN Performance in Real World Scenario

of packets received within a time period. The interpreted performance shows significant fluctuation in both the number of packets received, as well as the time taken between sets of packets (at worst case, several seconds between received packets).

To counteract some of the deficiencies in the ALIGN communication, the received ENU value is propagated based on both the velocity of the platform and the velocity of the helicopter itself. The velocity of the platform is transmitted at 2Hz to the helicopter via the RF telemetry link, implying accurate propagation of the ENU vector in cases of slow ($\leq$ 1Hz) changes to the platform velocity.

An illustration of typical hardware controller system results is shown in Figure 5.7. The data shown illustrates select signals from a full Hardware-in-the-Loop simulation, during which a fully autonomous landing was initiated for landing on a stationary platform.

The results show five modes of the state machine - RC Flight, the Hold mode (entered into when the control system is engaged), the deck tracking and landing modes, and the landed state. During simulations, the RC flight time is implemented by substituting a software controller until such time as one of the autopilot signals is armed. This allowed for a rapid set up and initialization of the helicopter in simulation at any required altitude. In the system, once one of the autopilot signals are armed, the helicopter can be flown via the remote, whereas while both are armed the OBC has control. This is illustrated in Table 5.2.

GS_AP	RC_AP	Command
0	0	Software Autopilot (SIL)
0	1	RC Flight
1	0	RC Flight
1	1	Hardware Autopilot (HIL)

Table 5.2: System Modes

The transition into the hold mode illustrates a slight transient (seen clearly in the heave rate signal at an OBC TIME of 35 seconds), due to the brief period of manual flight control (during which the collective setting was slightly higher than trim). The transition into the hold mode shows controller stability and accurate tracking of set points.

In the deck tracking mode, the helicopter is seen to correct it's altitude before proceeding to the required position. The landing occurs with an impact velocity of 0.5m/s before transitioning to the landed state (during which all control loops are disabled, barring the yaw rate control). Upon landing, the collective is lowered to reduce the force produced by the helicopter. The yaw rate controller remains enabled to ensure that the resulting moment is counteracted.

The slight transient seen late in the landed state is caused by a deficiency in the deck model. The introduction of the resolved forces causes the simulation to reduced the sample step size in order to better approximate the dynamic reaction. This causes the effective run time of the simulation to slow down, causing incorrect control actions to be calculated by the OBC. To counteract this, the step size was set to a fixed minimum step size, causing marginally incorrect dynamic reactions (small, balancing force reactions) to be calculated by the simulation. This was deemed to be an acceptable irregularity in the simulation, and is only noticeable after several seconds have passed.

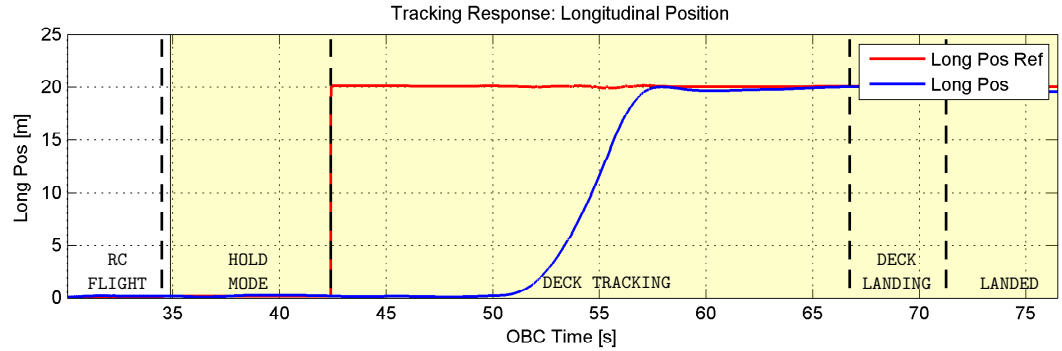

(a) Longitudinal Position Response

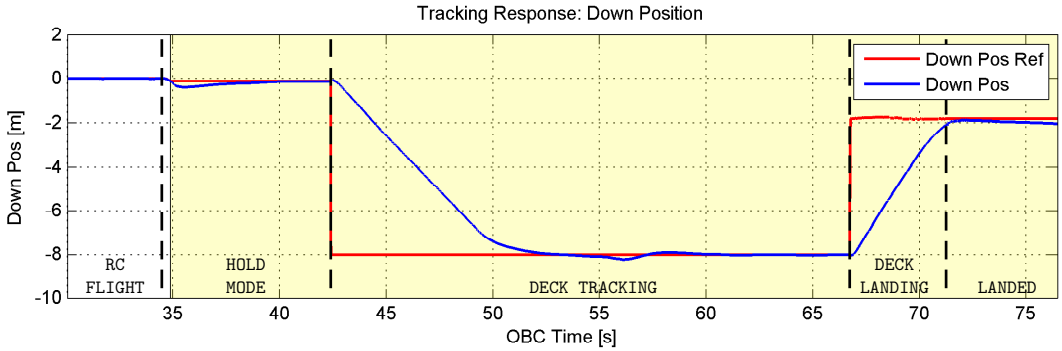

(b) Altitude Response

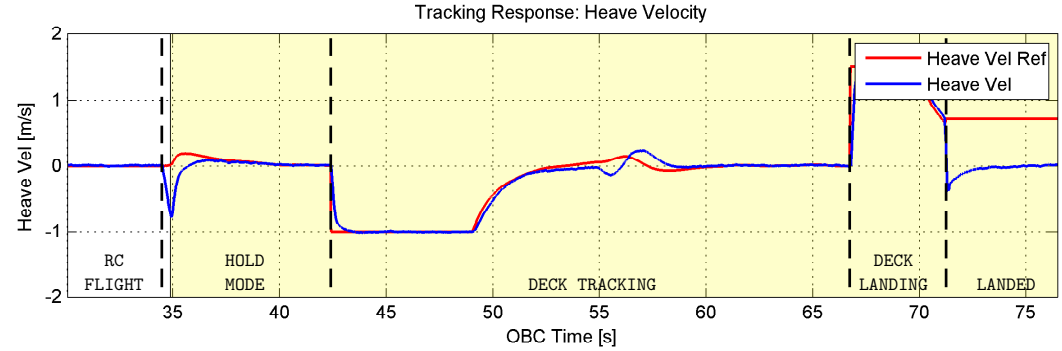

(c) Heave Velocity Response

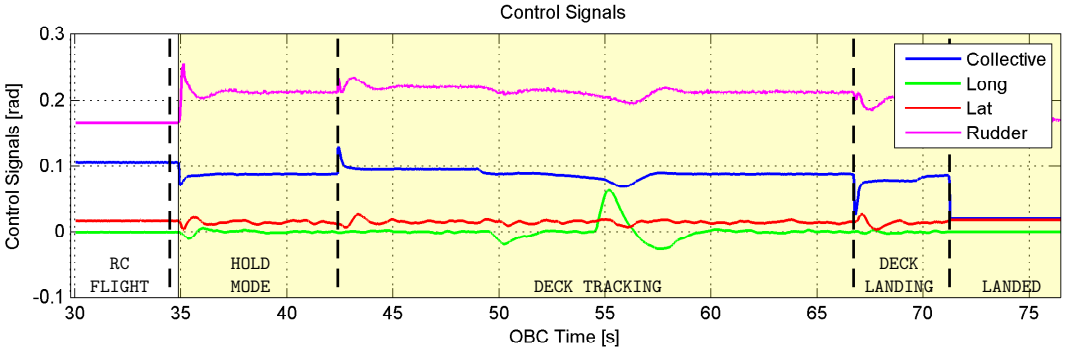

(d) Actuator Control Signals

Figure 5.7: Simulated Helicopter Landing using the full Hardware-in-the-Loop System

Chapter 6

Flight Test Results

In this chapter, the flight testing of the designed systems is discussed. The results are separated into four different sections, detailing the controller performance in the phases of its development. The first section describes the fundamental controller stability based on flight results and small step responses. The second section shows the helicopter's performance in forward flight, while the third and fourth sections detail the landing performance of the helicopter in the stationary and moving landing scenarios.

6.1 Controller Stability Testing

Controller stability testing was performed at the HRF Flying Club airfields, where the helicopter was manually flown to a safe altitude and the control system was enabled. To ensure safety, the helicopter was enabled in a hold mode, acquiring the trims from the piloted commands - managing a safe transition to the control system, and reducing the velocity to zero. All limits were reduced during this initial testing phase to ensure that the helicopter did not cause any untoward behaviour. In all the results shown in this chapter, the shaded area represents the region of time during which the controller was armed. During this test, the helicopter was flown in Single Point GPS mode (with no differential updates from the RTK system).

In this test, the helicopter was flown to an altitude of 15m before the controller was partially enabled (all controllers were enabled barring the outer loop position controllers. These were enabled after the helicopter

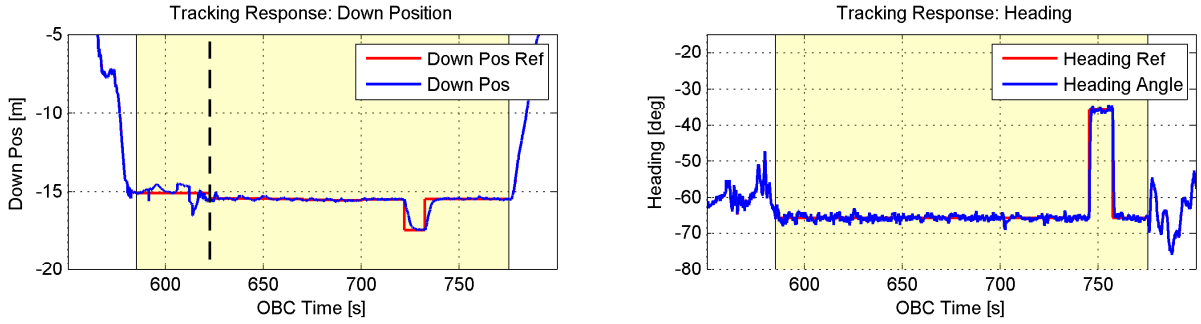

(a) Altitude Tracking Performance

(b) Heading Angle Tracking Performance

Figure 6.1: Controller Testing: Altitude and Heading Tracking Performance

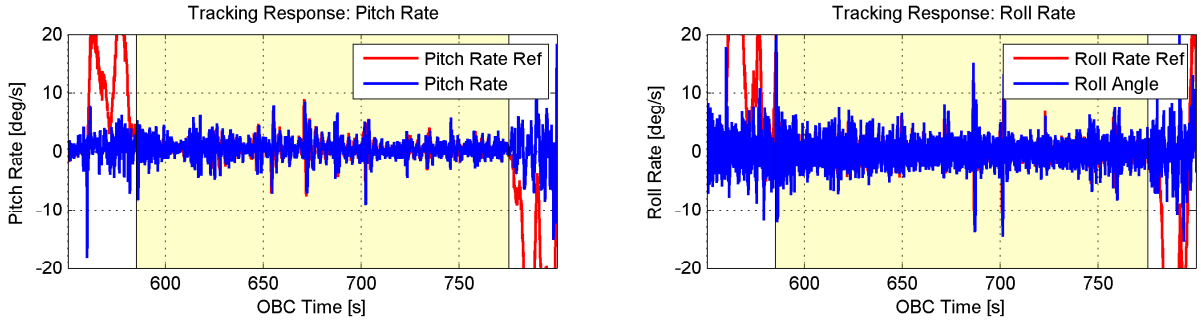

(a) Pitch Rate Tracking Performance

(b) Roll Rate Tracking Performance

Figure 6.2: Controller Testing: Pitch and Roll Rate Performance

was seen to be stable). Wind conditions during this test were not ideal, with mild wind conditions (estimated at around 2 - 3 m/s) on the ground. Figure 6.1b shows good tracking of the heading angle using fairly noisy measurements. The noise seen, on the order of 3° - 4°, is be due to the large amounts of vibration on the helicopter[1]. Despite this, the helicopter was found to accurately track its heading command with a fast settling time, accurately reaching it's setpoint within 2 seconds. During this test, the heading rate was limited to $10°/s$ (later updated to an operational limit of $40°/s$).

Altitude tracking was also found to work well, reliably maintaining it's position at hover with minimal deviation. It is well worth noting that these measurements were obtained using a Single Point GPS source. An updated solution in this case can potentially result in a shifted position estimate, creating erratic jumps such as those seen in Figure 6.1a at an OBC time of around 600s. Altitude regulation was found to improve as the solution was optimized, resulting in a cleaner performance as time went on.

Pitch and roll rate tracking, illustrated in Figure 6.2 was found to be on par with the modelled performance, rapidly damping disturbances and tracking the commanded setpoints. Similarly, the roll and pitch angle performance, seen in Figure 6.3, was seen to show fast accurate tracking of setpoints. The variations in the pitch and roll angles are due to sensor noise, the constant realignment of the helicopter's trim condition for hover (due to the velocity control system), as well as the impact of the position step responses.

Before the control system was armed, the pilot had attempted to align the helicopter with the wind direction. This is evident both in the large pitch offset angle[2] as well as the large variation in pitch angle, typical of a

[1]These measurements are post-filtering - even with constant feedback, the helicopter was seen to have a noticeable vibration on the tail boom. This effect appears to be an implication of the helicopter's design, where the vibration from the motor and the blades causes an aggravated vibration on the tail boom. This aggravated vibration causes mild fluctuations in the lift production of the tail rotor which is above the controller's bandwidth.

[2]During no-wind conditions, a standard helicopter would trim at a pitch angle of zero.

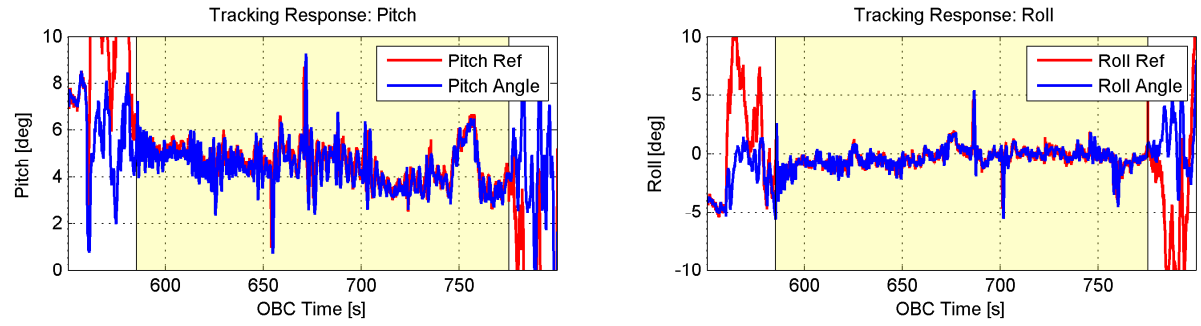

(a) Pitch Angle Tracking Performance

(b) Roll Angle Tracking Performance

Figure 6.3: Controller Testing: Pitch and Roll Angle Performance

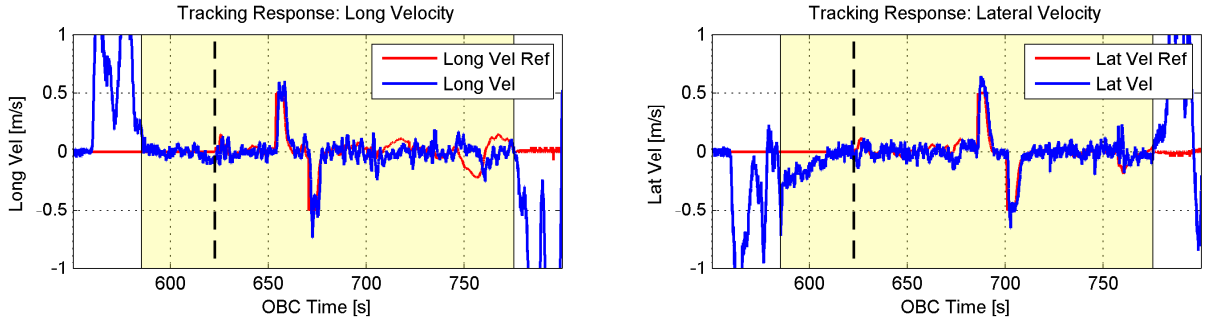

(a) Longitudinal Velocity Tracking Performance **(b)** Lateral Velocity Tracking Performance

Figure 6.4: Controller Testing: Longitudinal and Lateral Velocity Performance

helicopter attempting to fight gusty and turbulent wind conditions. The roll angle is affected with a similar but significantly smaller variation in angle.

Lateral and longitudinal velocity and position control was found to be responsive, accurately maintaining position despite the wind conditions. The velocity profiles of the helicopter are illustrated in Figure 6.4, showing a strong rejection of the variations in wind speed, and maintaining position when the position loops were armed. Position loops were armed at an OBC time of 622.7 seconds, indicated by the dashed line in Figures 6.4 and 6.5. Noise on the velocity, while not insignificant, was found to be more than adequate for the velocity control of the helicopter (velocity estimates from the GPS occur at 10Hz).

With the position and altitude controllers armed, the helicopter was given a series of step commands to test its ability to track a setpoint. Velocities were limited to 0.5 m/s, and step sizes were limited to 3m. The steps consisted of positive and negative steps in the longitudinal position, lateral position and heading angle setpoints.

Position and velocity measurements are transformed by the heading angle to give the longitudinal and lateral velocity and position estimates. Due to this, the noise and vibration occurring on the heading measurement is transformed onto the estimates and references. As this affects both the references and the estimates, the effect is effectively cancelled out in the errors unless far from the reference point (the effect is discussed further in Section **??**).

Position tracking performance was found to work well, maintaining position to within an error of 20cm[3], despite variations in wind. The large jump in the references near the end of the test is the effect of the heading

[3]This error is as it would appear to the helicopter, which would be affected by Single Point GPS drift. The performance with respect to a fixed reference would vary, although the variation would be small for a short time frame.

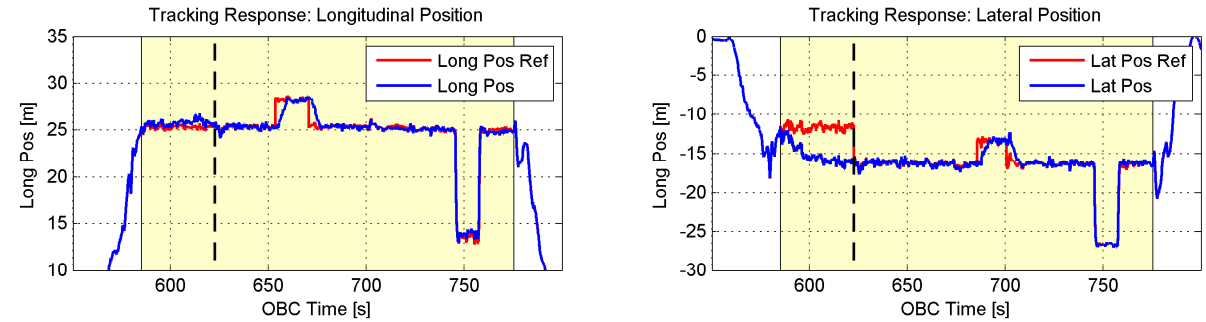

(a) Longitudinal Position Tracking Performance **(b)** Lateral Position Tracking Performance

Figure 6.5: Controller Testing: Longitudinal and Lateral Position Performance

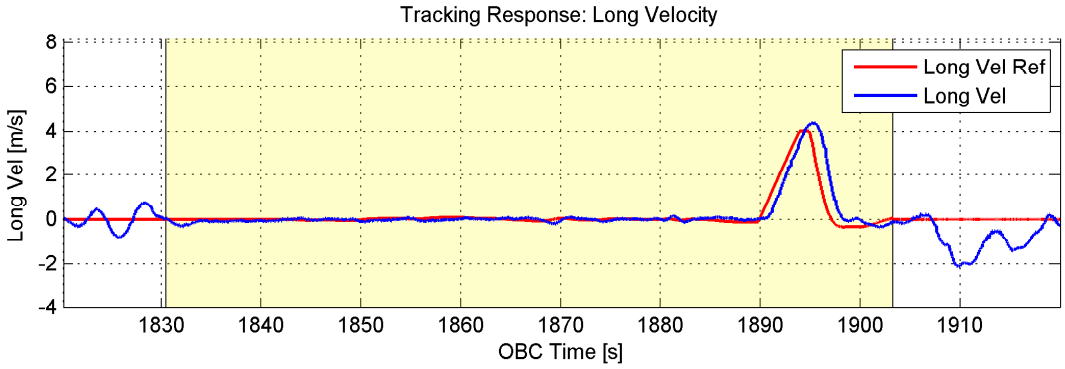

Figure 6.6: Longitudinal Velocity Tracking Performance

step, during which the references are transformed by a different value. Both measurement and reference are transformed, resulting in no additional control command being given to the helicopter.

6.2 Forward Flight Testing

Tracking a moving platform requires stability in fairly fast forward flight. The intention of these results is to illustrate the operation of the helicopter at practical test speeds in mild wind conditions. Conditions on the day were mild, with consistent wind speeds of around 3 to 4 m/s.

The velocity test consisted of a large position step (20m) during which the helicopter was limited in it's forward speed to the test velocity. Velocity tracking was implemented with a slew rate limiter to ensure accelerations were kept below 1m/s, ensuring a steady rise to the setpoint velocity of 4m/s.

The helicopter remained stable throughout the test, with the large velocity step negligibly impacting the other controllers. Altitude control in this situation, during which a pronounced altitude drop is typical, was found to regulate accurately - maintaining position to within 10cm when stationary, and experiencing transients of up to 20cm when accelerating. The altitude response and setpoint for this test is illustrated in Figure 6.7b.

Position tracking was found to perform accurately, overshooting the setpoint by only 50cm while reducing speed from 4m/s. The offset from the setpoint was corrected by the control system within 5 seconds. The position tracking performance is illustrated in Figure 6.7a.

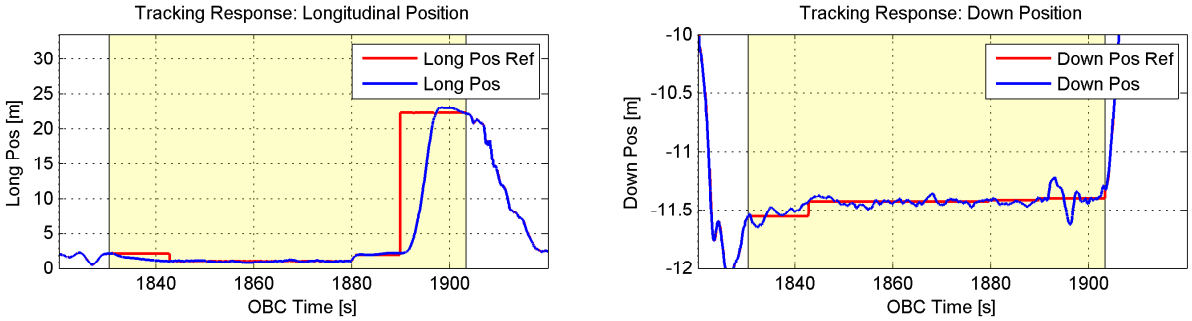

(a) Longitudinal Position Tracking Performance

(b) Altitude Tracking Performance

Figure 6.7: Controller Testing: Longitudinal and Altitude Position Tracking Performance

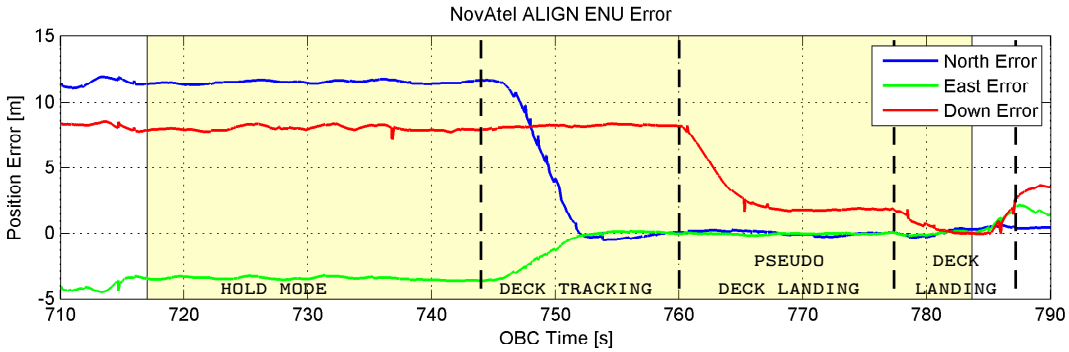

Figure 6.8: ENU Recordings from a Stationary Landing Attempt

6.3 Landing of the Helicopter on Stationary Platform

Before testing the helicopter on the moving platform it was necessary to test the landing controllers on the stationary, non-heaving reference point. This was first tested on a concrete landing pad at HRF in modest wind conditions.

In this context, the helicopter is initially guided with single point GPS readings before using the NovAtel ALIGN differential GPS mode. The NovAtel ALIGN mode provides the helicopter with a relative position measurement that can be used to accurately guide the helicopter to the intended landing point. The ENU vector, recorded from the landing is illustrated in Figure 6.8.

The helicopter begins by transitioning from the hold mode state into the deck tracking state. During this state, the helicopter seeks to position itself directly over the deck, minimizing the North and East errors. The helicopter successfully does this, after which a command is given from the ground station operator for the helicopter to enter a pseudo-deck landing mode. In this mode, the helicopter descends from it's tracking altitude of 8m to the an offset altitude of approximately 2m. After the landing command is given, the helicopter descends the final 2m to the ground, and searches for the acceleration spike that indicates that it has made contact.

In this test, ground effect was found to have a more significant effect than expected, and the helicopter touched down with an insufficient acceleration spike to cause a transition to the landed state (spiking at only 12 m/s^2, significantly below the threshold of 15 m/s^2). Due to this, the pilot was requested to resume control and take over the helicopter shortly after touchdown. The accelerometer reading is shown in Figure 6.9b. Despite the increased ground effect, the helicopter was able to perform a landing to within 0.4m of the target (the landing position errors can be seen in Figure 6.9a) .

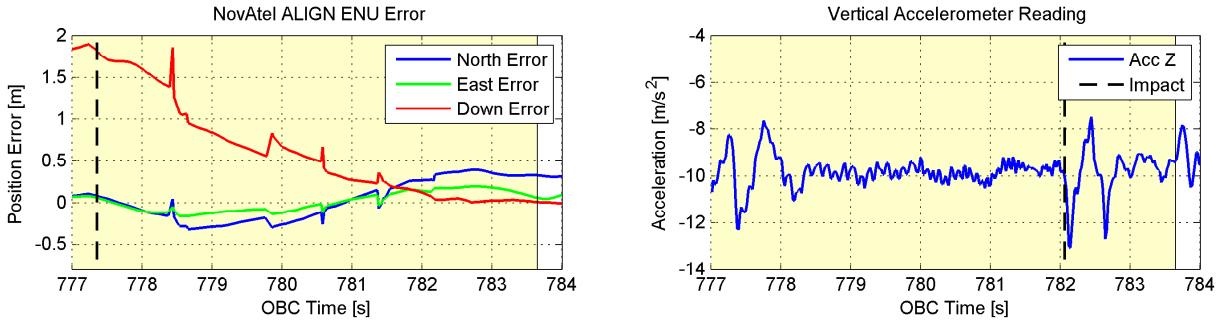

(a) ENU Landing Error

(b) Accelerometer Spike

Figure 6.9: Additional Information for Stationary Landing

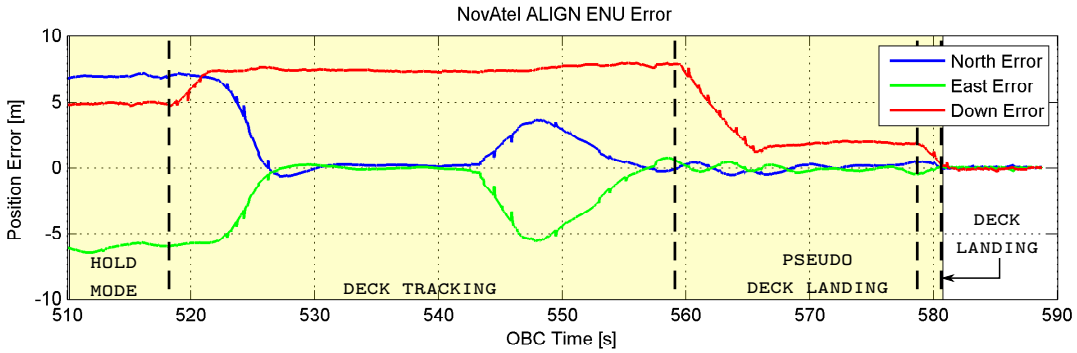

Figure 6.10: ENU Recordings from a Stationary Landing Attempt

6.4 Landing of the Helicopter on Moving Platform

Landing the helicopter on a moving platform proved to be a logistically challenging task, requiring advance planning and a careful approach. To facilitate the test, a 1-ton pickup truck was hired, alongside a 3m double axle trailer - to which a 3m x 3m grid was attached, as a representative moving landing pad. The NovAtel GPS Base Station was physically mounted on the platform to allow the use of the relative measurements provided by the ALIGN functionality. The landing operations were successful, with landings performed at vehicle speeds of 5kph, 10kph and 15kph[4]. Conditions were ideal, with mostly clear skies and mild, almost negligible wind speeds.

The test procedure began with the helicopter pilot flying the helicopter to a set altitude behind the deck before arming the autopilot. Once autopilot stability was confirmed, the helicopter was given a deck tracking command. In this mode, the helicopter is commanded to hover at a fixed altitude over the deck, minimizing the relative North and East measurements. Once settled, the driver of the vehicle begins driving at the required speed. The helicopter continues to track the deck and, after transients have subsided, is given the pseudo-landing command. The helicopter drops to an altitude of two meters above the deck, at which point - should the helicopter continue accurately tracking the platform - the landing command is given.

The system was found to track well, accurately following the platform with minimal error. The recorded ENU error vector for the 15kph (GPS: 11 kph) landing is shown in Figure 6.10, illustrating the system performance in various tracking modes. During the deck tracking mode, the helicopter was found to quickly and accurately reach the centre of the platform. Once the platform began moving, the helicopter rapidly began accelerating

[4]The vehicle speedometer settings appear to overestimate this velocity. GPS measurements indicate actual velocities of about 80% of these values

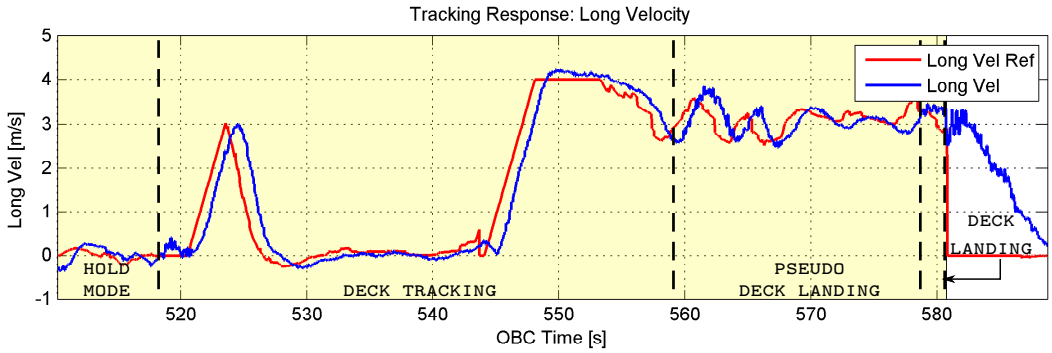

Figure 6.11: Velocity Profile of Landing Attempt

behind it, minimizing the associated transient within 10 seconds. The deck tracking mode in the illustrated data shows tracking at approximately 3 m/s or 11 kph (the velocity tracking response can be seen in Figure 6.11). The tracking velocity illustrated small transients when moving, appearing also as smaller transients in the position error profile (it is possible that is partially due to the variation in the forward speed of the vehicle, as the vehicle was driven across a fairly uneven field). The pseudo-landing mode, when entered, illustrated consistent steady-state altitude and position tracking performance with minimal transients or disturbances, decelerating to a hover gracefully whilst tracking the deck with minimal offset or overshoot.

Figure 6.12 shows several images extracted from the video footage of the landing attempts. Figure 6.12a illustrates the landing setup - in this image, the vehicle towing the trailer can be seen, as well as the helicopter hovering 2m above while in the pseudo landing state. Figures 6.12b and 6.12c, obtained from a GoPRO camera mounted on the platform, show the helicopter during the landing attempt and after the successful landing. These images were captured while moving at 11 kph.

The final landing command was given shortly after entering the pseudo-landing mode. In this case, the accelerometer spike (illustrated in Figure 6.13b) caused a transition to the landed state, during which the controller is effectively shutdown and disarmed. The final errors showed good tracking performance, with a very

(a) System Setup : Helicopter in Pseudo Landing State

(b) Helicopter during Landing State

(c) Helicopter in Landed State

Figure 6.12: Helicopter Landing Snapshots

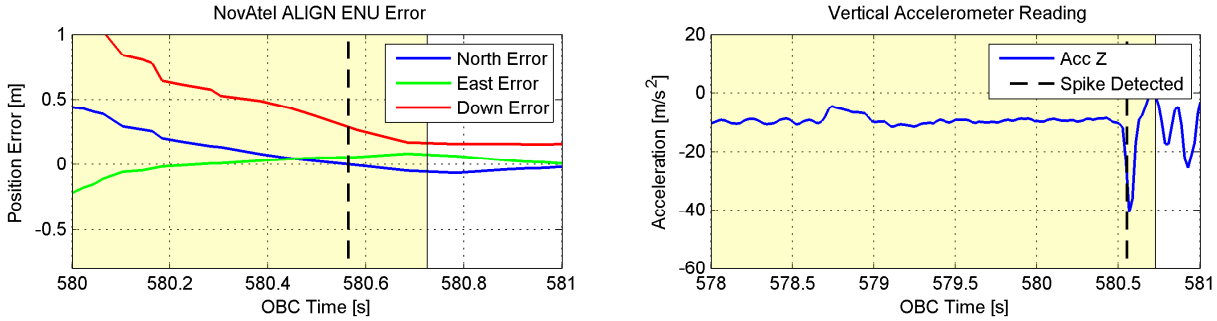

(a) ENU Landing Error

(b) Accelerometer Spike

Figure 6.13: Additional Information for Stationary Landing

small deviation from the intended landing position (illustrated in Figure 6.13a). The results from the landings are shown in Table 6.1.

Test Velocity	Landing Error [m]
0m/s (0 kph)	0.118 m
1m/s (3.6 kph)	0.18 m
2m/s (7.2 kph)	0.269 m
3m/s (11 kph)	0.05 m

Table 6.1: Recorded Landing Errors (based on ENU)

6.5 Conclusion

The practical helicopter landings were found to be congruous with the hardware simulated landings, achieving similar performance and errors. The autonomous landing system for the helicopter was found to work reliably for translating landings at speeds of up to 11 kph. Further testing is required to determine the functional bandwidth of the autonomous landings, although hardware-in-the-loop simulations indicate that practical landings at 20kph are achievable.

The practical tests were considered a successful demonstration of the autonomous landing system. Functionally, the helicopter was found to perform as designed, accurately tracking setpoints and performing landings on both stationary and moving targets.

Chapter 7

Quiescent Period Detection

The question of quiescent period detection for shipboard helicopter landings has been the focus of several studies and articles attempting to either predict or characterise the motion of a ship in order to ensure a safe helicopter landing.

The ship attitude constraints implemented for operational landings are stringent, requiring low roll and pitch angles to ensure that the helicopter remains close to its trim condition. Accelerations experienced by the helicopter at low angular deviations cause the helicopter to be particularly sensitive to ship motions once landed, and can result in dynamic roll-over and unwanted on-deck disturbances.

The helicopter landing procedures currently used in industry often involve some means of attachment to negate many of the effects experienced - these include the application of negative collective, and more radical methods such as the use of nets or harpoons to secure the helicopter (such as described by NATO (STANAG 1276), and implemented in systems such as RAST (Recovery Assist, Secure and Traverse system) by Indal Tech systems).

To minimize risk, quiescent periods are desired, the attempted detection of which is the subject of this chapter. In essence, this is with regard to the viability of a system that can qualitatively and conservatively predict suitable landing periods for the helicopter at sea, using only information available through the on-ship navigation system.

7.1 Safe Landing Characteristics

Characterising a safe landing opportunity (an opportunity where ship motions are within the dynamic constraints for a helicopter landing) is difficult, and operational bounds described by the Helicopter Certification Agency (HCA), NATO and the Navy (see section 2.2.2) are deferred to in order to ensure safety. A 'buffer' time, intended to represent a forward prediction requirement, was added before and after the unsafe windows so as to illustrate the performance of a predictive system over a simple state classifier.

Simulations show that approximately 3 seconds is required for a small unmanned helicopter to perform a landing, depending on the tracking altitude. This differs from the values needed by larger aircraft, where a full scale helicopter needs at least 6 seconds to land [41].

Heave and pitch motions are coupled when the deck is offset from the ship's centre of gravity, and a large pitch value can contribute significantly to heave. Both pitch and roll can cause significant contributions to dynamic rollover and their overall thresholds should be maintained for the duration of a landing attempt and shut-down period. Roll stabilisation for ships typically occur at speeds over 10 knots, while the longitudinal inertia of the ship tends to dominate for pitch motions, causing decreased relative amplitudes.

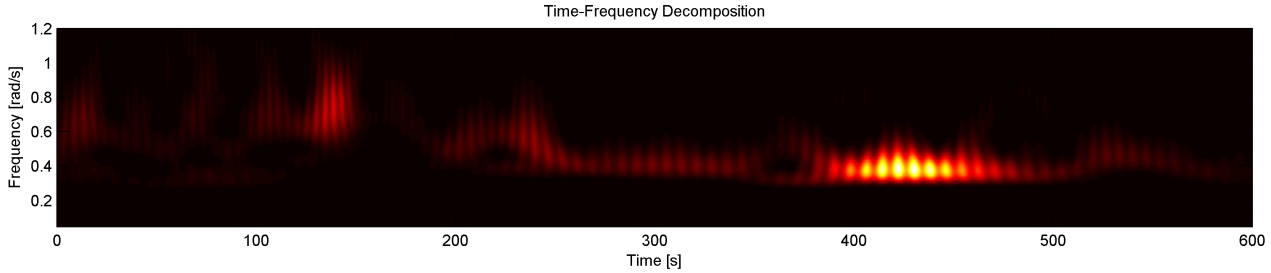

(a) Heave Spectrogram

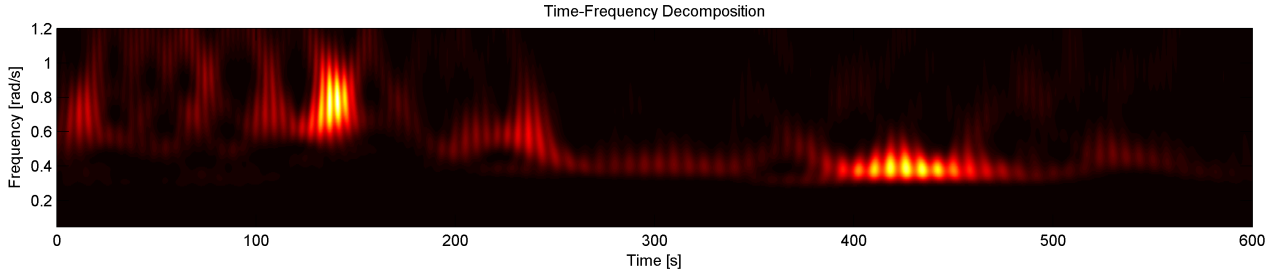

(b) Heave Rate Spectrogram

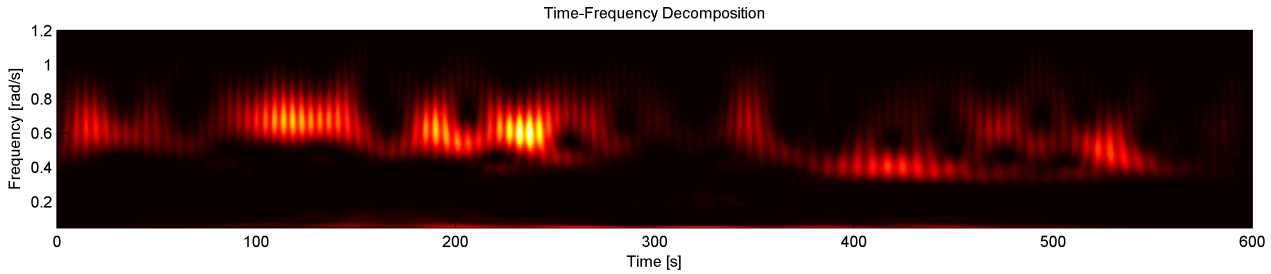

(c) Roll Spectrogram

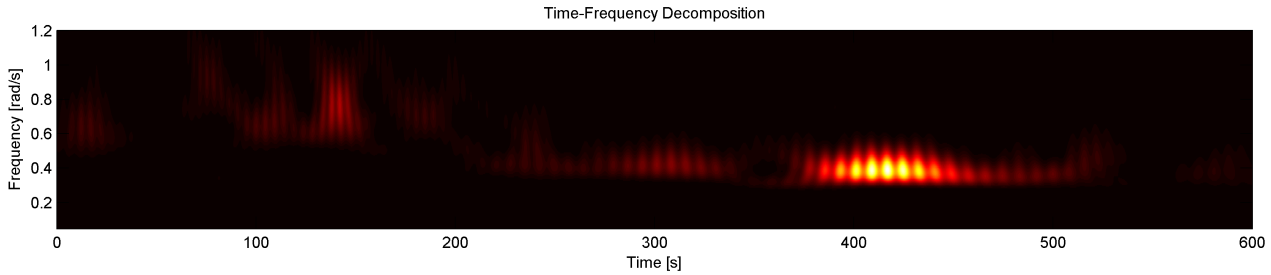

(d) Pitch Spectrogram

Figure 7.1: Spectrograms for Ship Data close to the coast (Data courtesy of SA NAVY)

Typical frequency spectra are shown in Figure 7.1 for a large (70m+) ship at sea (data courtesy of the South African Navy). The dataset consists of typical IMU outputs and includes information with regard to pitch, roll, heave, heading and their associated rates. The datasets are decoupled where possible using ship centre of gravity offset references. These spectra illustrate both deterministic and random trends in the ship's motion.

The spectra shown in Figure 7.1 were generated using a modified Time-Frequency decomposition analysis adapted from that described by Feron [45]. In order to approximate low frequency information, the Morlet wavelet width was adaptively changed to match between two and three periods of the target frequency. The

spectra show fairly low frequency modes, with most modes existing below 1Hz.

The spectra highlight fairly slow spectral shifts for the heave motions of the ship, but rapid and intense spectral fluctuations for roll and heave rate motions. Spectral shifts are important to note, as fast and unexpected shifts in spectral modes limit the accuracy of linear prediction systems to predict if these shifts do not correlate well with the time history used for the prediction generation. Modal drift over time appears to be fairly stochastic, and does not necessarily adhere to a causal pattern (i.e, it is not necessarily apparent when the modes will change.)

7.2 Safe Landing Prediction System Design

The safe landing prediction system is based on the aggregation of several linear prediction elements operating on the IMU data channels, producing a binary signal that can be interpreted by the ship's landing operator or by an autonomous system. The output command is essentially an indication on whether the prediction system considers the next 5 seconds to be safe - note that in this case, safe is considered to be the ship states that coincide with the operational limits defined in section 2.2.2. The binary command would typically be interpreted as a Green Light / Red Light indicator for landing operators, but could also be used to implement functional autonomous landings of rotary UAVs at sea.

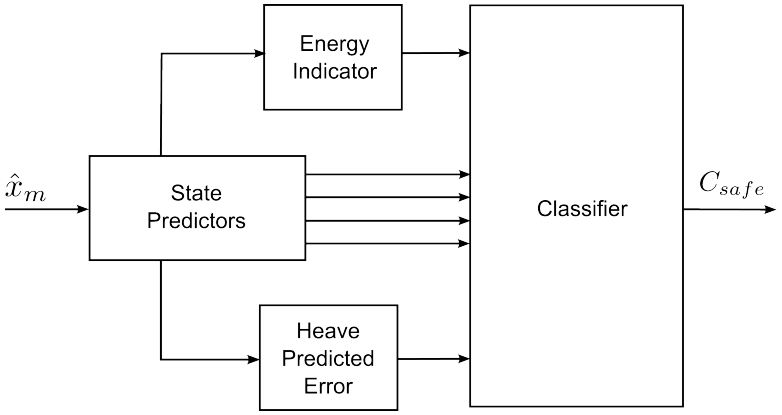

Figure 7.2: Safe Landing Prediction Structure

The predictor structure is shown in figure 7.2. Prediction is independently performed on each of the data channels (including heave, pitch and roll, their associated rates as well as yaw rate). The predictions are then passed into a classifier along with additional prediction based measures, including a predictive Energy Indicator and a measure of the helicopter's ability to follow the predicted heave motion (Heave Predicted Error). Details regarding these measures are described in the following sections.

7.3 Prediction Methods

IMU based prediction techniques rely entirely on historic data - implying that prediction capability is generally poor for fast changing modes or for significant changes in ship motion that do not correspond to a trend implicit in the data. However, given that spectral shifts are slow, fairly accurate prediction performance can be achieved

provided that prediction horizons are fairly short. If narrow bandwidth waveforms resembling 'Almost Periodic Functions' exist, then linear prediction techniques such as described by [46] can be effective, with potential prediction horizons of up to 30s [41]. These systems work particularly well for large wave amplitudes, where relatively narrow bands exist and the presence of wave coherence ensures statistical dependence in sea surface behaviour for periods of time equivalent to the reciprocal of the bandwidth [46].

Statistical prediction techniques include the use of Autoregressive Moving Average (ARMA) models [47], Kalman Filters and Neural Networks [48]. However, these algorithms, with the exception of the Neural Network implementation, are generally not able to maintain high degrees of accuracy (beyond 2 to 3 seconds prediction) in sea states 5 and above [48]. The neural network system was found by Khan [48] to operationally predict up to 7 seconds ahead (at which point it reaches a 50% chance of being within the confidence interval).

Alternative methods include prediction based on Minor Components Analysis (MCA), and Autoregressive functions [49], as well as a modified Prony Analysis presented by Yang [50]. Energy indicators can provide additional information regarding the overall energy in the ship, and are often used as a way to define safe landing thresholds ([51],[52]).

The results published by Zhao [49] show good performance for MCA prediction with acceptable accuracy and a feasible computational load. When compared to Auto Regressive or Neural Network equivalents, the author [49] found that the MCA analysis performed optimally, with autoregressive techniques forming a close second.

It should be noted that the performance of these algorithms is dataset specific, and that results may not be replicable in volatile or spectrally inconsistent datasets. In particular, the performance of many algorithms is motivated through simulated data which may have limited correlation with dangerous sea conditions.

A linear regressive predictor (as used in the generalized Prony analysis used by [50]) was chosen for this work due to its comparative performance, the ease of user control in its implementation, its decreased computational burden, and the results presented by Yang [50].

7.4 Generalised Prony Analysis

Prony analysis involves the fitting of exponentially decaying fixed frequency sinusoids to a dataset. These signals can then be analysed to note specific frequency contents and phase offsets. The signals are of the form,

$$y(t) = \sum_i A_i e^{\lambda_i t} \cos(\omega_i t + \phi_i) \tag{7.1}$$

These signals can be generalized to a sum of complex exponentials and constants. When limiting the summation to being real-valued (necessary as ship motion data is real-valued), it must be assumed that every complex value is associated with a complex conjugate. The generalized form is illustrated in Equation 7.2.

$$y(t) = \sum_i B_i e^{\gamma_i t} \tag{7.2}$$

where B_i and γ_i are complex values that fully encapsulate the information contained in the original prony specification. Using this form allows for constants, decaying, static and growing sinusoids as well as linear exponentials to be represented.

Prony analysis normally relates to the extraction of frequency information from a dataset. This can be accomplished through various linear model fits, and can be actively implemented by noting the relation to the z-transform operation. In this manner, the fitting of Prony class signals can be accomplished in real time by limiting a linear model fit to be of a zero-only form.

7.5 Generating a System Model

In order to extract components or perform predictions, a model of the system is first required. An approximate fit of the data to the time history is required and this was accomplished by means of a least squares model fit. This is discussed in the following subsection, along with the means by which frequency components and residuals can be extracted and prediction performed.

7.5.1 Linear Least Squares Model Fitting

A real-valued model encapsulating Prony class signals can be fitted using a difference equation implementation. There are several approaches of doing this, although the simplest is possibly through a least-squares approximation. Essentially, a model of the form,

$$y[n] = \sum_{i=1}^{m} a_i y[m-i] \tag{7.3}$$

can be fit to a dataset using $N+m$ recorded values, where N is the number of values used to minimize the solution. In order to ensure that the system is over-constrained (that only one solution exists), it is imperative that $N > m$, although $N >> m$ is preferred to help ensure a good fit. To perform a fit, the ideal values for ω in Equation 7.4 must be found.

$$Y = A\omega \tag{7.4}$$

where ω is the vector of weights to be solved for, $\omega = \{a_1, a_2, a_3, ..., a_m\}$, Y is the vector of recorded values and A is a matrix containing the delayed values, defined as follows,

$$A = \begin{bmatrix} y[n-1] & y[n-2] & y[n-3] & \dots & y[n-m] \\ y[n-2] & y[n-3] & y[n-4] & \dots & y[n-m-1] \\ y[n-3] & y[n-4] & y[n-5] & \dots & y[n-m-2] \\ \vdots & \vdots & \vdots & \ddots & \vdots \\ y[n-N] & y[n-N-1] & y[n-N-2] & \dots & y[n-m-N] \end{bmatrix} \tag{7.5}$$

Solving for the coefficients can be accomplished in a manner of ways. The simplest is possibly through the use of the Moore-Penrose pseudo-inverse, defined as

$$A^{\#} = \left(A^T A\right)^{-1} A^T \tag{7.6}$$

$$\omega = A^{\#} Y \tag{7.7}$$

The computational overhead of such an approach is high, as two matrix multiplications and an inversion must be performed to calculate the pseudo-inverse. Additionally, the system is susceptible to singularities and may be ill-conditioned should particularly calm or erroneous data be given. The Moore-Penrose pseudo-inverse is

mathematically analogous to a least-squares best fit.

There are several recursive methods that can be used to improve the computational efficiency of this estimation, including the standard Recursive Least Squares (RLS) as well as a Forgetting Factor Recursive Least Squares (FFRLS) approach. The benefits of a recursive procedure lie in the decrease in computation time as well as in increased simplicity of implementation.

The Forgetting Factor Recursive Least Squares was chosen for this project for its ability to give increased weighting to more recent samples (necessary, as the model of the deck motion will be shifting in its dominant modes over time, and it is imperative that the model is adapted to match the latest modes). FFRLS can be implemented based on the recursive equations shown in [50],

$$\omega[k] = \omega[k-1] + K[k]\left(y[k] - \psi^T[k]\omega[k-1]\right) \tag{7.8}$$

$$K[k] = P[k-1]\psi[k]\left(\gamma + \psi^T[k]P[k-1]\psi[k]\right)^{-1} \tag{7.9}$$

$$P[k] = \left(P[k-1] - K[k]\psi^T[k]P[k-1]\right)/\gamma \tag{7.10}$$

$$\theta(0) = 0, P(0) = \alpha I \tag{7.11}$$

In these equations, $\omega[k]$ represents the current estimation of the weights, $K[k]$ is the current control update and $P[k]$ is commonly referred to as an error covariance matrix. The value γ is the forgetting factor value, α is a large number used to initialize the covariance matrix and $\psi[k]$ is an $N \times 1$ matrix containing the data history values,

$$\psi[k] = (y[k-1], y[k-2], \ldots, y[k-m])^T$$

7.5.2 Component Extraction for Modal Estimation

Components can be extracted by noting that the coefficients of the difference equation are directly related to the z-transform coefficients. The modes can then be approximated as the zeros of the components can be directly related to exponential and frequency components. In order to do this, the roots of the z transform polynomial must be found.

$$\sum_i b_i z^i = \prod_i (z - z_i)$$

The roots of the function can be estimated by finding the eigenvalues of the Frobenius companion matrix (after dividing every coefficient by the coefficient of the highest power of z),

$$C = \begin{bmatrix} 0 & 0 & \cdots & 0 & -b_0 \\ 1 & 0 & \cdots & 0 & -b_1 \\ 0 & 1 & \cdots & 0 & -b_2 \\ \vdots & \vdots & \ddots & \vdots & \vdots \\ 0 & 0 & \cdots & 1 & -b_{n-1} \end{bmatrix} \tag{7.12}$$

These roots can be used to approximate system components by noting that the complex zeros can be converted to standard frequency interpretations using the conversion shown in Equation 7.13 [53].

$$\lambda_i = \begin{cases} \dfrac{\ln z_i}{T} & \text{if } z_i \in \Re \\ \dfrac{\ln |z_i|}{T} \pm \dfrac{j}{T} \arctan\left(\dfrac{\text{Im}\{z_i\}}{\text{Re}\{z_i\}}\right) & \text{otherwise} \end{cases} \tag{7.13}$$

Residuals are then found by fitting the current function data to the Vandermonde matrix of the component roots [53],

$$\begin{bmatrix} y[n-N+1] \\ y[n-N+2] \\ y[n-N+3] \\ \vdots \\ y[n] \end{bmatrix} = \begin{bmatrix} 1 & 1 & 1 & \cdots & 1 \\ z_1 & z_2 & z_3 & \cdots & z_n \\ z_1^2 & z_2^2 & z_3^2 & \cdots & z_n^2 \\ \vdots & \vdots & \vdots & \ddots & \vdots \\ z_1^N & z_2^N & z_3^N & \cdots & z_n^N \end{bmatrix} \begin{bmatrix} B_1 \\ B_2 \\ B_3 \\ \vdots \\ B_n \end{bmatrix} \tag{7.14}$$

These values can then be used to isolate the dominant components associated with the signal. Using these analyses, components can be tracked or specific components can be removed to stabilize predictions. While relevant to analyses, component extraction was disregarded in the final system due to its limited enhancement capabilities in motion prediction. However these components, although computationally expensive to extract, remain a means to provide data that could potentially be useful for improved classification.

7.5.3 Prediction

Prediction was implemented by iteratively calculating predicted values based initially on measured values, and later on previously predicted values. The scheme is illustrated in the following equations, which are iterated until the number of required prediction points are achieved.

$$y[n] = \psi^T[n-1] \cdot \omega \tag{7.15}$$

$$\psi^T[n] = \left(y[n], \psi^T[n-1]\right) \tag{7.16}$$

where the elements of $\psi[n]$ exceeding the length of the weights vector are discarded. This is referred to as auto-regressive model prediction [54].

7.6 Prediction System

This section details the performance of the individual prediction systems. Predictions were based on the modelling described above, and is autoregressive in nature. As described in the system design, prediction was performed on roll, pitch, heave, their associated rates, and yaw rate.

7.6.1 Parameter Choice

The fundamental parameter selections were the order (σ), sampling rate (f_s), and forgetting factor (γ) for each predictor. The sampling rate was chosen to be 4 Hz, allowing frequencies of up to 2Hz to be predicted. Higher rates were originally used but did not provide any significant improvement in prediction quality.

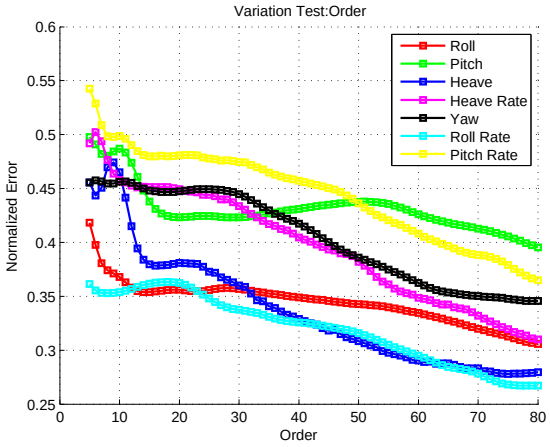

(a) Variation of Parameters Results : Order Variation around $\gamma = 0.995$

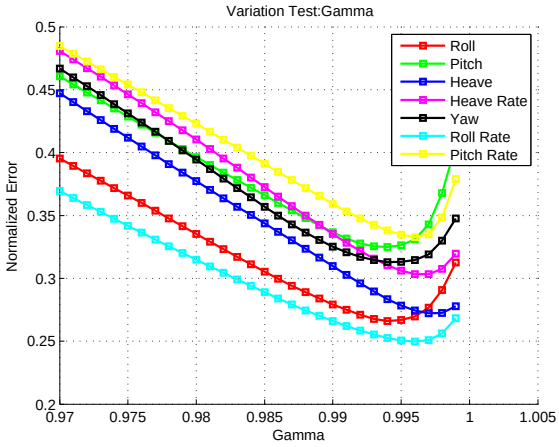

(b) Variation of Parameters Results : Forgetting Factor Variation around $\sigma = 75$

Figure 7.3: Results of a Variation of Parameters Optimization Scheme around Local Optimums

Order and forgetting factor choices were motivated by the results of a variation of parameters process on a modestly volatile dataset. The results were normalized to the maximum amplitude of the signal in question, and are shown in the figures 7.3a and 7.3b.

Prediction capabilities were found to improve significantly with increased orders. Order values are particularly important with regard to prediction bandwidth, limiting the minimum representable frequency to $2\pi/(\sigma t_s)$. Analytically (based on the spectrogram results shown in Figure 7.1), one would presume that an order of 60 would provide an optimal error for heave, due to the 0.4 rad/s frequency minimum (implying a speculative value for σ as $\sigma = 62.8 \approx 63$). The data shown in Figure 7.3a reflects this but does not show significant decreases for heave beyond $\sigma = 50$.

The final parameter choice was chosen to be a forgetting factor of 0.995 and an order of 75 for all prediction elements. Note that these parameters are optimized with regard to the prediction error normalized to the maximum amplitude of the channel. This implies that the numbers favour stability in prediction and lower order exponentials over prediction quality at specific time instances. Empirically chosen gains such as these should be dataset dependent, however, no significant shifts were found between datasets with regard to optimal parameter choice. Larger sigma values generally gave better results, but plateau at specific error values depending on the dataset used.

7.6.2 Prediction Performance

Independent state prediction was found to perform fairly well, with accurate prediction times ranging from the order of 15 seconds to 4 seconds, depending on the bandwidth of the sea states in question. Prediction performance for a dataset was based on the absolute error relative to the relevant limit, where an error of less than 20% of the limit is desired. To illustrate this, the predictive errors for a stable dataset (low spectral shifts) and a more volatile sea state (large, aggressive spectral shifts) are shown in Figure 7.4. Note that the scaling implies that error margins increase by up to a factor of two for a volatile dataset over the non-volatile dataset. The graphs shown in Figures 7.4a and 7.4b were generated from independent 600 second datasets (10 minutes) and include all predictions within that time frame.

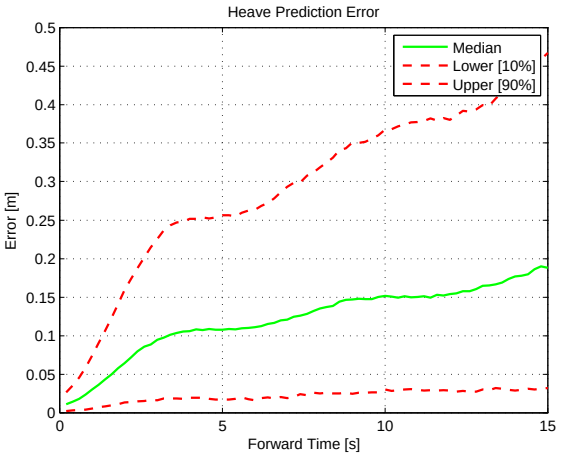

(a) Heave Predictions for Stable Dataset

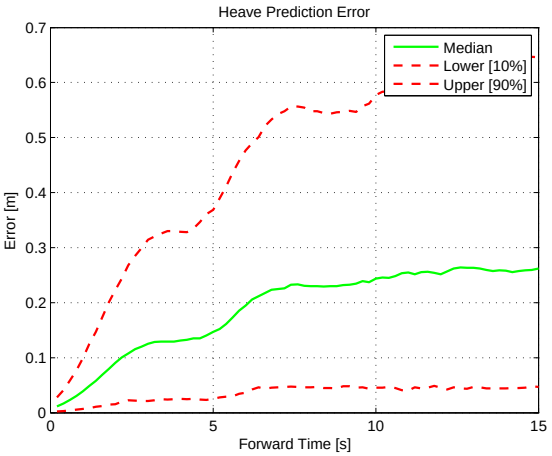

(b) Heave Predictions for Volatile Dataset

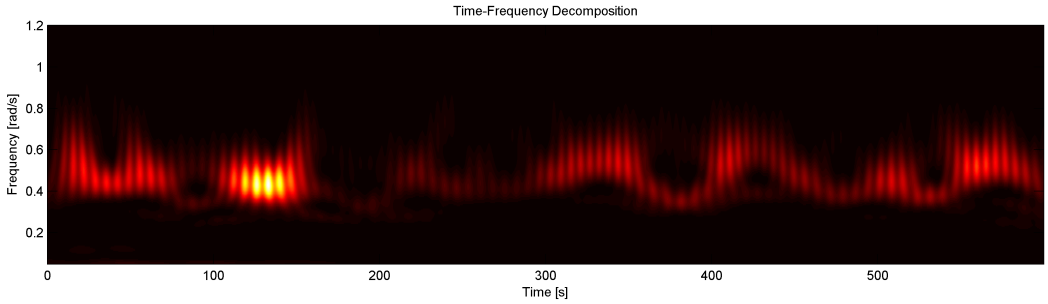

(c) Spectral Intensities for Stable Dataset

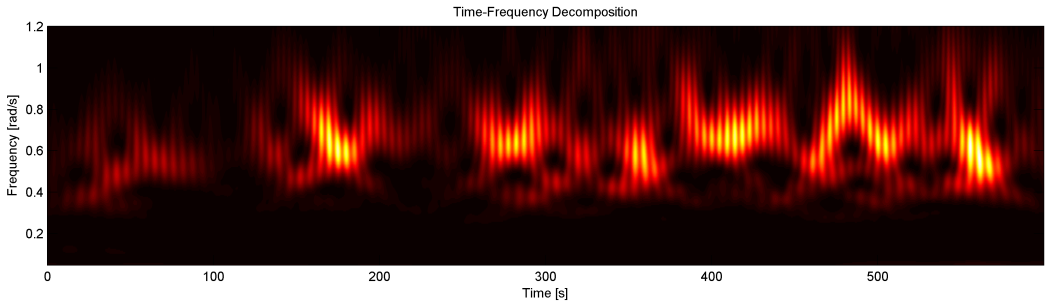

(d) Spectral Intensities for Volatile Dataset

Figure 7.4: Heave Prediction Capabilities in Differing Sea Conditions

Heave prediction shows strong accuracy for a 5 second forward prediction, with a median value ranging from 10cm to 15cm accuracy along with a 90% chance of being within 35cm. Error margins increase dramatically for longer prediction times, passing a worst case error margin of 0.5m (50%) at 7 seconds.

Actual predictions vary in stability, depending on the spectral fluctuations implicit in the system. For the same dataset, heave predictions for 5 second, 10 second and 15 second forward prediction times are shown. The 5 second predictions are generally fairly accurate, whilst the 10 second and 15 second predictions show varying accuracy and poor prediction quality for distant rising amplitudes. Fast changes in behaviour are particularly difficult for the system to track and the prediction quality was found to depend entirely on the dataset used.

For most datasets, it was found that, on average, prediction performance degraded heavily when predicting beyond a 7 second window, and the system was often unable to predict large or sudden changes so far in the future. As such, the chosen forward prediction time was elected to be 5 seconds in order to account for potentially fast changes in mode - the advance warning for which is often not implicit in the historic data.

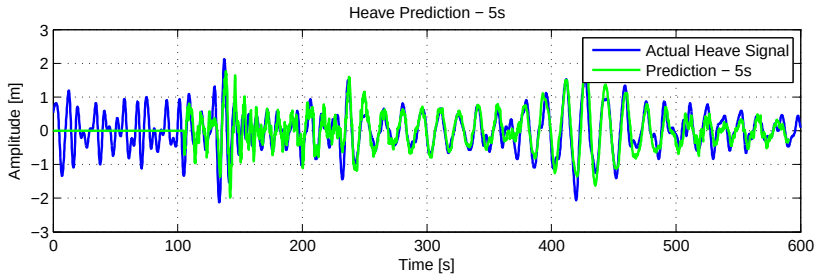

(a) Results of a 5 second forward prediction

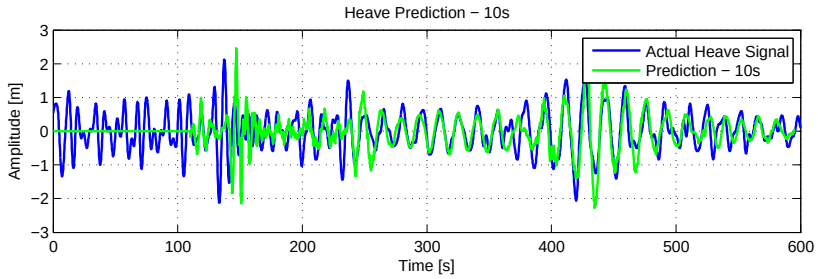

(b) Results of a 10 second forward prediction

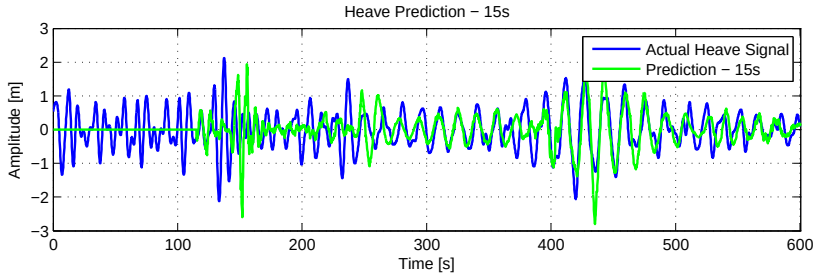

(c) Results of a 15 second forward prediction

Figure 7.5: Predictive Capabilities on a Reasonably Volatile Dataset

The results for a roll prediction are shown in Figure 7.6, where in general the spectral fluctuations have a far higher frequency and bandwidth, significantly reducing the integrity of the forward prediction.

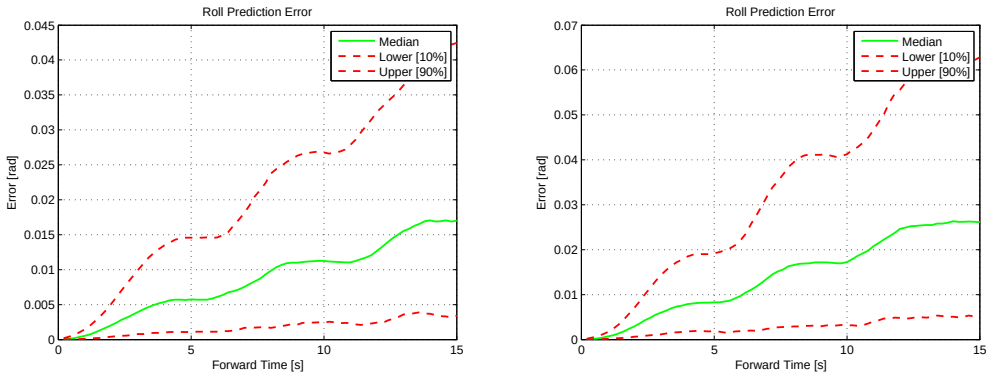

(a) Roll Predictions for Stable Dataset **(b)** Roll Predictions for Volatile Dataset

Figure 7.6: Roll Prediction Capabilities in Differing Sea Conditions

A 5 second prediction time, as used in the classifier, was found to generally ensure homogeneity in the prediction capabilities across datasets with varying spectral volatility. Prediction capabilities, while normally acceptable at 5 seconds, were found to be decidedly more erratic for angular prediction measurements, particularly for pitch prediction (possibly due to the non-linear disturbances caused by wave collisions when travelling at speed). More accurate predictions (based on the results shown in [42],[54],[48]) could potentially be obtained using

more advanced methods. Due to the dataset dependent nature of motion prediction, full-scale testing and implementation is required to verify the applicability of results in literature to this use-case.

7.6.3 Impact of Spectral Coherence on Prediction

One of the implicit assumptions in the use of linear prediction is that the spectral composition of the ship motion at the time of prediction is maintained for a set amount of time into the future. Many papers that test algorithms for ship motion prediction make use of simulated data that is inherently deterministic or completely periodic, implying that their results cannot necessarily be emulated in a real-data scenario where conditions to not necessarily conform to a cyclic, deterministic process.

In order to test the potential prediction quality that could be obtained, a prediction coherence chart was created in an attempt to determine at which point, for a given dataset, spectral coherence is lost when looking forward into the future. For this purpose, spectral coherence is considered a measure of correlation of the spectral information between two time instances, defined as,

$$C_{XY} = \frac{\left(\sum_{\omega=0}^{\omega_n} X(\omega)Y(\omega)\right)^2}{\sum_{\omega=0}^{\omega_n} X(\omega)^2 \cdot \sum_{\omega=0}^{\omega_n} Y(\omega)^2} \tag{7.17}$$

where X and Y are the spectral intensities at two separate time instances. Using the output of the spectrograms, this technique was used to test coherence loss in forward prediction that could be used to gauge practical limits of prediction. Two examples of coherence loss, one for a fairly volatile dataset, another for a non-volatile dataset

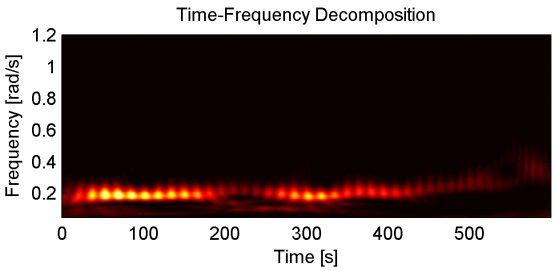

(a) Spectrogram for Non-Volatile Heave

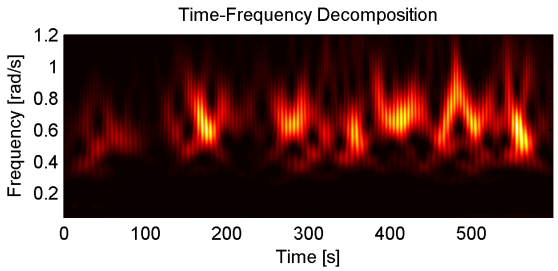

(b) Spectrogram for Volatile Heave

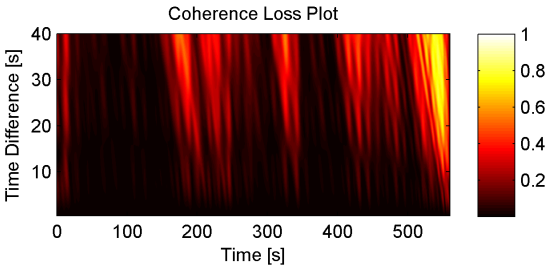

(c) Coherence Loss for Non-Volatile Heave

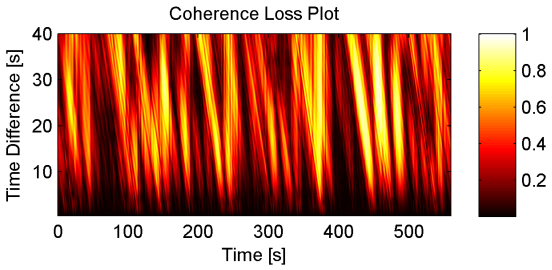

(d) Coherence Loss for Volatile Heave

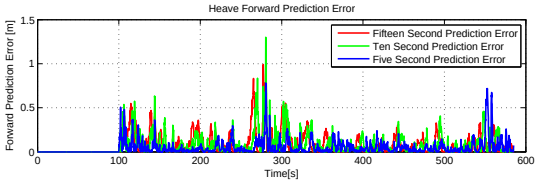

(e) Predictive Error for Non-Volatile Heave

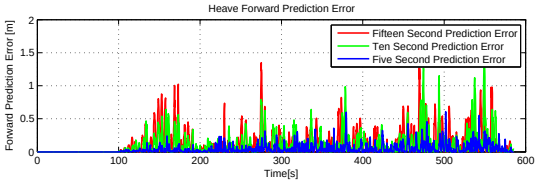

(f) Predictive Error for Volatile Heave

Figure 7.7: Impact of Coherence Loss on Prediction Capability

are shown in Figure 7.7.

In this circumstance, volatility refers to the practical prediction limit to which coherence is maintained. A volatile dataset would be considered anything with fluctuating coherence horizons below 6 or 7 seconds (coherence loss of around 0.5), and a non-volatile dataset where prediction can be accurately maintained for over 10 seconds. To illustrate the impact of coherence loss on this system, the instantaneous prediction error is shown alongside the spectrograms and coherence loss plots.

7.6.4 Heave Error Propagation

An analytical error was derived to give an indication of the helicopter's ability to track a given heave signal. This was accomplished by passing the predicted heave signal through a linear model representative of the helicopter's closed loop heave dynamics, and subtracting the output from the original prediction. The RMS value of this 'error' prediction was then used as an indication of the helicopter's tracking ability for the predicted motion.

The heave error propagation system is illustrated in the diagram below,

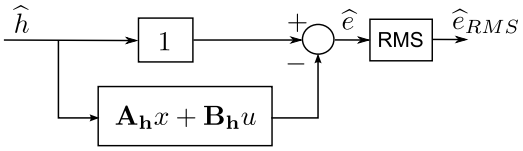

Figure 7.8: Heave Error Propagation System

The simplified heave model used for the estimator was based on the design in Section 3.5.1. The heave model can be reduced to a 3rd order system of the form,

$$\begin{bmatrix} \dot{x_1}(t) \\ \dot{x_2}(t) \\ \dot{x_3}(t) \end{bmatrix} = \begin{pmatrix} -6.74 & 5.09 & -3.98 \\ -1.0 & 0 & -0.7 \\ 1.0 & 0 & 0 \end{pmatrix} \begin{bmatrix} x_1(t) \\ x_2(t) \\ x_3(t) \end{bmatrix} + \begin{pmatrix} 3.98 \\ 0.7 \\ 0 \end{pmatrix} u_1(t)$$

$$y(t) = \begin{pmatrix} 0 & 0 & 1.0 \end{pmatrix} \begin{bmatrix} x_1(t) & x_2(t) & x_3(t) \end{bmatrix}^T$$

This model can then be used to provide an indication of the helicopter's ability to track a given heave reference. Results show a slight phase advance over the actual heave signal and could potentially provide a useful indicator of an unsafe deck. An example of this is shown in Figure 7.9.

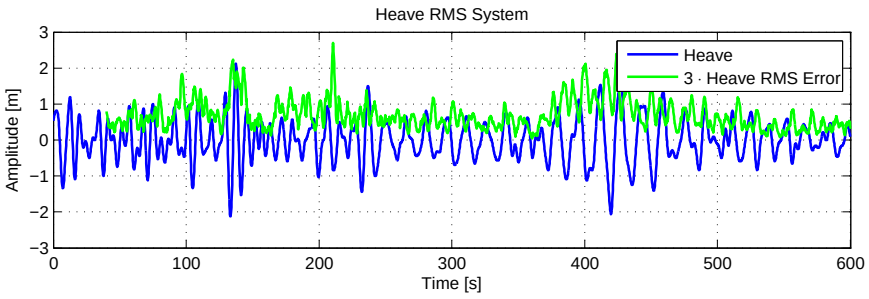

Figure 7.9: Heave Error Propagation Results

7.6.5 Total Energy Prediction

An ideal landing period may coincide with a local minimization of the kinetic energy of the ship. In terms of the system, a surrogate was constructed based on the examples shown in [52]. The Energy Indicator (EI) used in the system was defined to be,

$$EI = \alpha_\phi \dot{\phi}^2 + \alpha_\theta \dot{\theta}^2 + \alpha_\psi \dot{\psi}^2 + \alpha_h \dot{h}^2 \tag{7.18}$$

where $\dot{\phi}$, $\dot{\theta}$ and $\dot{\psi}$ are the roll, pitch and yaw rates respectively and $\dot{h}$ is the heave rate. The weighting factors $\{\alpha_\phi, \alpha_\theta, \alpha_\psi, \alpha_h\}$ were chosen to ensure equivalent contributions from the relative sources. Being an aggregate of several different predictions, the energy predictive error is logically the aggregate of the individual predictive errors, implying a lessened prediction capability. However, the EI indicator shows useful information in determining critical landing points, and the 5 second prediction shows correlation with the actual system energy. An example is shown in Figure 7.10 of the system energy for a given dataset.

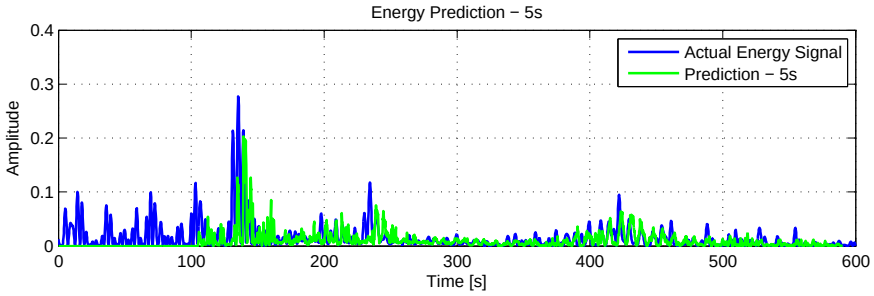

Figure 7.10: A 5 second ahead Energy Prediction

Largely due to the increased error margins implicit in the linearly coupled predictions, absolute energy prediction was found to be fairly insensitive and delayed, providing occasionally good predictive qualities but fairly poor advance information to the system during incoherent conditions.

7.7 Classifier Design

An empirically tuned classifier, wherein sensitivities were chosen based on the output performance, was used to generate the landing command. The output was compared to an automatically generated ground truth in order to determine the effectiveness of the system. This section discusses both the ground truth generation, as well as the manner in which the classifier was structured before presenting results. Note that in order to ease the implementation of the classifier, an affirmative signal (1) indicates a no-land condition, while a negative condition (0) indicates that it is safe to land. The system was tuned to favour conservative behaviour - the cogency of this argument favouring safety concerns over absolute predictive performance.

7.7.1 Ground Truth Generation

An automatic, acausal ground truth generation procedure was developed based on imposed limits. This system, implemented offline as a post-analysis of the recorded data, provides a means of grading the performance of the prediction classifier. For a given signal, the ground truth was found by finding any value exceeding the limits within a given window and placing a box of a specific width around the point (before and after). Multiple windows are aggregated to generate a smooth ground truth. This ensures that the ground truth is very

conservative and imposes an implicit requirement on the prediction abilities of the system. For this section, Ground Truth signals are always defined as red signals, whilst prediction signals are presented as green signals.

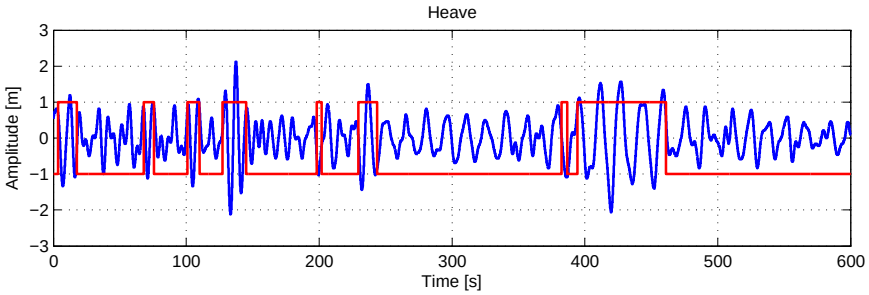

Figure 7.11: Automatic Ground Truth Generation for a Heave Signal

The ground truth width was chosen to be 6 seconds, creating a 3 second before and after requirement for predictions (the typical landing time requirement for a UAV helicopter). This ensures that when classifications are compared to the ground truth, classifications have the implied prediction requirement as well as a measure of conservatism.

7.7.2 Classifier Operation

The classifier was implemented as the aggregate of the individual limit classifications. If any of the limits imposed on the system are exceeded, the system will generate a hold off command,

$$\overline{C_{land}} = C_\phi + C_\theta + C_h + C_{\dot{h}} + C_{\dot{\theta}} + C_{\dot{\phi}} + C_{\dot{\psi}} + C_{HE} + C_E \tag{7.19}$$

The individual classification of a given signal was based on the prediction signal combined with a robustness filter. For a given point sensitivity σ_x and limit θ_x, the classification was the sum of the points exceeding the limit greater than the sensitivity value. The value chosen for σ_x thus is a measure of how many of the forward predicted points must exceed the bounds in order for the classifier to consider the limit exceeded. This ensures that boundary cases do not cause overtly conservative behaviour, and that prediction signals with high levels of random coherence loss, such as roll rate or pitch rate, can be limited to providing a more constrained classification.

$$C_x = \sum_j (x(j) > \theta_x) > \sigma_x \tag{7.20}$$

In addition to the sensitivity parameter for the individual predictions, a delay was added to the classifier to only allow the system to revert to a 'safe landing' state if a certain amount of time has passed during which the sea states are within operational limits. This was added to enforce conservatism in prediction and to ensure that the global indicator does not oscillate when close to a boundary limit (instead, the landing opportunity will be deemed unsafe).

7.8 Classifier Performance

The classifier's performance was graded on two datasets defining the two primary cases of system operation. The first dataset is used to grade the system's performance in a sea state where conditions are generally unsafe but occasionally safe (referred to as a High Energy dataset). The second dataset is used to illustrate the system's performance in conditions that are generally safe, but occasionally unsafe (referred to as a Low Energy dataset).

7.8.1 Classification for a High Energy Dataset

Classifier performance is largely dependent on the datasets used, particularly with regard to spectral coherence. Severe operational limits enforce a relatively stringent requirement on the system to locate ideal landing periods. When on the border of operational limits, as in the case of the dataset illustrated in Figure 7.12, prediction is difficult and the system errs on the side of conservatism.

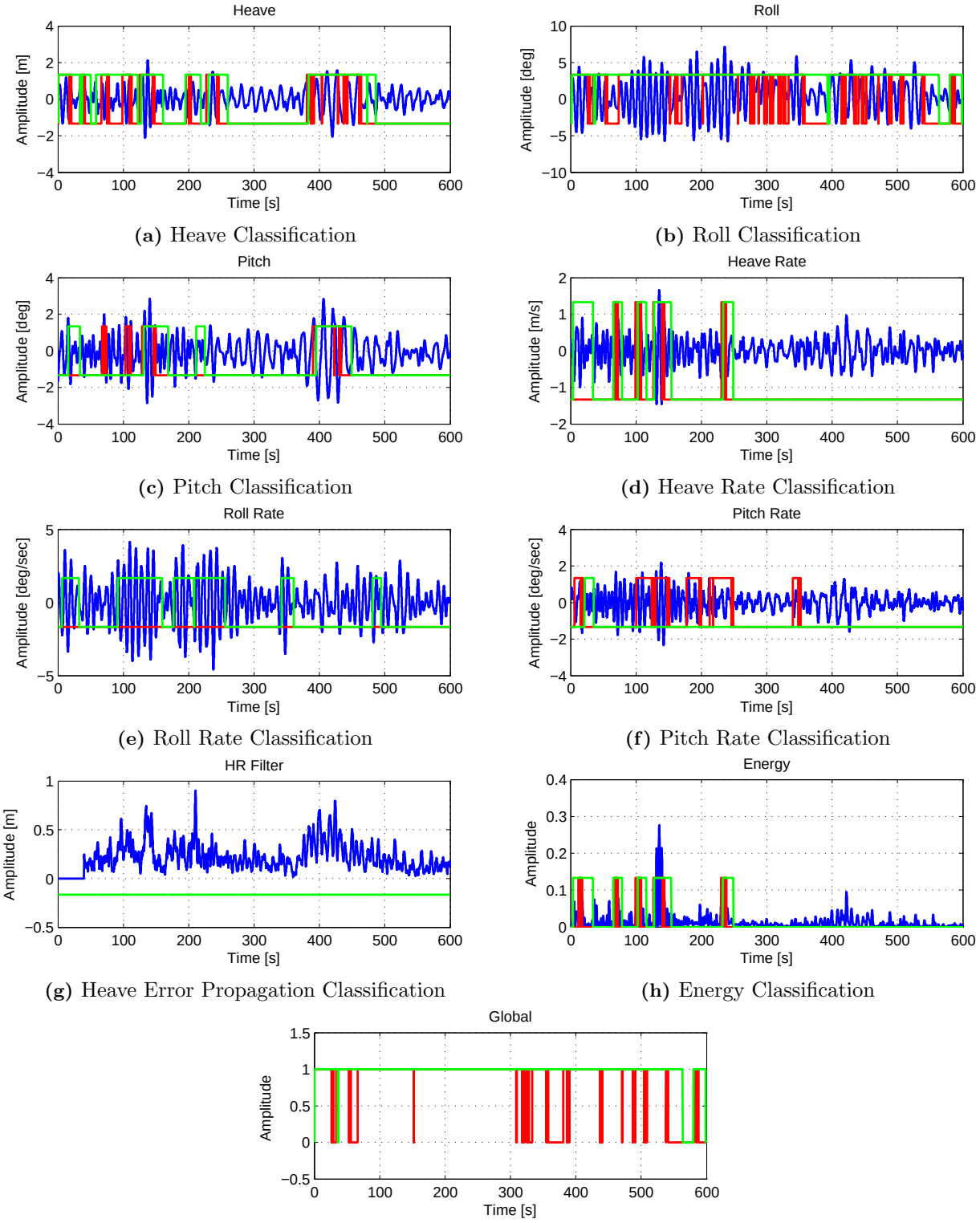

(a) Heave Classification

(b) Roll Classification

(c) Pitch Classification

(d) Heave Rate Classification

(e) Roll Rate Classification

(f) Pitch Rate Classification

(g) Heave Error Propagation Classification

(h) Energy Classification

(i) Final Classification (aggregate)

Figure 7.12: Prediction for a Volatile Dataset

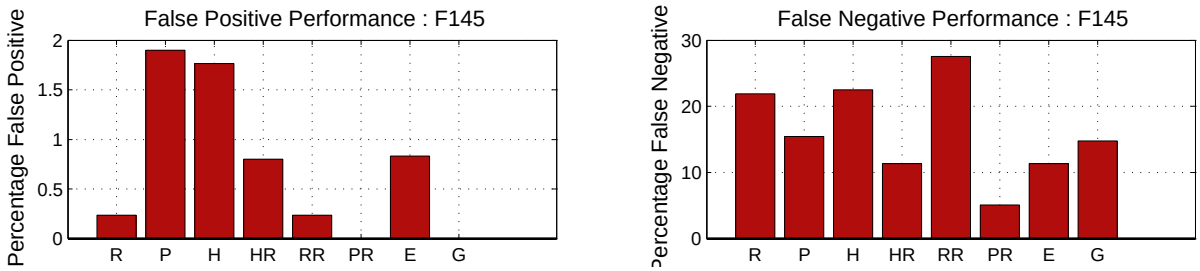

(a) False Positive Performance

(b) False Negative Performance

Figure 7.13: Classifier Performance

Noticeably, the roll angle limitation causes the system to remain largely 'unsafe' throughout the dataset. Of particular interest is to note that occasional spikes do occur that the system either fails to predict entirely (generally implying a minor limit transgression), or fails to predict sufficiently in advance (where the green line spikes after the red line, implying that the system failed to provide the required 3 second warning time).

When these individual predictions are combined, the aggregate structure of the classifier provides conservatism with a fair amount of forewarning before bounds are exceeded. However, the increased conservatism does cause several potential quiescent periods to be missed. This is reflected in the False Negative and False Positive statistics (see Figure 7.13), where occasional false positives do occur, but the global false positive statistic remains low. However, this causes an increase in the number of false positives seen, reducing the total number of safe landing opportunities that the system will find.

Results show that overall the system is able to predict the majority of instances during which particular measurements exceed limits, as well as generally predicting these instances several seconds ahead of time. The significant outcome of this is to see that the system is able to predict points where the helicopter is unable to land, thereby largely ensuring safety in the helicopter-ship operational interface.

7.8.2 Classification for a Low-Energy Dataset

In this dataset, the classifier's performance is evaluated on a low-energy, or fairly stable dataset. The intention is to evaluate the systems ability to predict in conditions that are generally 'safe', during which short 'unsafe' periods exist. The overall energy of the system is significantly lower, when compared to that in Figure 7.12. However, short limit transgressions do occur, and the system is required to predict these while still providing successful indication of potential landing periods. In this case, limit transgressions are entirely due to a single state (roll angle), thus losing the advantages provided by the aggregate design of the system.

The output of the classifier is shown in Figure 7.14. The system is seen to be conservative, but due to conditions being exceeded by a single state, the system struggles to provide any form of collaborative prediction, limiting the advance warning given by the system. However, the system is still able to largely predict the transgressions, although occasionally narrowly missing the 3 seconds buffer. The performance of the system is illustrated in Figure 7.15.

Whilst conservative in nature, the sensitivity of the system causes occasional false negatives (an 'unsafe' condition when conditions are 'safe') that are difficult to remove without influencing the prediction of unsafe landing points. This condition was favoured in design, as false negatives have less implication to a helicopter landing than a false positive (a predicted 'safe' condition when conditions are actually 'unsafe').

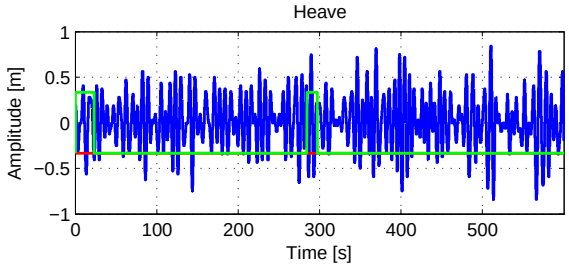

(a) Heave Classification

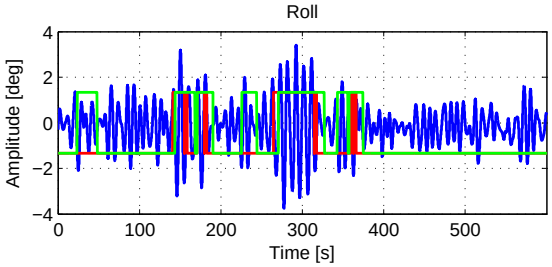

(b) Roll Classification

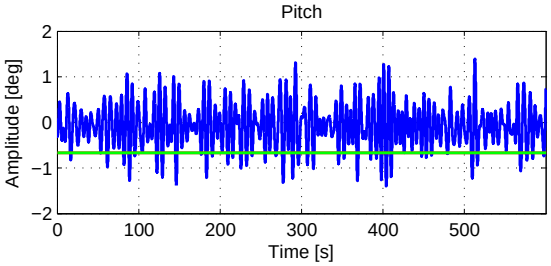

(c) Pitch Classification

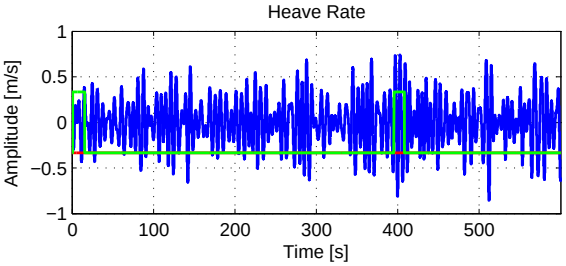

(d) Heave Rate Classification

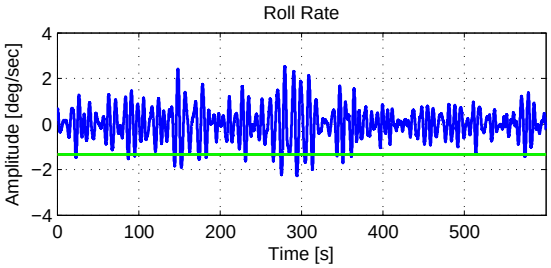

(e) Roll Rate Classification

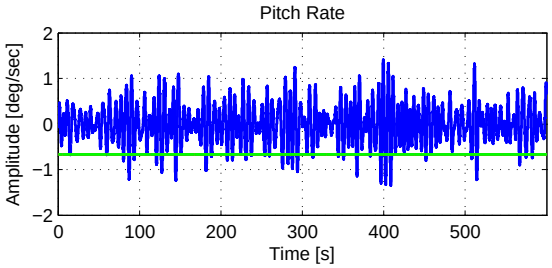

(f) Pitch Rate Classification

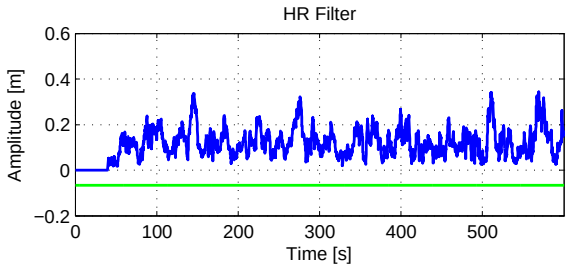

(g) Heave Error Propagation Classification

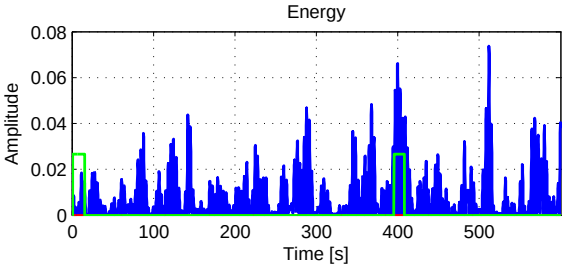

(h) Energy Classification

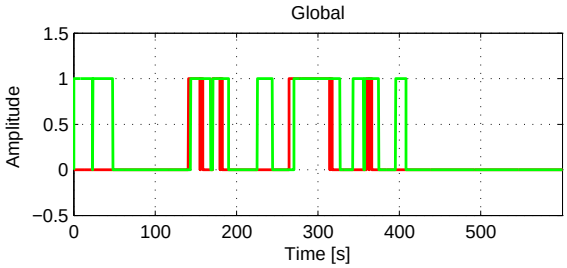

(i) Final Classification (aggregate)

Figure 7.14: Prediction for a Low-Energy Dataset

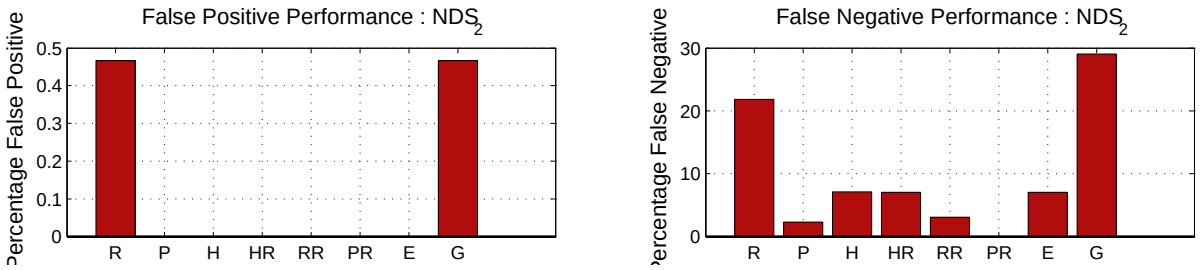

(a) False Positive Performance

(b) False Negative Performance

Figure 7.15: Classifier Performance

7.9 Conclusion

In this chapter it was shown that linear prediction techniques can be used to provide an indication of safe landing opportunities, although general loss of coherence after a certain horizon indicates an inability for linear prediction to perform optimally in some scenarios. Individual channel prediction provides useful classification and some channels provide inherent phase advance capabilities that can be used to improve the performance of quiescent period detection. A classification solution was presented that, whilst still open to optimization, illustrates a potential solution to real time, conservative detection of quiescent periods. Performance could potentially be improved with the use of a more advanced prediction techniques, as well as more elaborate classification technique.

Chapter 8

Conclusions

While autonomous flight for helicopters has been a well studied problem, the research field illustrates several deficiencies relating to systems facilitating specific mission task elements (MTE's). In this regard, a combined, fully autonomous system implementing high fidelity operational landings for moving targets helps to bridge the gap between man and machine, reducing the training requirements for pilots and simultaneously improving the functional capacity of the helicopter.

Fully autonomous landings for manned helicopters on ship decks remains an open problem, largely due to the stringent safety and performance requirements that must be met for civil or martial implementation. The application to unmanned systems, however, presents significantly less risk to operators and illustrates an ideal test bed for initial implementation.

In this work, a navigation and control system, capable of full autonomous flight and landing, was successfully designed, implemented and tested in simulation and in practice. The system was found to operate well in single point flight, stationary landing, aggressive forward flight and moving landings. Similarly, the system was also found to perform in modest wind conditions, accurately and dynamically rejecting disturbances and performing consistently with it's design criteria. The system architecture is scalable and could be implemented on a full scale helicopter if desired. All the systems were fully tested in a high fidelity Hardware in the Loop simulation, as well as on an X-Cell .90 Aerobatic Helicopter. Practical flight tests concluded with a successful demonstration of the helicopter landing on a target moving at 11 kph.

A system to detect and predict the presence of a quiescent period was also developed using ship motion data obtained from the South African Navy. The system, based on the forward prediction of the ship motion states, simultaneously allows for the early detection of dangerous conditions in addition to the detection of quiescent periods, reducing the risk in operational landings, and mitigating potentially hazardous situations. This system, highly conservative in nature, is scalable for both ship and helicopter and, when combined with an autonomous landing procedure, can be used to implement fully autonomous landings of helicopters at sea. Results show that the algorithms used in the system are feasible although further study is required to both fully optimize and improve the operational envelope of the system.

Chapter 9

Recommendations

There are several recommendations that can be made based on the performance of the systems in this research. These recommendations are detailed in the following sections.

9.1 Control System and Autonomous Behaviour

In order to improve the functioning of the control system and the autonomous behaviour, there are several recommendations that could be considered in further development.

1. Currently the estimator used in the system is based on an Extended Kalman Filter (EKF) with fixed noise covariances. These estimator modes could be improved by adapting the estimator to the GPS mode of operation, optimizing the state estimation process for the various GPS modes (Single Point, RTK and ALIGN modes, specifically).
2. The lateral controllers, empirically, are susceptible to oscillation when performing in the presence of large winds. This should be investigated and additional robustness included for the helicopter's operational envelope.
3. The system currently utilizes a single trim point for the calculation of it's gains, and bank-to-turn aircraft-style control is not implemented for fast speeds (considered out of the scope of this project). It is recommended that control gains are calculated and gain scheduling implemented for a variety of forward speeds to extend the flight envelope of the helicopter. The gain scheduling should also take the accuracy of the GPS measurement into account to ensure optimal performance in light of variable sensor accuracy.
4. A robust method of detecting that a landing has occurred should be implemented to ensure that the helicopter always transitions to the landed state upon impact.

9.2 Hardware Implementation and Testing

The hardware implementations of the helicopter control systems illustrated several limitations that could be improved upon in future projects.

1. Radio Frequency interference on the 2.4GHz band was found to be a severe limitation in the practical testing of the system, as the pilot remote, WiFLY and Maxstream all transmit on the same frequency. It is recommended that either the remote or the MaxStream systems are shifted to a lower band to reduce local interference.
2. The NovAtel differential GPS system is legacy equipment and was found to be the limiting factor in the operational bandwidth of the practical system. It is recommended that this system be replaced with a newer, faster GPS system so as to improve the functional capabilities of the helicopter in flight.
3. The avionic systems used are based on the dsPIC33EP512GP806, a digital signal processing embedded CPU produced by Microchip. While certainly powerful in it's own right, the computational bandwidth is occasionally exceeded during operation, causing control cycles to be missed. It is recommended that either a more powerful processor is used in future development or that the clocking frequency of the hardware is raised.
4. The MaxStream units were found to provide a very limited bandwidth and range, representing a fundamental limitation in the communication between the ground station operator and the aircraft. It is recommended that this unit be upgraded to allow expansion on system capabilities.

9.3 Quiescent Period Detection System

The isolation of ideal landing periods is a challenging task that has several limitations. In particular, the following recommendations are considered to be pertinent to the development of the system and the field as a whole.

1. The field appears to be underdeveloped, requiring a large amount of study to better define probability based ship motion characteristics. Should a generic, state-dependant model be found that can be used to predict the dynamics of the ship based purely on it's current or past motion information, a less stochastic model could be implemented to improve the prediction model.
2. Performance characteristics are difficult to gauge due to the variety of conditions in which the ship can operate, alongside the impracticability of testing and comparing a system's performance for multiple scenarios. The datasets available should be characterised off line to define the sea state level, the mean frequency content as well as a measure of the volatility. The system's performance in a variety of conditions could then be analysed and automatically graded based on batch tests.
3. Different prediction algorithms should be investigated to define the relative performance of algorithms in a variety of conditions. This may lead to the dynamic selection of algorithms for different scenarios.
4. An on-line measure of coherence or volatility would greatly improve the prediction capabilities of the system, by allowing optimal prediction lengths or predictor settings to be chosen. This should be investigated to see whether a viable measure of coherence, based on previous data, can be implemented.

Bibliography

[1] F. Kendoul, "Survey of Advances in Guidance , Navigation , and Control of Unmanned Rotorcraft Systems," *Journal of Field Robotics*, vol. 29, no. 2, pp. 315–378, 2012.

[2] B. Mettler, T. Kanade, and M. Tischler, "System identification modeling of a model-scale helicopter," *Robotics*, vol. 17, no. 6, pp. 1–25, 2000.

[3] E. Feron and E. Johnson, "Aerial Robotics," in *Springer Handbook of Robotics* (B. Siciliano and O. Khatib, eds.), ch. 44, pp. 1009–1029, Springer, 2008 editi ed., 2008.

[4] N. Carstens, *Development of a Low-Cost, Low-Weight Flight Control System for an Electrically Powered Model Helicopter*. Master's thesis, Stellenbosch University, 2005.

[5] V. Gavrilets, "Avionics system for a small unmanned helicopter performing aggressive maneuvers," in *Digital Avionics Systems Conference, 2000. Proceedings. DASC. The 19th*, (Philadelphia, Pennsylvania), pp. 1–7, IEEE, 2000.

[6] S. Groenewald, *Development of a Rotary-Wing Test Bed for Autonomous Flight*. Master's thesis, Stellenbosch University, 2005.

[7] C. van Schalkwyk, *Full State Control of a Fury X-Cell Unmanned Helicopter*. Master's thesis, Stellenbosch University, 2008.

[8] L. Rossouw, *Autonomous Flight of an Unmanned Helicopter*. Master's thesis, Stellenbosch University, 2008.

[9] J. Hermansson and A. Gising, "Autonomous landing of an unmanned aerial vehicle," *Reglermte (Swedish Control Conference)*, no. 1, 2010.

[10] A. Cesetti, E. Frontoni, A. Mancini, and P. Zingaretti, "Autonomous safe landing of a vision guided helicopter," in *Proceedings of 2010 IEEE/ASME International Conference on Mechatronic and Embedded Systems and Applications*, (Qingdao, ShanDong), pp. 125–130, IEEE, July 2010.

[11] S. Scherer, L. Chamberlain, and S. Singh, "Autonomous landing at unprepared sites by a full-scale helicopter," *Robotics and Autonomous Systems*, vol. 60, no. 12, pp. 1545–1562, 2012.

[12] S. Saripalli and G. S. Sukhatme, "Landing a Helicopter on a Moving Target," in *Proceedings 2007 IEEE International Conference on Robotics and Automation*, (Roma, Italy), pp. 2030–2035, IEEE, Apr. 2007.

[13] S. Saripalli, "Vision-Based Autonomous Landing of an Helicopter on a Moving Target," in *AIAA Guidance, Navigation, and Control Conference*, (Chicago, Illinois, USA), pp. 1–8, American Institute of Aeronautics and Astronautics, Aug. 2009.

[14] C. Wu, D. Song, J. Qi, and J. Han, "Autonomous Landing of an Unmanned Helicopter on a Moving Platform based on LP Path Planning," in *Proceedings of the 8th International Conference on Intelligent Unmanned Systems (ICIUS 2012)*, no. Icius, (Singapore), pp. 978–981, 2012.

[15] W. Bagen, J. Hu, and Y. Xu, "A vision-based unmanned helicopter ship board landing system," in *CISP '09. 2nd International Congress on Image and Signal Processing*, (Tianjin), pp. 2–6, IEEE, 2009.

[16] S. Oh, K. Pathak, and S. Agrawal, "Autonomous helicopter landing on a moving platform using a tether," in *Proceedings of the 2005 IEEE International Conference on Robotics and Automation*, no. April, (Barcelona, Spain), pp. 3960–3965, 2005.

[17] D. Lee, T. Ryan, and H. J. Kim, "Autonomous landing of a VTOL UAV on a moving platform using image-based visual servoing," in *2012 IEEE International Conference on Robotics and Automation*, (Saint Paul, Minnesota, USA), pp. 971–976, IEEE, May 2012.

[18] B. Mettler, M. B. Tischler, and T. Kanade, "System Identification of Small-Size Unmanned Helicopter Dynamics," in *American Helicopter Society 55th Annual Forum Proceedings*, vol. 2, (Montreal, Quebec, Canada), pp. 1706–1717, 1999.

[19] R. Cunha and C. Silvestre, "Dynamic Modeling and Stability Analysis of Model-Scale Helicopters with Bell-Hiller Stabilizing Bar," *AIAA Guidance, Navigation, and Control Conference and Exhibit*, Aug. 2003.

[20] A. Budiyono, T. Sudiyanto, and H. Lesmana, "First principle approach to modeling of small scale helicopter," in *ICIUS 2007*, (Bali, Indonesia), pp. 100–110, 2007.

[21] M. La Civita, *Integrated Modeling and Robust Control for Full-Envelope Flight of Robotic Helicopters*. Phd, Carnegie Mellon University, 2002.

[22] V. Gavrilets, "Aggressive Maneuvering of Small Autonomous Helicopters: A Human-Centered Approach," *The International Journal of Robotics Research*, vol. 20, pp. 795–807, Oct. 2001.

[23] C. Liu, W.-H. Chen, and J. Andrews, "Piecewise constant model predictive control for autonomous helicopters," *Robotics and Autonomous Systems*, vol. 59, pp. 571–579, July 2011.

[24] L. A. Sandino, M. Bejar, and A. Ollero, "On the applicability of linear control techniques for autonomous landing of helicopters on the deck of a ship," in *2011 IEEE International Conference on Mechatronics*, (Istanbul), pp. 363–368, IEEE, Apr. 2011.

[25] S. Esmailifar and F. Saghafi, "Autonomous Unmanned Helicopter Landing System Design for Safe Touchdown on 6DOF Moving Platform," in *2009 Fifth International Conference on Autonomic and Autonomous Systems*, (Valencia), pp. 245–250, IEEE, 2009.

[26] K. Peng, G. Cai, B. M. Chen, M. Dong, K. Y. Lum, and T. H. Lee, "Design and implementation of an autonomous flight control law for a UAV helicopter," *Automatica*, vol. 45, pp. 2333–2338, Oct. 2009.

[27] J. Avila Vilchis, B. Brogliato, a. Dzul, and R. Lozano, "Nonlinear modelling and control of helicopters," *Automatica*, vol. 39, pp. 1583–1596, Sept. 2003.

[28] T. K. Roy, M. Garratt, H. R. Pota, and H. Teimoori, "Robust altitude control of an unmanned autonomous helicopter using backstepping," *Proceedings of the 10th World Congress on Intelligent Control and Automation*, pp. 1650–1654, July 2012.

[29] L. Marconi and R. Naldi, "Aggressive control of helicopters in presence of parametric and dynamical uncertainties," *Mechatronics*, vol. 18, pp. 381–389, Sept. 2008.

[30] M.-D. Hua, T. Hamel, P. Morin, and C. Samson, "Introduction to Feedback Control of Underactuated VTOL Vehicles: A Review of Basic Control Design Ideas and Principles," *IEEE Control Systems*, vol. 33, pp. 61–75, Feb. 2013.

[31] M. Ax and S. Thamke, "Optical Position Stabilization of an UAV for Autonomous Landing," in *Proceedings of ROBOTIK 2012; 7th German Conference on Robotics*, (Munich, Germany), pp. 1–6, IEEE, 2012.

[32] P. J. Garcia-Pardo, G. S. Sukhatme, and J. F. Montgomery, "Towards vision-based safe landing for an autonomous helicopter," *Robotics and Autonomous Systems*, vol. 38, pp. 19–29, 2002.

[33] G. D. Padfield, *Helicopter Flight Dynamics*. Oxford, UK: Blackwell Publishing Ltd, Jan. 2007.

[34] V. Gavrilets, *Autonomous Aerobatic Maneuvering of Miniature Helicopters*. Doctor of philosophy, Massachusetts Institute of Technology, 2003.

[35] A. Bramwell, G. Done, and D. Balmford, *Bramwell's helicopter dynamics*. Oxford: Butterworth-Heinemann, second ed., 2000.

[36] P.-J. Bristeau, E. Dorveaux, D. Vissière, and N. Petit, "Hardware and software architecture for state estimation on an experimental low-cost small-scaled helicopter," *Control Engineering Practice*, vol. 18, pp. 733–746, July 2010.

[37] J. Blakelock, *Automatic control of aircraft and missiles*. John Wiley and Sons, second ed., 1991.

[38] W. Johnson, *Helicopter theory*. New York: Dover Publications, 1994 ed., 1980.

[39] V. Gavrilets, B. Mettler, and E. Feron, "Nonlinear model for a small-size acrobatic helicopter," in *AIAA Guidance, Navigation, and Control Conference*, (Montreal, Canada), American Institute of Aeronautics and Astronautics, 2001.

[40] HCA, "New helideck classification and pitch, roll and heave limits," tech. rep., Helicopter Certification Agency, Bristow, UK, 2010.

[41] J. Riola, J. Diaz, and J. Giron-Sierra, "The Prediction of Calm Opportunities for Landing on a Ship : Aspects of the Problem," in *Oceans*, (Santander, Spain), 2011.

[42] A. D. Swart, *Monocular Vision Assisted Autonomous Landing of a Helicopter on a Moving Deck*. Master's thesis, Stellenbosch University, Stellenbosch, 2013.

[43] J. Blackwell and R. Feik, "A Mathematical Model of the On-Deck Helicopter/Ship Dynamic Interface," tech. rep., Aeronautical Research Laboratory, Australian Department of Defence, Melbourne, 1988.

[44] V. Gavrilets, I. Martinos, B. Mettler, and E. Feron, "Control Logic for Automated Aerobatic Flight of a Miniature Helicopter," in *AIAA Guidance, Navigation, and Control Conference and Exhibit*, no. August, (Reston, Virigina), pp. 1–8, American Institute of Aeronautics and Astronautics, Aug. 2002.

[45] E. Feron and M. Brenner, "Time-frequency analysis for transfer function estimation and application to flutter clearance," *Journal of Guidance, Control, and Dynamics,*, vol. 21, no. 3, 1998.

[46] E. Morris, H. Zienkiewicz, and M. Belmont, "Short Term Forecasting of the Sea Surface Shape," *International Shipbuilding Progress*, vol. 45, no. 444, pp. 383–400, 1997.

[47] I. Yumori, "Real Time Prediction of Ship Response to Ocean Waves Using Time Series Analysis," in *OCEANS 81*, pp. 1082–1089, IEEE, 1981.

[48] A. A. Khan, C. Bil, and K. Marion, "Real Time Prediction Of Ship Motion For The Aid Of Helicopter And Aircraft Deployment And Recovery," *25th International Congress of the Aeronautical Sciences*, pp. 1–6, 2006.

[49] X. Zhao, R. Xu, and C. Kwan, "Ship-motion prediction: algorithms and simulation results," in *2004 IEEE International Conference on Acoustics, Speech, and Signal Processing*, vol. 5, pp. V–125–8, IEEE, 2004.

[50] X. Yang, "Displacement motion prediction of a landing deck for recovery operations of rotary UAVs," *International Journal of Control, Automation and Systems*, vol. 11, pp. 58–64, Jan. 2013.

[51] B. W. Sherman, *The Examination and Evaluation of Dynamic Ship Quiescence Prediction and Detection Methods for Application in the Ship- Helicopter Dynamic Interface*. Master's thesis, Virginia Polytechnic Institude, 2007.

[52] B. Ferrier and T. Manning, "Simulation and Testing of the Landing Period Designator (LPD) Helicopter Recovery Aid," *Naval Engineers Journal*, vol. 110, pp. 189–205, Jan. 1998.

[53] X. Yang, M. Garratt, and H. Pota, "Monotonous Trend Estimation using Recursive Prony Analysis," in *Australian Control Conference*, no. November, (Melbourne), pp. 321–326, 2011.

[54] X. Yang and H. Pota, "Ship motion prediction for maritime flight operations," in *Proceedings of the 17th World Congress*, (Seoul, South Korea), pp. 12407–12412, The International Federation of Automatic Control, 2008.